LIBRARY
Michigan State
University

PLACE IN RETURN BOX to remove this checkout from your record.
TO AVOID FINES return on or before date due.
MAY BE RECALLED with earlier due date if requested.

DATE DUE	DATE DUE	DATE DUE
	JUL 13 2008	

6/01 c:/CIRC/DateDue.p65-p.15

POLY-C TECHNOLOGIES FOR FIELD EMISSION ELECTROLUMINESCENCE

By

Ungsik Kim

A DISSERTATION

Submitted to
Michigan State University
in partial fulfillment of the requirements
for the degree of

DOCTOR OF PHILOSOPHY

Department of Electrical and Computer Engineering

2002

ABSTRACT

POLY-C TECHNOLOGIES FOR FIELD EMISSION ELECTROLUMINESCENCE

By

Ungsik Kim

Poly-crystalline diamond and carbon nanotube, with their unique mechanical, thermal, chemical and electrical properties, are attractive materials for field emission display applications. The research reported in this thesis concerns the investigation of electron emission and electro-luminescence during electron emission from diamond and carbon nanotube.

Diamond and carbon nanotube emitters were fabricated under various growth conditions using microwave plasma chemical vapor deposition system. Methane concentration in hydrogen and extrinsic doping of boron were used to vary the defect density in diamond films. Various shapes of multi-wall carbon nanotubes with diameters ranging from 20 - 400 nm and densities in the range of 10^8 - 10^9 cm^{-2} were grown on iron and nickel coated substrates.

The spatial mapping of electron emission over the sample surface was achieved by computer controlled x-y-z stages with 1 μm resolution in a vacuum chamber. The mapping study revealed that secondary nucleation on the diamond film surface which resulted in an increase of density of grain boundaries played an important role in improving the electron

emission. Vertically aligned carbon nanotubes improved dramatically the site density and uniformity of electron emission. Carbon nanotubes were grown on a pointed metal tip with a radius of a few microns. It was demonstrated that the tube on a tip could be used as single electron source.

We have reported for the first time field emission electro-luminescence (FEEL) from poly-crystalline diamond although light emission during field emission from carbon nanotube was observed by other researchers. The analysis of spectral data indicated that the defects present in the film served as luminescent centers. The quantitative models for FEEL and hysteresis behavior of emission current were discussed. FEEL is potentially attractive for display devices without the need for phosphor-coated screens.

ACKNOWLEDGEMENTS

The author wishes to thank his advisor, Dr. Dean Aslam, for his encouragement, guidance and support throughout this research. Additional thanks are extended to Dr. Donnie K. Reinhard, Dr. Timothy A. Grotjohn and Dr. David Tomanek for their valuable discussions and academic advices. The author is also thankful to Dr. Steve Rand of University of Michigan for help in developing the qualitative model.

The author would like to thank all the members of Dr. Aslam's research group for their assistance and helpful discussions.

Last but not least, the author would like to thank his family in Korea and his wife, Dayoung Kim, for their patience, understanding and sacrifice during the course of this study.

This work was supported in part by the Engineering Research Centers Program of the National Science Foundation under Award Number EEC-9986866.

TABLE OF CONTENTS

LIST OF TABLES

LIST OF FIGURES

CHAPTER 1

RESEARCH MOTIVATION AND GOALS

1.1 Introduction

Devices based on microfabricated field emission sources were proposed in the early 1960s [1]. The concept of molybdenum microtip emitters was first developed by Spindt [2]. A variety of materials and structures have been attempted thereafter to improve the performance of the devices [3,4,5]. The development of a new generation of flat panel displays can be regarded as a strong driving force for stimulating the research effort in the field of carbon cold cathodes. Various forms of carbon based materials, such as CVD diamond film, amorphous carbon, graphite, and carbon nanotubes, are being studied concerning both fundamental and applied purposes in flat panel displays, microwave tubes and point electron guns [6,7,8,9,10,11]. The ideal emitter has a high carrier concentration and high mobility that results in good electrical conductivity to keep up stable emission and to enable high speed applications. A high electric field breakdown strength is also important to avoid destruction by arching. The thermal conductivity should be sufficient that the heat generated by the high current densities can be quickly dissipated. The emitter medium should be chemically inert to avoid an emission decay

during ion bombardment or surface diffusion on the cathode surface. The resistance to chemical attacks would make it possible to use a lower vacuum without running into emission deterioration. High tensile strength and low vapor pressure minimize mechanical surface damage due to high electric field forces, and emission noise.

Diamond and carbon nanotubes have proven themselves as excellent candidates for the next generation of electron-emission devices [12,13]. Parallel investigations of both the physics of emission and attempts for devices have taken places [6,14]. The original interest in investigating emission properties of diamond stems from the fact that certain orientations of diamond exhibit negative electron affinity [15,16]. This means that the vacuum level lies below the conduction band edge so that electrons present in the conduction band can readily escape the surface. The potential use of carbon nanotubes as a material for electron emitter originates from the small diameter and elongated shape of the tube that lead to a high geometrical field enhancement [17]. Another strong point of carbon nanotube emitters is the relatively simple production in large quantities [18,19].

1.2 Objective of This Work

The scope of the present work is to understand the electron emissions of poly-diamond and carbon nanotubes and to gain a detailed understanding of electro-luminescence during field emission.

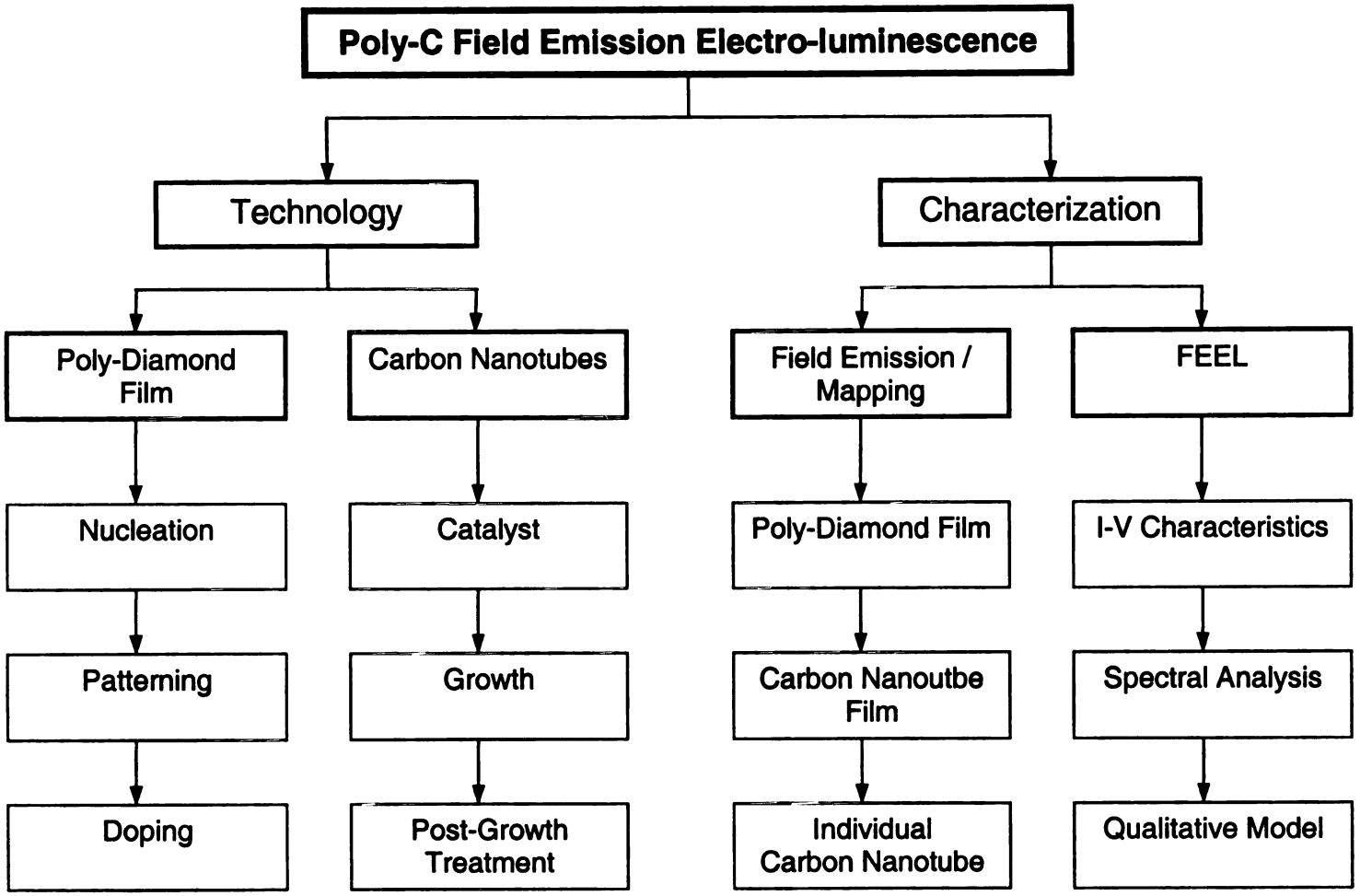

Figure 1-1: Overview of poly-C field emission electro-luminescence.

Figure 1.1 illustrates an overview of the present study. Infrastructure technologies for diamond and carbon nanotubes are required to successfully fabricate the emitter structures and related systems. The deposition parameters, such as temperature, doping, gas mixture ratio and pre/post-growth treatment, influence the film morphology and defect contents. Although nanotube geometric structures appear to be ideally suited as field emission, the orientation and density of the tubes are critical for emission properties. The electron emission characteristics with respect to the density of nanotubes were reported [20]. The low density nanotube film showed inhomogeneous emission with very few sites emitting a low current. A much more homogeneous emission image was obtained for a medium density film. A very dense film yielded a result similar to the low density film. The length of the tubes and the distance between neighboring emitters are important to reach a high field enhancement along with an emitter density that is high enough to ensure homogeneous emission at low fields. To best utilize the characteristics of nanotubes for field emission, the tubes should have highly oriented and well-distributed. The electron emission from the surface of diamond and nanotubes is non-uniform which arises from non-uniformity of emission sites. It is, however, not clear whether this non-uniformity is related to variation of electron affinity, surface roughness, defects or grain size for diamond films and orientation, defects or non-uniform distribution of nanotubes. I-V characteristics and spectral data are expected to be helpful for

understanding the field emission electro-luminescence mechanism. A model that can be used to explain the observed field emission induced electro-luminescence will be made.

The present research mainly focuses on the following issues:

(1) The development of fabrication techniques for diamond and carbon nanotube field emitters.

(2) Characterization of field emission/mapping and electro-luminescence properties from fabricated emitters.

(3) Qualitative explanation of field emission electro-luminescence.

1.3 Dissertation Organization

Chapter 2 presents a brief overview of the current technologies of diamond and carbon nanotubes. Unique properties of diamond and nanotubes are reviewed. It considers the various methods for synthesizing nanotubes, including arc evaporation and catalytic growth. Field emission studies from various types of diamond and nanotubes are summarized. Defects in diamond investigated by luminescence techniques are discussed. Luminescence researches on diamond and carbon nanotubes are also given. In chapter 3, poly-C technologies used in this study are

outlined. The detail description of the film deposition system, MPCVD, is given. Nucleation, patterning, doping, and characterization of diamond film are investigated. Nanotube growth procedure and method of purifying tubes are also covered. Chapter 4 focuses on the characterization of field emission from diamond and carbon nanotube films as well as nanotubes on a pointed metal tip. The computer controlled system is used to study a spatial mapping of electron emission over the sample surface. In chapter 5, experimental observations of electroluminescence during field emission are described. The qualitative models for field emission electroluminescence and hysteresis behavior of emission current are proposed. Chapter 6 presents conclusions of this study and considers possible future directions.

CHAPTER 2

DIAMOND AND CARBON NANOTUBES: A REVIEW

2.1 Introduction

An overview of diamond and carbon nanotube films is presented. The properties of the films are discussed. The fabrication of carbon nanotubes (CNT) using different methods is described. Various types of poly-diamond (poly-C) and CNT field emitters are summarized. Luminescence studies are reported in detail.

2.2 A Review of Diamond

The unique electrical, chemical, thermal and mechanical properties of poly-diamond as a field emitter are reported. Comprehensive field emission and luminescence studies from diamond are discussed.

2.2.1 Properties of Diamond

Diamond is comprised of covalently bonded carbon atoms in a diamond cubic crystal structure, shown in Figure 2-1(a).

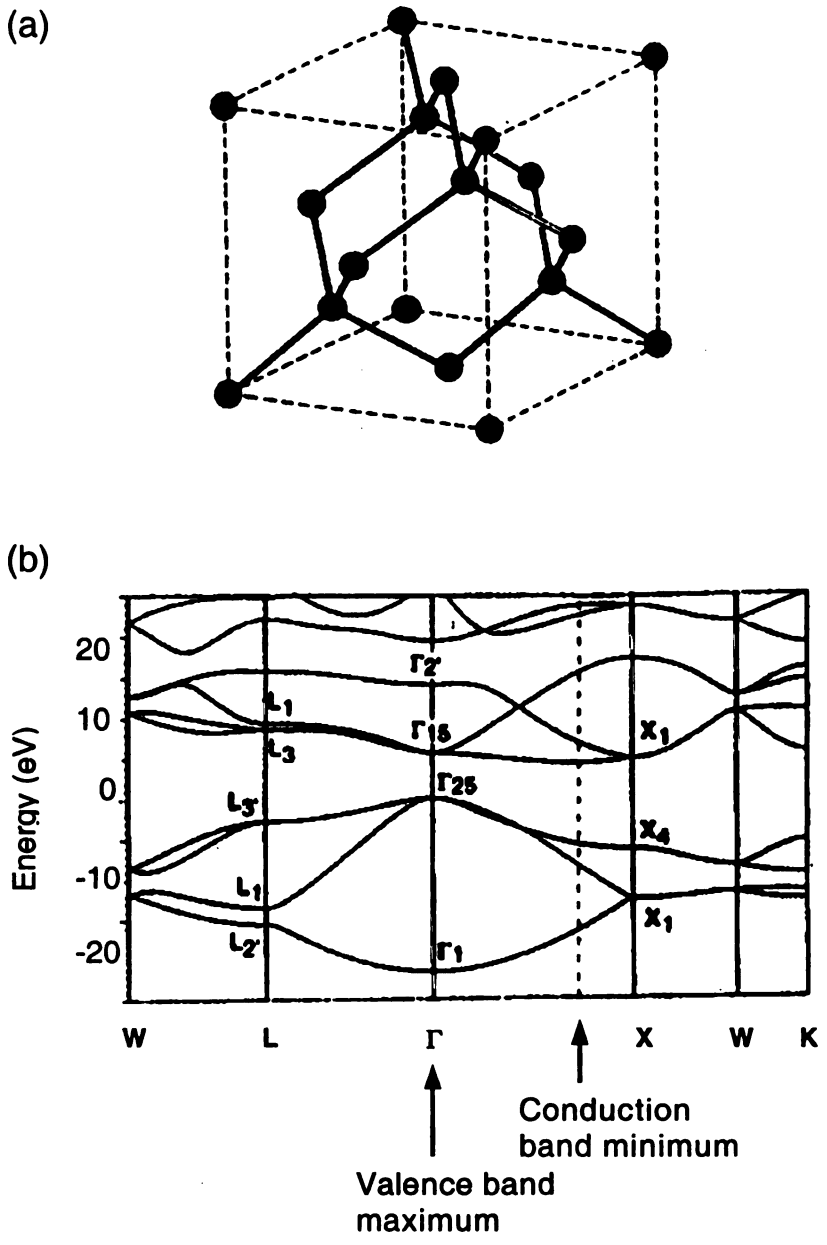

Figure 2-1: (a) Unit cell of diamond structure and (b) band structure of diamond.

Table 2-1: Properties of diamond.

Lattice constant	0.356725 nm
Atom density	1.77×10^{27} cm^{-3}
Hardness	5700-10,400 kg/mm^2
Young's modulus	10.5×10^{11} N/m^2
Density	3.515 g/cm^3
Coefficient of thermal expansion	0.8×10^{-6} C
Thermal conductivity	20 W/cm·K
Specific heat	6.195 J/K·mol
Melting point	4000 C
Refractive index	2.42
Band gap	5.45 eV
Resistivity (IIa)	$>10^{14}$ Ω·cm
Dielectric constant	5.7
Hole mobility	1600 $cm^2/V·s$
Electron mobility	2000 $cm^2/V·s$
Electron saturated current velocity	2.7×10^7 cm/s
Hole saturated current velocity	1×10^7 cm/s
Electric breakdown field	1×10^7 V/cm
Johnson figure of merit	73856×10^{23} $W·Ω/s^2$
Keyes figure of merit	444×10^2 W·C/cm·s

The diamond lattice can be thought of as a face centered cubic (FCC) structure with an extra atom placed at a/4 + b/4 + c/4 from each of the FCC atoms with a, b, c being the basis vectors of the lattice. Therefore, four additional points within every unit cell are occupied by atoms resulting from two interpenetrating FCC sublattices. In diamond covalent sp^3-bonding is found, which distinguishes it from other carbonaceous structures with different hybridization. Diamond with its low dielectric constant $\varepsilon_r = 5.7$ has a high electrical breakdown field strength of 10^7 V/cm for undoped diamond, and a high electron saturation velocity at 2.7×10^7 cm/s which is favorable for high speed applications [21]. It is not very reactive so that surface contaminations are of lesser concern. A thermal conductivity of 20 W/cm·K enables a quick dissipation of heat induced by high emission current [22]. In addition, diamond has a low coefficient of thermal expansion at room temperature. In the [111] direction, electron affinity is very small or even negative [15] whereas defect density and stress are high. Diamond has an indirect band gap of 5.45 eV, as depicted in Figure 2-1(b). Due to its large band gap, diamond is an insulator, in the absence of dopants, at room temperature with a resistivity on the order of $>10^{14}$ Ω̄cm [23]. The properties of diamond are summarized in Table 1.

2.2.2 Field Emission from Diamond

The wide bandgap of diamond produces interesting effect. The conduction band approaches the vacuum level. The energy difference between the vacuum level and conduction band is known as the electron affinity, while the work function is the energy difference between the Fermi level and the vacuum level. The work function of most metals is 4 eV to 5 eV. In diamond, there is some evidence that the conduction band may exceed the vacuum level, yielding a negative electron affinity [15,24]. Therefore, there is no potential barrier for the electron emission from the conduction band. The electron emission current density is a function of not only the barrier height, but also of the electron supply which in turn depends on the electron concentration in the conduction band. Because of the wide bandgap of diamond, to obtain significant electron emission one needs to populate the conduction band by doping or by injection of carriers from a metal contact. While p-type doing of diamond has been demonstrated, effective n-type doping is still unsuccessful. Nitrogen is an n-type dopant in diamond but its energy level is significantly below the bottom of the conduction band. Consequently, the increase of concentration of electrons due to the nitrogen doping is insignificant. Exact mechanisms of the electron injection from the metal contacts, as well as of the electron transport through the diamond film remain subjects of theoretical modeling and discussions [12,25,26,27]. Diamond may promise as a cold cathode electron source for use in flat panel displays [6,28].

Table 2-2: Diamond field emitters.

Emitter	Deposition method	Current or Current density	Electric Field (V/μm)	Reference
Patterned diamond array	HFCVD	3.5 mA	0.8	[52]
P-doped diamond	MPCVD	1 nA	15.5	[50]
B-doped piramidal diamond tip	PECVD	10 nA	9	[59]
N-doped diamond	HFCVD	0.25 mA/cm^2	3	[46]
B-doped diamond	MPCVD	58 $\mu A/cm^2$	21.6	[42]
B-doped diamond	MPCVD	4.89 mA/cm^2	35	[43]
N-doped nanodiamond	MPCVD	25 μA	1.3	[32]
C-implanted diamond	MPCVD	10 mA/cm^2	42	[39]
N-doped type Ib diamond	High pressure	1 nA/cm^2	0.2	[47]
B-doped type IIb diamond cones	Ion sputtering	80 nA/cm^2	3.8	[44]
Poly-diamond	DC discharge	1.5 mA/cm^2	10	[36]
a-diamond	Laser ablation	100 mA/cm^2	40	[31]

Table 2-2: Continued.

Emitter	Deposition method	Current or Current density	Electric Field (V/μm)	Reference
N-doped diamond/ a-C/Mo	MPCVD	290 μA	10.4	[57]
Poly-diamond	MPCVD	22 $\mu A/cm^2$	22	[37]
N-doped Poly-diamond	CVD	20 $\mu A/cm^2$	2	[48]
Diamond powder	HPHT	1 A/cm^2	35	[12]
Diamond	CVD	500 mA/cm^2	10	[63]
Diamond/Si tip	CVD	320 mA/cm^2	6.8	[54]
N-doped type Ib		1 mA/cm^2	10-20	[49]
Poly-diamond	Explosive synthesis	10 mA/cm^2	3-5	[64]
B-doped diamond	MPCVD	10 mA/cm^2	30	[45]
Diamond	HFCVD	0.1 mA/cm^2	8	[65]
B-doped diamond	HFCVD	1 mA/cm^2	18	[66]
B-doped gated array	HFCVD	0.1 A/cm^2	20	[6]
B-doped poly- & undoped nano-diamond	Plasma enhanced chemical transport	1 mA/cm^2	Poly: 28-80 Nano: 7-16	[34]

Table 2-2: Continued.

Emitter	Deposition method	Current or Current density	Electric Field (V/μm)	Reference
N-doped Diamond	MPCVD	1-8 mA/cm^2	5-8	[69]
Poly-diamond	MPCVD	10 mA/cm^2	0.5%CH_4: 12.7 1.5%CH_4: 5.5	[38]
Fine-grained diamond	MPCVD	3 mA/cm^2	5	[67]
Diamond/Mo	MPCVD	25 mA/cm^2	5	[58]
B-implanted diamond	MPCVD	2.17 mA/cm^2	37	[40]
B-doped diamond	MPCVD	0.7 mA/cm^2	20	[68]
B, Na, C-doped diamond	MPCVD	10 mA/cm^2	B-doped: 30 B-impl: 62 Na-impl: 58 C-impl: 42	[41]
P-doped diamond	MPCVD	1 mA/cm^2	7.6	[51]
Patterned diamond	CVD	100 mA/cm^2	12	[60]
N-doped diamond	MPCVD	40 nA/cm^2	1.8	[70]

Table 2-2: Continued.

Emitter	Deposition method	Current or Current density	Electric Field (V/μm)	Reference
CVD-,HPHT-,nano-diamond		CVD-D: 4.37 mA/cm^2 HPHT-D: 29.5 mA/cm^2 ND: 79.6mA/cm^2	CVD-D: 8 HPHT-D: 5.3 ND: 20	[35]
Bias-grown Diamond	MPCVD	12.7 μA/cm^2	2	[71]
ArF laser irradiation in ammonia atmosphere on nano-diamond	DC arc discharge	0.2 A/cm^2	100	[33]
Diamond/Si tip	MPCVD	Ungated:57μA Gated:3.4μA	Ungated: 2.5 Gated: 0.4	[53]
Poly-diamond/Si tip	HFCVD	0.23mA/40000tip	13.9	[55]

Theoretical considerations of electron emitters suggest that the desired material would be one with a low work function. In addition to low temperature emission, there are numerous benefits to an emission source with a low work function. Emission sources often have a small radius of curvature to enhance the electric field. The emission is sensitive to changes in the radius of curvature, but a low work function device would be less sensitive to geometrical effects. The turn-on voltage to initiate electron emission is reduced in a low work function material and is more abrupt. Therefore, voltage variations do not alter the emission current as significantly as in higher work function emitters with a more gradual turn-on. Another benefit of a low work function material is that the saturation emission current is higher in low work function devices. Based on these benefits, the low work function of diamond may make it ideally suited for field emission applications.

Several structures have been investigated for electron emission from diamond. A diamond junction device [29], homoepitaxial diamond [30], amorphous diamond [31], nano-crystalline diamond [32,33,34,35], and polycrystalline diamond [36,37,38] have been demonstrated. Field emission was studied from diamond films implanted [39,40,41] or doped by boron [42,43,44,45], nitrogen [46,47,48,49], or phosphorous [50,51]. Diamond was used as a tip for electron emission and these tips were made into an array [7,52]. Diamond was also used as a coating on Si [53,54,55,56] and metal tips [57,58]. Patterned diamond was investigated for electron emission

[59,60]. The resilience of diamond emission when exposed to oxygen at 10^{-2} Torr was demonstrated [61]. In addition to a negative or low work function, field enhanced electron emission may be generated by the formation of a diamond tip with a small radius of curvature [62]. Field emission from various types of diamond is summarized in Table 2-2.

2.2.3 Luminescence from Diamond

The luminescence spectra observed when excited states relax is beneficial in assessing the properties of diamond. Cathodo-luminescence, where states are excited with an electron beam, is probably the most commonly used luminescence technique. Photo-luminescence is generated when the sample is exposed to photons and electro-luminescence is investigated when the excitation caused by an applied voltage is sufficient to generate light. The peak position and description for several common defects in diamond are summarized in Table 2-3.

- **Cathodo-luminescence (CL)**

The wavelength of the emitted photon is related to the energy difference of the transition that generated the light. Therefore, CL provides information about the defect levels within a material. The CL spectrum typically consists of sharp peaks and broad bands. The sharp peaks are indicative of discrete transitions between energy levels whereas broad bands indicate variable transition energies [72,73,74].

Table 2-3: Luminescence spectra in diamond.

Peak position (eV)	Peak position (nm)	Name	Description	Reference
5.15	240.7		Boron related acceptors	[85]
4.97	249.4			
4.65	266.6			
4.582	270		Carbon interstitial	[79]
3.188	388.8		Carbon interstitial and single nitrogen atom	[78]
2.85	435	Blue band A	Broad band – dislocations	[76]
2.8	442		Growth induced dislocation	[86]
2.33	532		Doublet line – nitrogen related	[76]
2.355	526.3		Nitrogen-carbon interstitial complex	[87]
2.284	543			
2.2	563	Green band A	Broad band – thought to be related to boron	[76]
2.156	574.9		Single N and V	[77]
1.945	638		Vacancy	[88]
1.9	652.4		Related to phosphorous	[89]
1.682	737		Silicon	[80]
1.673	741	GR1	Neutral vacancy	[80]

CL is a near-surface technique. Typical acceleration voltages are 10 to 50 keV and correspond to emission depths of 0.5 to 17.7 μm. The CL spectrum typically consists of broad bands and sharp zero phonon lines and their sidebands. Two broad peaks are often observed and are referred to as green and blue band A because they occur in the green and blue wavelengths, respectively. The broad band was thought to be associated with dislocations [75]. A comparison of the CL spectra and x-ray topographic images revealed a strong correlation of the 2.85 eV band to the dislocation density. The 2.2 eV band was thought to be attributed to a boron related center [76]. The sharp peaks were often associated with impurity atoms or aggregates. Nitrogen containing defects generated numerous CL peaks. The most common nitrogen peaks occurred at 2.156, 2.33, 2.807, and 3.188 eV. The 2.156 eV defect was thought to consist of nitrogen and a vacancy [77]. Near 2.33 eV, a doublet line occurred which was thought to be related to nitrogen [76]. Separate lines at 2.807 and 3.188 eV were thought to be caused by a single nitrogen atom and a carbon interstitial [78]. Another defect that was believed to be related to a carbon interstitial occurred at 4.582 eV [79]. The 1.681 eV defect near neutral vacancy defect was attributed to silicon [80]. The emission intensity of one defect may vary with the concentration of other defects and the efficiency of individual defects differs. Therefore, CL does not provide a quantitative determination of the defect density.

- **Photo-luminescence (PL)**

Laser light is often used for PL [81,82,83]. The luminescence occurs from defects with lower energy than the incident photons. This feature allows selective excitation of a defect by controlling the incident laser energy. The intense beam can excite lower concentration of defects. The PL spectra are similar to the CL spectra for most defects.

- **Electro-luminescence (EL)**

Although not as heavily investigated, EL generated by an applied voltage is also used to characterize diamond. Yellow-green luminescence was observed for Schottky barrier point contact probed at 300 C to 750 C [84]. EL from Schottky diode of boron-doped poly-diamond was observed [75]. Figure 2-2 shows EL spectra of the lightly doped and heavily doped diamond films, respectively. EL was observable when the forward bias across the diode exceeded 25 V or the reverse bias exceeded 20 V. The EL spectra were similar in forward and reverse biases. The luminescent center of EL was equal to that of CL.

Blue-green EL from free-standing diamond has been observed [90]. The In_2O_3 transparent conductor and conducting epoxy were used for the front and back contacts on the 15 μm thick free-standing diamond. EL was observed with the unaided eyes from the individual 5-10 μm grains of the diamond film. The peak position of EL occurred at 485 nm.

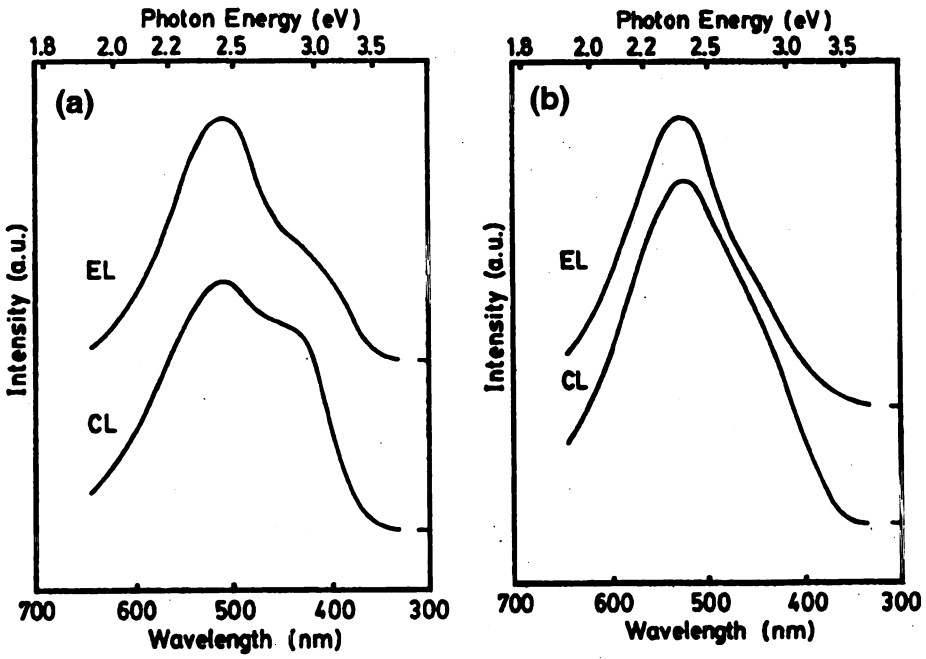

Figure 2-2: EL and CL spectra of boron-doped poly-diamond. (a) B/C = 200ppm. (b) B/C = 1000ppm.

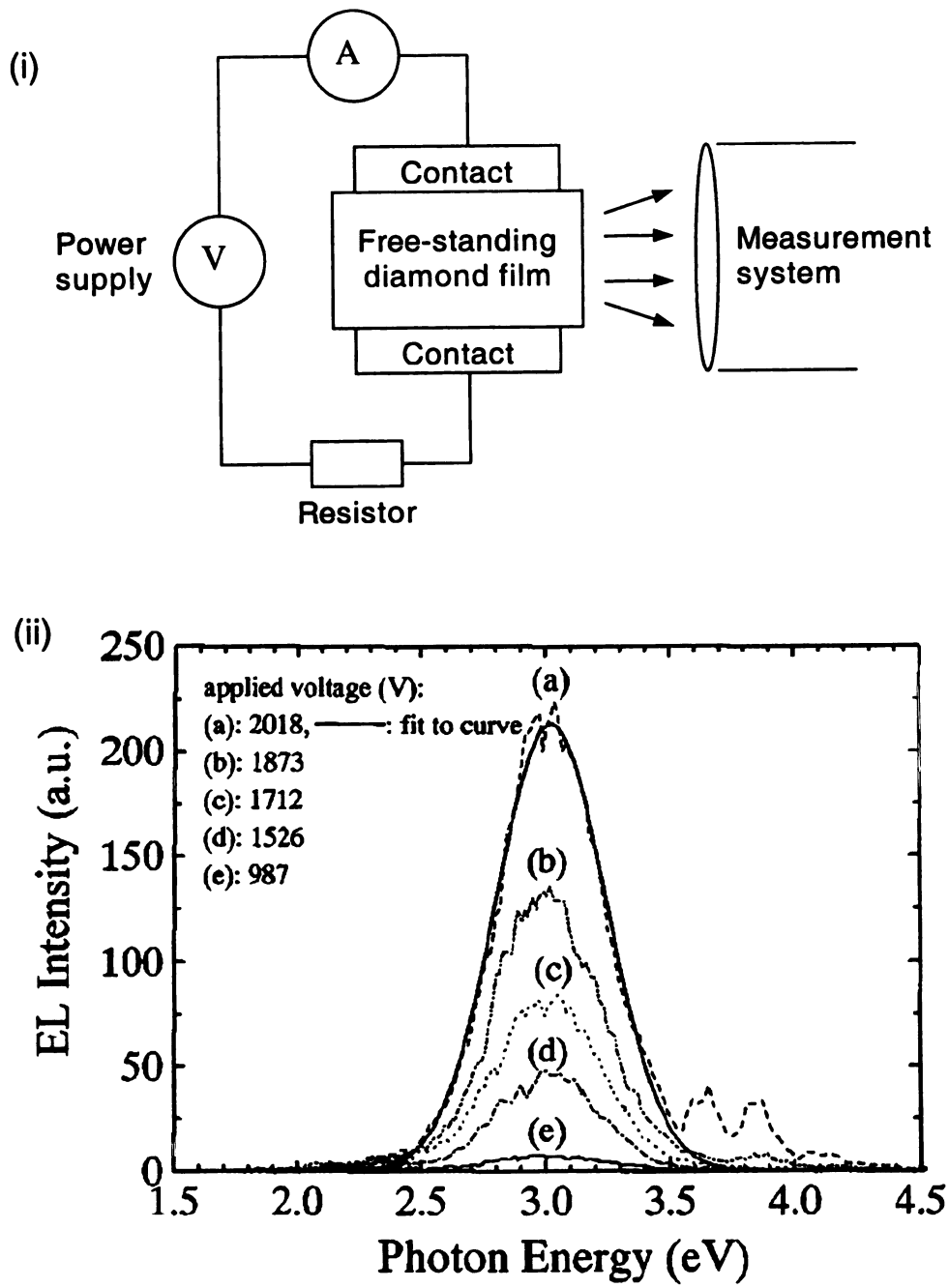

Figure 2-3: (i) Schematic diagram of experimental setup and (ii) electroluminescence spectra at different voltages.

It was proposed that the recombination of donor-acceptor pairs was responsible for the emission of the observed light. The donor was believed to be nitrogen and the acceptor was probably boron. Nitrogen contamination was likely from the wall of the reactor or from the relatively poor vacuum during deposition. The trace of boron was likely to have been carried over from deposition to deposition.

Blue-violet EL from 400 μm thick free-standing diamond has been reported [91]. The electrical contacts were provided by Ti/Pt/Au. The EL was observed at voltages above 800 V which was a field of 2 V/μm. Figure 2-3 shows schematics of experimental setup and EL spectra at different voltages. The main luminescence band was centered at 3.0 eV. Additional peaks at about 3.65 and 3.85 eV appeared at voltages above 1850 V. The subgap photocurrent spectrum in the photon energy range from 1.7 to 5.0 eV revealed that there was a 3.0 eV transition of electrons or holes between the conduction or valence band and the gap states.

2.3 A Review of Carbon Nanotubes

In this chapter, properties and fabrication methods of carbon nanotubes are discussed. Electron emission research works from a variety of nanotubes are summarized. A discussion is given of luminescence from nanotubes.

2.3.1 Property of Carbon Nanotubes

A carbon nanotube is a graphene sheet, a simple planar assembly of carbon atoms disposed in a honeycomb lattice, rolled into a cylinder. The primary classification of a carbon nanotube consists of either one cylindrical graphene sheet (single-wall nanotube, SWNT) or of several nested cylinders with an interlayer spacing of 0.34 – 0.36 nm (multi-wall carbon nanotube, MWNT). The nanotube diameter varies from ~1 nm (for SWNTs) to 400 nm (for MWNTs) and its lengths are usually well over 1 μm. One of the most significant quantum properties of carbon nanotube is its electronic structure which depends only on its geometry. The helical geometry of the honeycomb lattice is called chirality of SWNT which is unique to solid state physics [92]. The electronic structure of SWNT is either metallic or semiconducting, depending on tube diameter and chiral angle and does not require any doping. The diameter and chirality is determined by a chiral vector,

$$C_h = na + mb = (n,m) \tag{2.1}$$

where *a* and *b* are the unit vectors of graphene sheet as shown in Figure 2-4. The chiral vector specifies the equator of SWNT. Any other geometry and properties are defined by the two indices (*n,m*). Only armchair (*n,n*) and zigzag (*n,0*) nanotubes have a mirror symmetry and that the other (*n,m*) nanotube has a chiral symmetry. Metallic conduction occurs when

$$n - m = 3q \tag{2.2}$$

where *n* and *m* are the integers which specify the tube's structure and *q* is an integer [93,94,95].

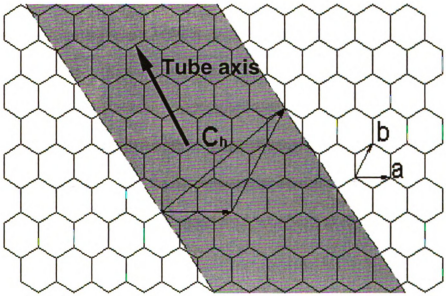

Figure 2-4: Construction of the unit cell for (2,3) nanotube.

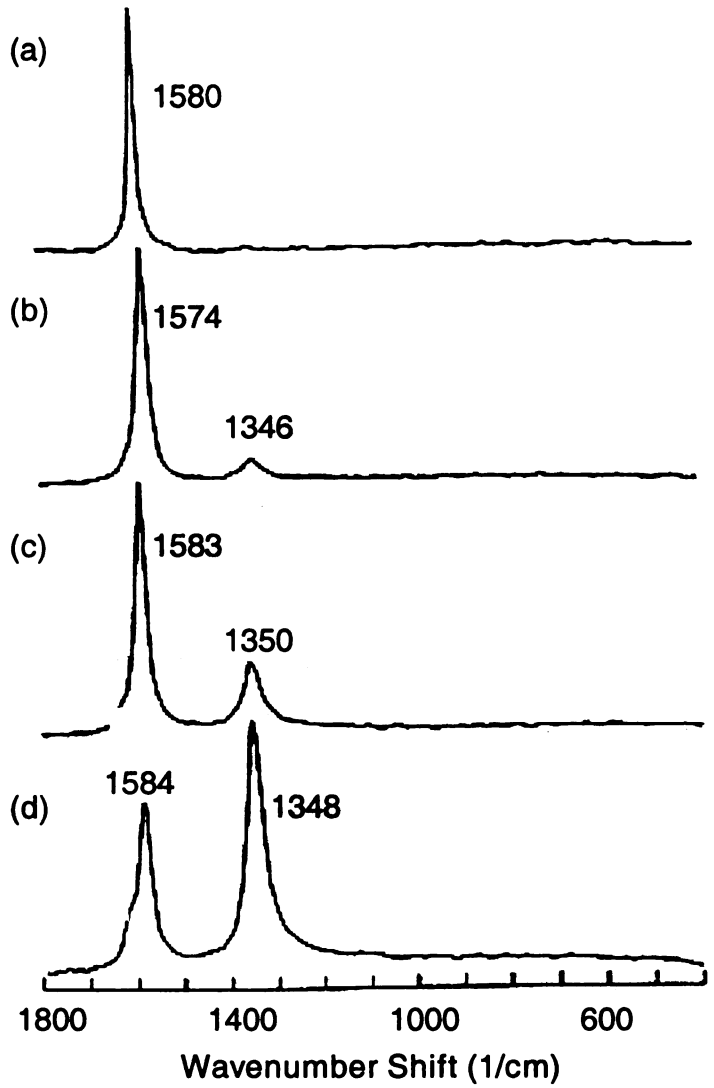

Figure 2-5: Raman Spectra of (a) highly oriented pyrolytic graphite, (b) inner core of the cathodic deposit, (c) outer shell of the cathodic deposit, and (d) glassy carbon.

All armchair tubes and one out of three zigzag and chiral tubes are metallic. The band structure of the nanotube shows a gap leading to semiconducting behavior, with a bandgap that scales approximately with the inverse of the tube radius.

Resistivity measurements on MWNT showed wide variations ($5x10^{-6}$ – 0.8 Ω·cm). Since samples of MWNT are known to be structurally heterogeneous, these results provide clear evidence that the electronic properties of carbon nanotubes can vary greatly according to their structure [18,96,97,98]. Raw cathodic soot had a resistivity of approximately 0.01 Ωcm [18]. The catalytically grown straight tubes of 8.5 nm and 13.9 nm in diameter had resistivity of 0.00195 and 0.00078 Ωcm, respectively [97]. Nanotubes were annealed at 2850 C before carrying out electrical measurements. Four metal leads were deposited with 1 μm of distance between contacts to enable four-probe measurements. The resistivity values were in the range of 0.0000051 and 0.8 Ωcm. A slight increase in resistivity was observed with decreasing temperature [98]. The resistivities of bundles of SWNTs were measured in the range of 0.000034 and 0.0001 Ωcm using MWNTs as voltage probes [99]. The resistivity of the bundles increased with the temperature above 200 K.

Figure 2-5 shows the Raman spectra of material from nanotubes and nanoparticles taken from the core of the cathode, with those from the outer shell of the cathodic deposit produced by arc evaporation process, and

with the spectra of highly oriented pyrolytic graphite and of glassy carbon [100,101]. The strong peak which occurs in the region of 1580 cm^{-1} can be assigned to Raman vibrations of graphite, while the band at around 1350 cm^{-1} can be attributed to disorder. However, the spectra do not give detailed information about nanotube structure since the core deposit contains nanotubes with a variety of different sizes and structures. There is little difference between Raman spectra from purified and unpurified nanotube samples [102].

The theoretical work predicted the Young's modulus for nanotubes close to that for a graphene sheet (1060 GPa) [103,104,105]. The quantitative measurements of the mechanical properties of nanotubes were carried out in the transmission electron microscopy (TEM) and atomic force microscopy (AFM). The Young's modulus ranged from 400 GPa to 4100 GPa [106,107,108,109]. Clusters of nanotubes were deposited on TEM grids such that isolated tubes were extended for a considerable distance into empty space. The Young's modulus was estimated from 410 to 4150 GPa, with an average of 1800 GPa. The large spread in values resulted from uncertainties in estimating the lengths of the anchored tubes, and from the presence of defects in the tube structures [106]. Scanning probe microscopy enabled individual tubes to be manipulated directly. One end of the tube was fixed, and then the bending force of the tube was determined as a function of displacement. A linear curve for lateral force versus displacement was observed from MWNTs. The results implied a

value of ~1.28 TPa for the Young's modulus [110]. Carbon nanotubes were subjected to large bending stresses using atomic force microscopy. The tubes were not fixed at one end, but were supported on mica. It was found that the tubes can be bent repeatedly through large angles without fracturing [111].

2.3.2 Fabrication of Carbon Nanotubes

A description of arc evaporation method of nanotube synthesis is given. This is a classic method of preparing MWNTs, and produces good quality tubes. Carbon vapor condensation, pyrolysis, and electrochemical methods are summarized. Catalytic method for producing MWNTs is discussed.

- **Arc evaporation**

The arc discharge technique [112] has been in use for the production of carbon fibers as depicted in Figure 2-6. The graphite electrodes are held a short distance apart during arching. Some of the carbon which evaporated from the anode re-condensed as a hard cylindrical deposit on the cathodic rod. The deposit on the cathode contains both nanotubes and nano-particles. A number of factors have been shown to be important in producing a good yield of high quality nanotubes. The most important is the pressure of the helium in the evaporation chamber [18].

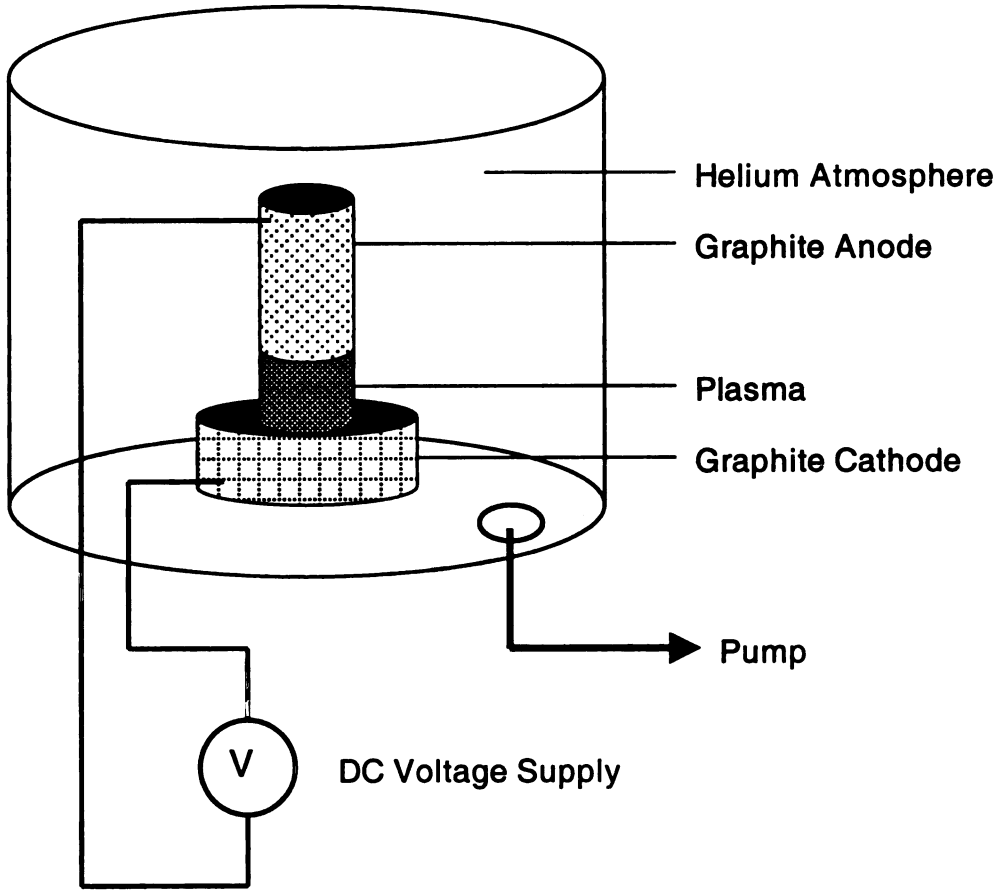

Figure 2-6: Schematic diagram of arc discharge.

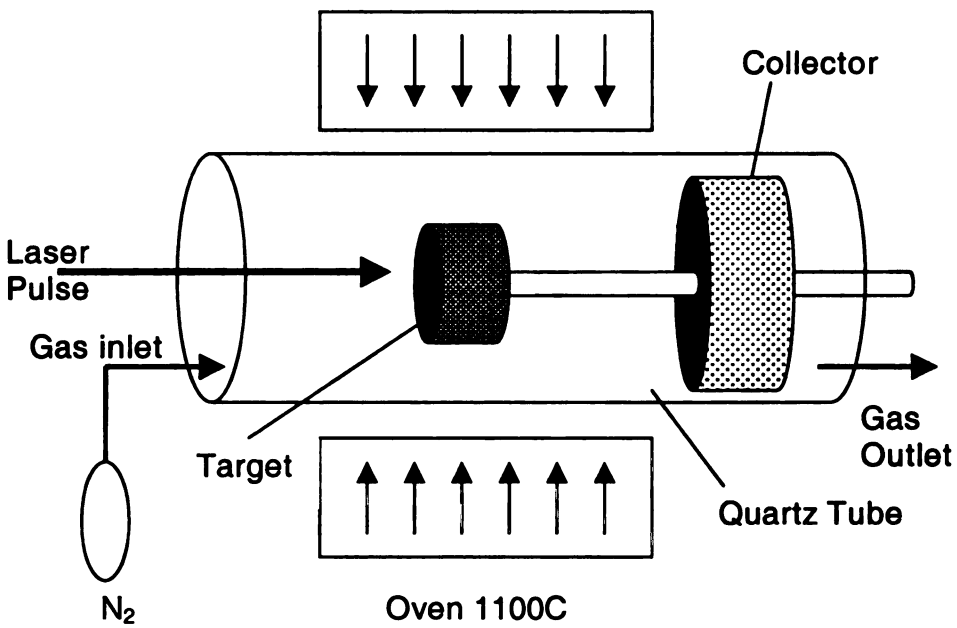

Figure 2-7: Schematic diagram of laser ablation.

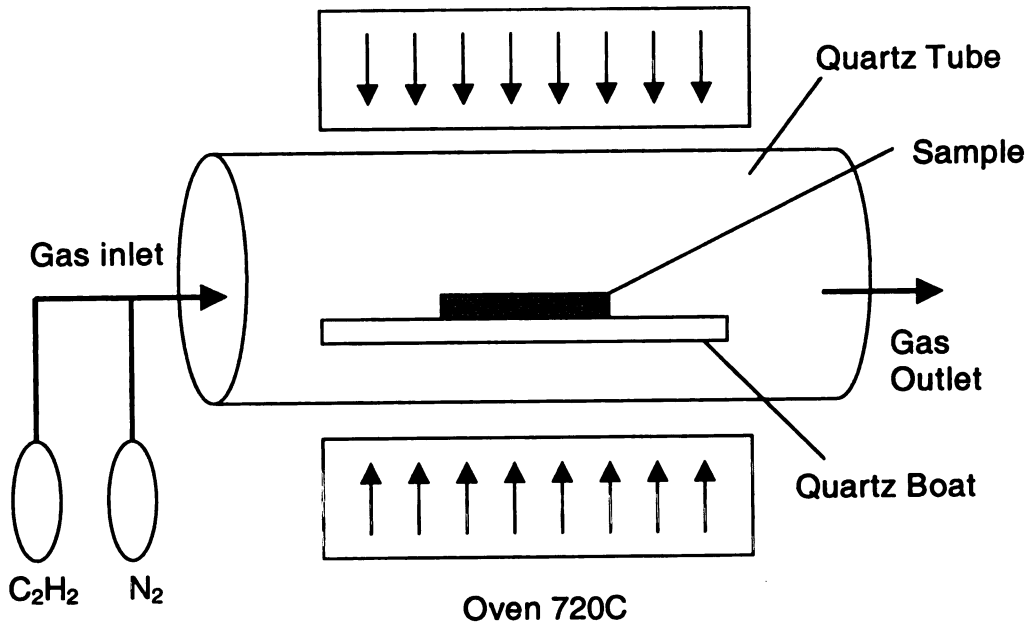

Figure 2-8: Schematic diagram of catalytic growth.

Another important factor is the current flowing through the two electrodes. The current is usually in the range of 50 – 100 A. Too high a current will result in a hard, sintered material with few free nanotubes. The current should be kept as low as possible, consistent with maintaining a stable plasma [113,114]. Efficient cooling of electrodes and the chamber has been shown to be essential in producing good quality nanotube samples and avoiding excessive sintering [115]. Iijima et al. and Bethune et al. reported that an arc discharge with a cathode containing metal catalysts (such as cobalt, iron or nickel) mixed to graphite powder resulted in a deposit containing SWNTs [17,116]. The yield of the method has been significantly increased by optimizing the catalyst mixture and the deposition conditions [19,117].

- **Carbon vapor condensation**

Another method to grow nanotubes using condensation of carbon vapor was demonstrated. An electron beam was used to evaporate graphite in a high vacuum (10^{-6} Torr), and collected the material which condensed on quartz [118]. Carbon vapor was produced by resistively heating a carbon foil, and the vapor was condensed onto highly oriented pyrolytic graphite, under a vacuum of 10^{-8} Torr [119]. The synthesis can be carried out in a horizontal flow tube under a flow of inert gas. The flow tube was heated to ~1200 C by a tube furnace as displayed in Figure 2-7. Laser pulses entered the tube and struck a target consisting of a mixture of

graphite and a metal catalyst such as Co or Ni. SWNTs condensed from the laser vaporization and were deposited on a collector outside the furnace zone [120].

- **Pyrolysis**

MWNTs can be produced by the pyrolysis of benzene in the presence of hydrogen. Benzene vapor and hydrogen were introduced into a ceramic reaction tube in which a graphite rod was positioned to act as a substrate. Microscope examination showed the presence of MWNTs similar in structure and quality to those produced by arc-evaporation, although the yield appeared to be low [121].

- **Electrochemical synthesis**

An electrochemical synthesis of MWNTs involved the electrolysis of molten lithium chloride using a graphite cell in which the anode was a graphite crucible and the cathode was a graphite rod. The cathode was immersed in the melt. A current was passed through the cell and then water was added to dissolve the lithium chloride and reacted with the lithium metal. Toluene was added to the aqueous suspension. The solid material resulted through the treatment contain large numbers of rather imperfect MWNTs. Both tubes and nanoparticles contained encapsulated lithium chloride or oxide [122].

- **Catalytic growth**

The catalytic growth of nanotubes is based on the decomposition of a hydrocarbon gas over a transition metal to grow nanotubes in a chemical vapor deposition (CVD) reactor, as in Figure 2-8. In general, the catalytic growth yields nanotubes of larger diameter as compared to the arc discharge, along with a crystalline structure that is not perfectly graphitized. The ends of the tubes are mostly open. For the production of MWNTs acetylene is usually used as source of carbon atoms at temperatures typically between 600 and 800 C. To grow SWNTs the temperature has to be significantly higher (900 – 1200 C) due to the fact that they have a higher energy of formation. Yield and average diameter of tubes were varied by controlling the process parameters [123]. The type of catalyst was found to control the formation of individual bundled tubes [124]. The catalytic method is ideally suited to grow films of nanotubes on planar substrates.

2.3.3 Field Emission from Carbon Nanotubes

Carbon nanotubes have attracted considerable attention as electron sources. Their high conductivity, sharp tip and long, narrow shape make useful field emitters, and some promising results have been achieved. The intrinsic structural and chemical properties of the individual tube play a role. The field emission behaviors for SWNTs [125,126,127] and MWNTs [13,128,129] were studied.

Table 2-4: Carbon nanotube field emitters.

Emitter	E_{to} [V/μm]	E_{thr} [V/μm]	J_{max} [Acm^{-2}]	Reference
MWNT	n.a.	<25	1	[13]
MWNT	n.a.	~15	10	[128]
MWNT	<2.7	~4.8		[129]
MWNT	~40	n.a.		[129]
MWNT	n.a.	20	3	[14]
Arc MWNT	n.a.	20	0.1	[130]
Arc MWNT	4.0	6.5		[136]
Arc MWNT	2.6	4.6		[137]
Arc MWNT	1.1	2.2		[8]
Arc MWNT	2.6	4.6		[8]
Arc MWNT	7.5	10	0.4	[138]
Arc MWNT	0.9	4		[139]
Arc MWNT	n.a.	1.5		[140]
Arc MWNT	2.4	n.a.		[131]
ta-C coated MWNT	1.6	n.a.		[131]
Open MWNT	4.5	30		[8]

Table 2-4: Continued.

Emitter	E_{to} [V/μm]	E_{thr} [V/μm]	J_{max} [Acm^{-2}]	Reference
SWNT	1.5	3.9		[125]
SWNT	n.a.	2.4		[126]
SWNT	n.a.	4 – 7	4	[127]
SWNT	2.1	n.a.		[141]
SWNT	2.8	5.2		[8]
CVD MWNT	1.7	n.a.		[142]
CVD MWNT	n.a.	4.8 – 6.1		[143]
CVD MWNT	n.a.	3.5		[126]
CVD MWNT	n.a.	2.1		[144]
CVD MWNT	4.8	6.5	0.1 – 1	[9]
CVD MWNT	n.a.	>5		[145]
CVD MWNT	3	6.6		[146]
CVD MWNT	1.6	5		[147]
CVD MWNT	3	5.6		[147]

Table 2-4: Continued.

Emitter	E_{to} [V/μm]	E_{thr} [V/μm]	J_{max} [Acm^{-2}]	Reference
CVD MWNT	n.a.	5.2		[148]
CVD MWNT	2.54	n.a.		[149]
CVD MWNT	1.5	n.a.		[150]
CVD MWNT	5.8 – 7.7	9.4 – 11.3	1.5	[151]
CVD MWNT	0.75	1.6	1 – 3	[152]
CVD MWNT	9.8	14.4		[132]
CVD MWNT	2.2	3.3		[132]
CVD MWNT	3.6	5.3		[132]
Graphitic fibers	1.8	4		[153]
Graphitic fibers	5.6	14		[8]
Graphitic fibers	2.1	n.a.	0.2	[154]

E_{to} and E_{thr} are the turn-on and threshold fields needed to produce an integrated current density of 10 $\mu A/cm^2$ and 10 mA/cm^2, and J_{max} is the maximum current obtained without destruction of the emitter. n.a. means that the value is not indicated or could not be deduced from the figures.

Differences in field emission were found depending on the geometry [8], fabrication methods [9,130], and surface treatment [131] as well as between closed and open tubes [8]. The density and orientation of the tubes on the film influenced also the emission [8,129]. Field emission was investigated on patterned films with different densities [132]. The low density film showed a rather inhomogeneous emission pattern with very few sites emitting. A much more homogeneous emission with a large number of emission sites was obtained for a medium density. A film of high density yields a result similar to the low density film. In addition to the work on arrays of nanotubes, field emission was carried out on an individual tube [8,133]. This enabled to determine the field emission characteristics of an individual tube. It was found that field emission was dramatically enhanced when the tube was opened by laser vaporization or oxidation [134]. A flat panel display was demonstrated employing a nanotube-epoxy composite as the source [135]. A summary of field emission from different types of nanotubes is given in Table 2-4.

2.3.4 Luminescence from Carbon Nanotubes

Rinzler et al. detected a very faint luminescence at the tip of individual opened nanotube [134]. Individual nanotube was attached to graphite fiber electrodes. The tip of tube was opened either by laser heating in high vacuum to near sublimation temperature (~3000 C) or by exposure to several militorr of O_2 while laser-heating the tip to 1000 to 1500 C. The field emission ranged from 0.5 to 1.5 μA at −100 to −110 V bias with 1 mm separation. The nanotube

incandesced dimly at the tip. The structures responsible for the incandescence were individual linear carbon chains that had pulled out from the open edges of the graphene sheets of the nanotube as shown in Figure 2-9. The dim incandescence was due to the carbon chains heated by the emission current. The tube was biased substantially above –110 V and field emitting more than 2 μA suffered catastrophic burn-back events. This produced a single bright streak. The incandescent flash that illuminated the side of the nanotube was caused by resistive heating of the outermost layer unraveling down the side of the tube. Bonard et al. observed light emission during electron field emission on SWNT and MWNT films [155]. The light was emitted from the vicinity of the apex of the tip. The light intensity was increased with emitted current. Luminescence was not homogenous on the emitting surface as the intensity variations were detected. Figure 2-10 showed the spectra acquired at different emitted currents. The peak intensity and widths were varying between 1.73 and 1.83 eV and between 0.3 and 1 eV, respectively. For SWNT films, light was emitted at higher energies as compared with MWNTs, but their behavior was comparable to those of MWNTs. Theoretical calculations showed that the local density of states at the tip presented sharp localized states with well-defined energy bands. It was thus suggested that the luminescence was due to electronic transitions between energy levels at the tip that are participating in the field emission.

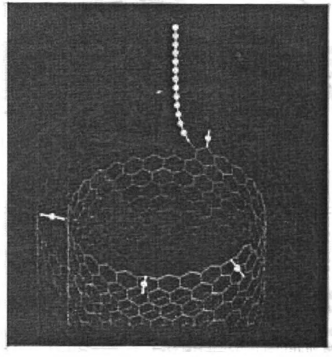

Figure 2-9: Model of the tip of a multiwalled nanotube.

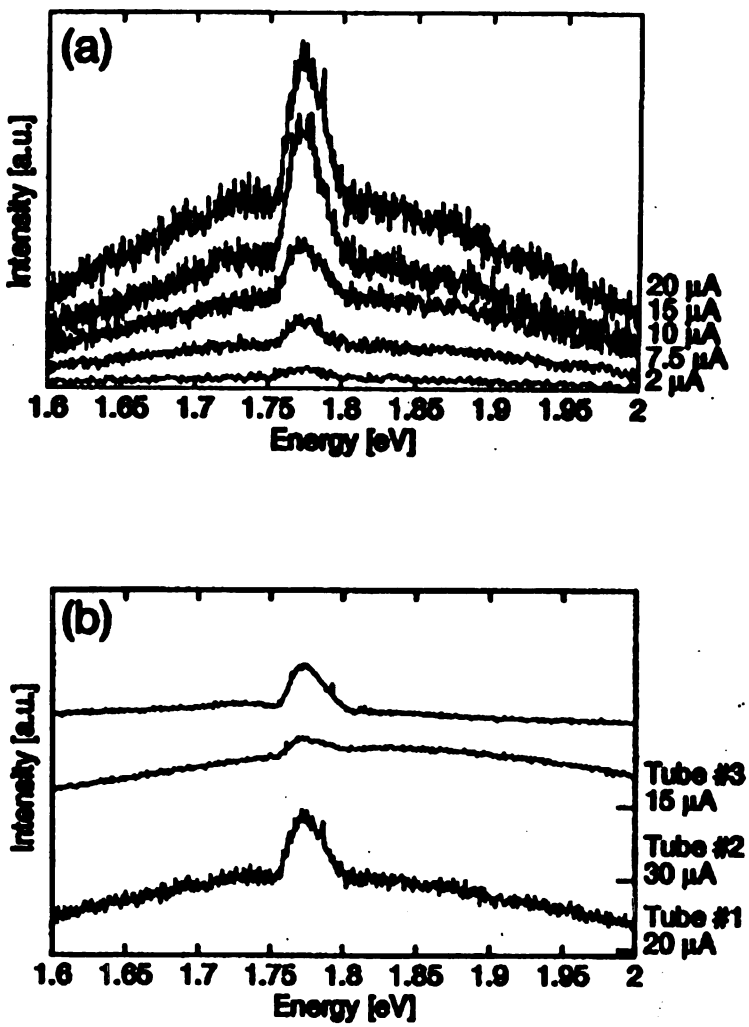

Figure 2-10: Luminescence spectra. (a) Variation of emitted current for MWNT. (b) Different MWNTs with different emitted currents.

CHAPTER 3

POLY-C TECHNOLOGY

3.1 Introduction

The fundamental technologies such as nucleation, patterning, deposition, doping, post-growth treatment, and characterization used in the study are discussed, as shown in Figure 3-1.

3.2 Fabrication System

Both poly-diamond and carbon nanotube films were synthesized using microwave plasma chemical vapor deposition (Model MPDR 313EHP, Wavemat, Inc.) with 2.45 GHz microwave generator up to 6 kilowatts. The schematic diagram is shown in Figure 3-2. The main parts of the system consist of;

(1) Cylindrical microwave cavity

(2) Process chamber

(3) Substrate holder

(4) Pressure

(5) Microwave source unit

(6) Gas supply unit

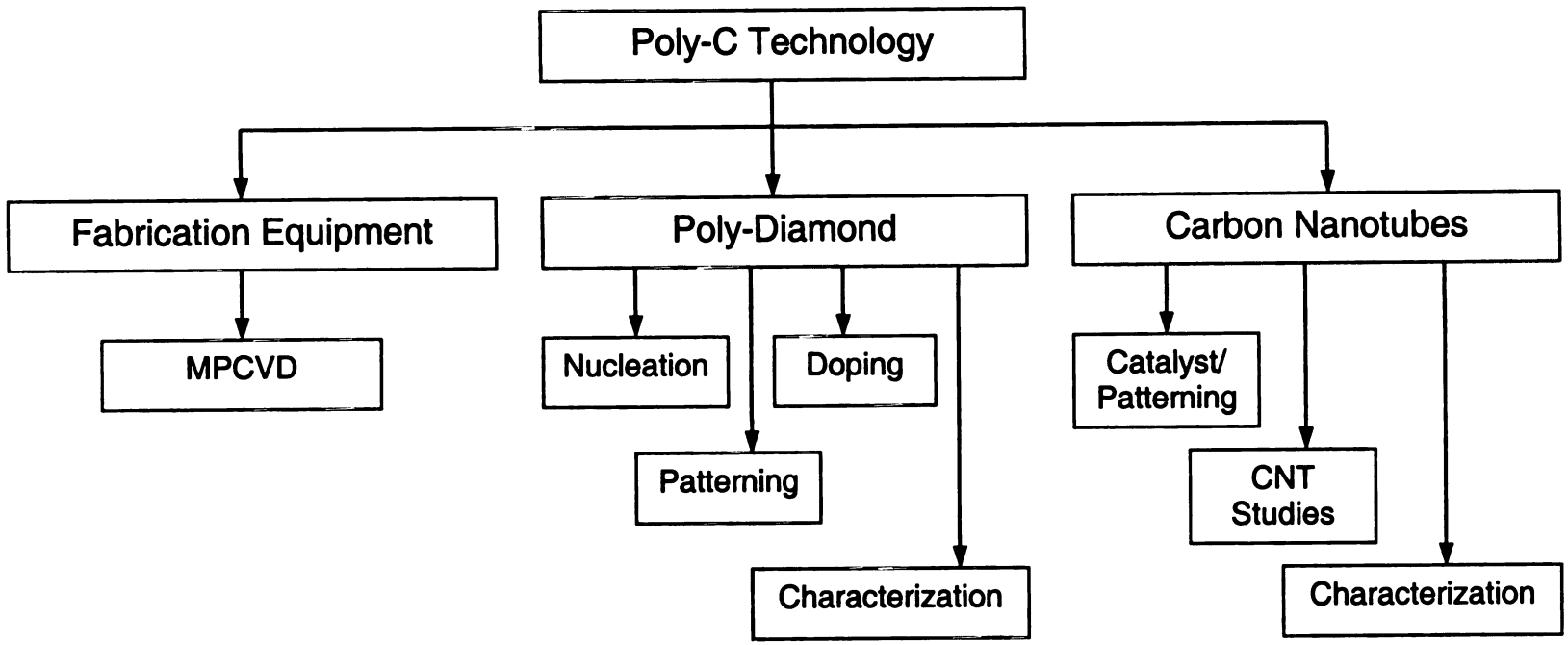

Figure 3-1: An overview of poly-C technology.

(1) Microwave cavity

The side view of the microwave cavity, the base plate, the substrate holder and the deposition chamber is shown in Figure 3-3. The diameter of the aluminum cylindrical microwave cavity was fixed at 17.78 cm and its height defined by L_S in Figure 3-3 was changeable to tune the microwave cavity. The cylindrical quartz dome inside the microwave cavity had dimensions of 5 inch diameter and 3.5 inch height. The microwave cavity was essentially a termination to the microwave transmission waveguide. The intensified microwave energy produced the plasma of the feed gases in a quartz dome inside the cavity. The cavity was designed to operate in the electromagnetic mode designated TM_{013}. This mode was found to provide optimum film deposition uniformity. The resonant condition of the cavity was mainly determined by the position of the cavity short and the microwave coupling probe. The short was the electrical top of the cavity and determined the overall length of the cavity, which in turn controlled the operating mode of the cavity. The position of the probe, defined by L_p in Figure 3-3, determined the electromagnetic fields near the cavity wall and hence the coupling of the energy into the cavity. By tuning the positions of the short and probe, the impedance of the plasma discharge/microwave cavity was matched to that of the transmission waveguide, producing a resonant condition. A well tuned cavity would show little or no reflected microwave power.

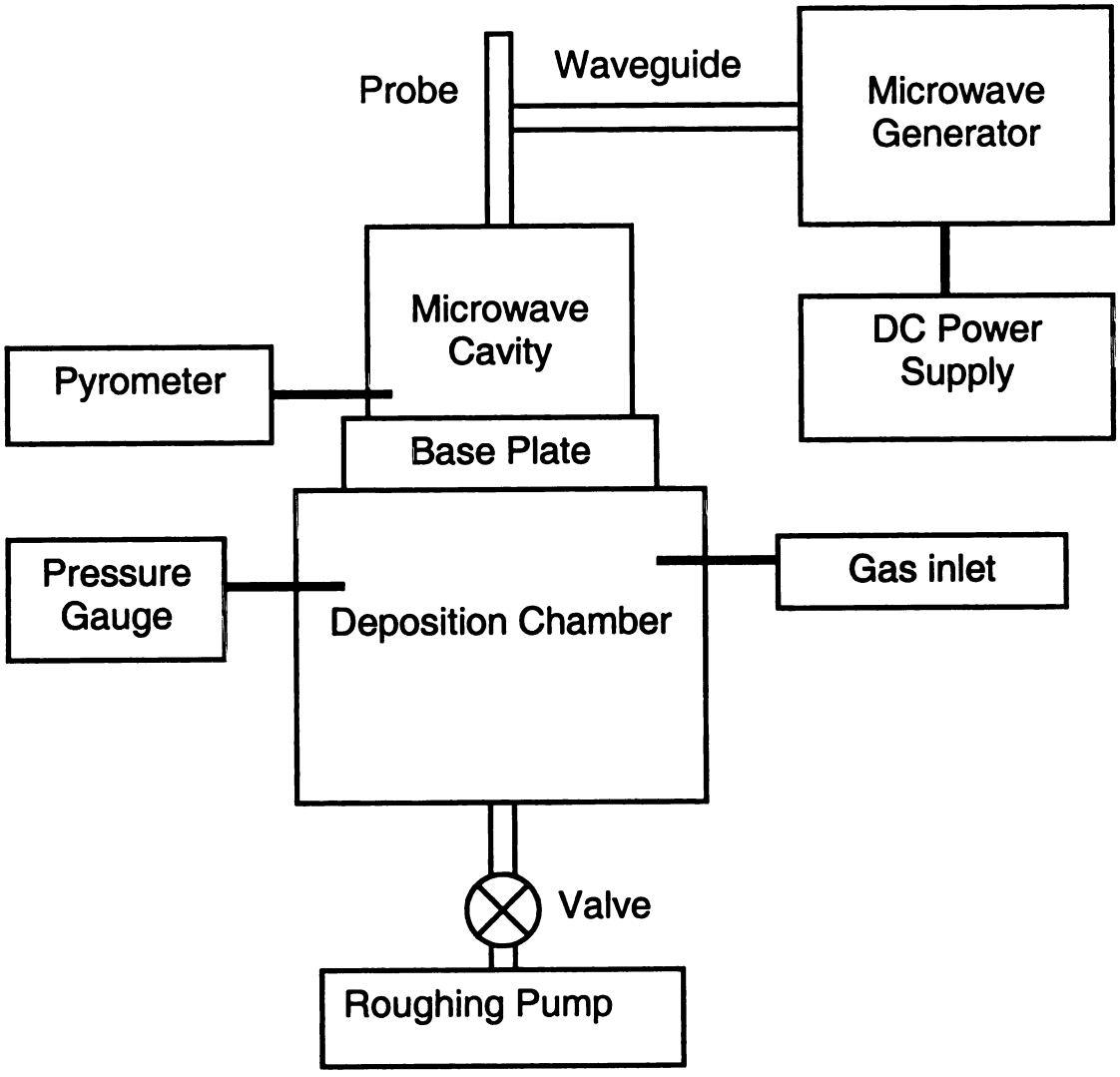

Figure 3-2: Schematic diagram of MPCVD system.

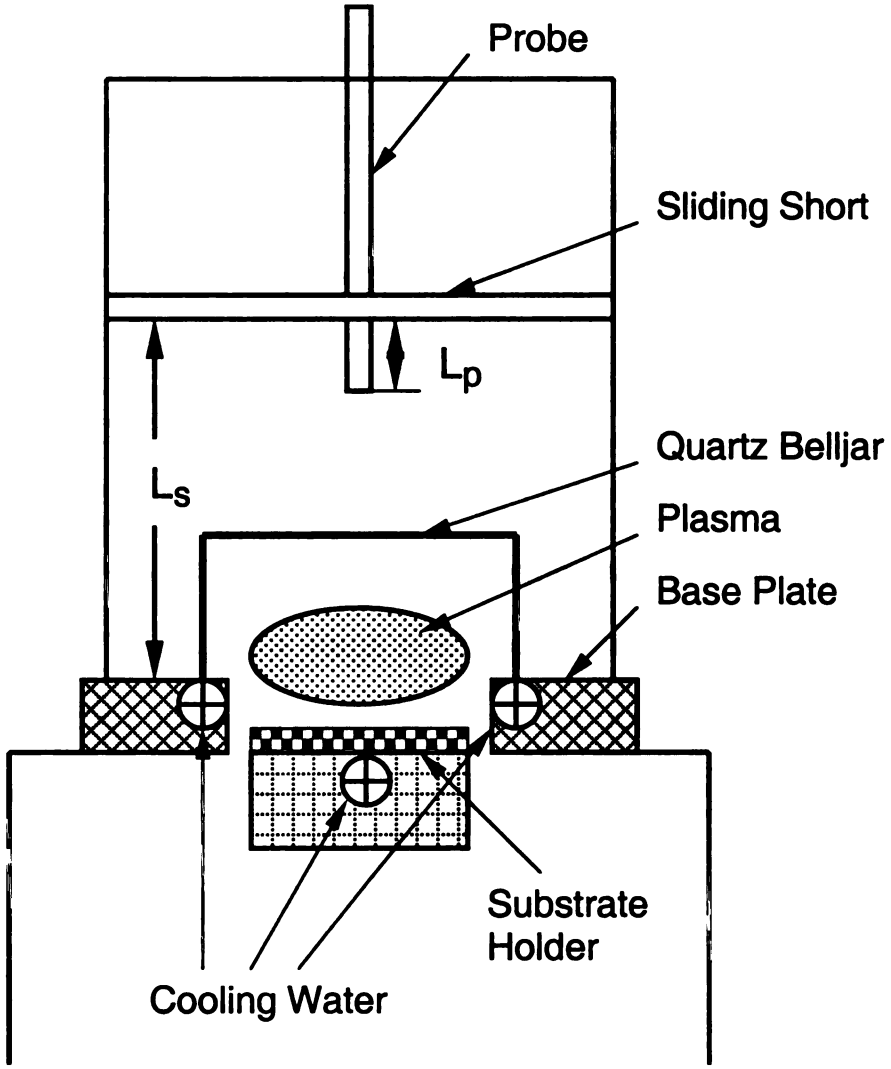

Figure 3-3: The side view of the microwave cavity, the baseplate, and the deposition chamber of the system.

The power supplied to the cavity should be increased to the desired power level only after the cavity operation in the desired mode has been verified. Water was used to cool the cavity walls, sliding short, coupling probe, and base plate. The jet pump (Model 9K862A, Dayton motors) was used to increase the inlet pressure. The thermocouples (Type K, Omega Engineering, Inc.) were used to monitor the temperature of the microwave cavity, base plate, quartz dome, short, and probe.

(2) Process chamber

The process reactor consisted of a 17 inch high, 18 inch O.D. stainless steel chamber. The sample can be loaded and unloaded through a 10 inch front door. The sample stage attached to the base plate by sliding through two guiding rods. Cooling water of the sample stage, vacuum gauges, and electrical feedthrough were assembled through 2.75 inch Del-Seal ports.

(3) Substrate Holder

Graphite or molybdenum was used as a substrate holder and accommodates 4 inch substrate. The substrate holder had active cooling, so the temperature of the substrate was decreasing with cooling. The substrate temperature was observed by the infrared thermometer (Model OS3707, Omega Engineering, Inc.).

(4) Pressure

Three capacitance manometers (Type 622A, MKS Instruments, Inc.) were used to measure the pressure in the chamber. The pressure controller (Type 651, MKS Instruments, Inc.) read the pressure transducer and controls the throttle valve (Type 653, MKS Instruments, Inc.) to achieve the desired deposition pressure. A base pressure of 10 mTorr was achieved with the mechanical pump (Model SD-300, Varian Inc.). N_2 was used to purge and backfill the chamber.

(5) Microwave source unit

The microwave source unit consisted of a DC power supply (Model GMP60KSM, Sairem), a microwave power controller (Model PIL408, Sairem) and a magnetron (Model GMP60KSM, Sairem). A DC power supply drove a magnetron source producing waves with frequency 2.45 GHz. The power supply was able to deliver power between 0.6 to 6 kW. The microwave power circulated from the magnetron source to the plasma, but diverted the reflected power to the matched load where it was absorbed. Hence, the magnetron head was protected against any reflected power on the transmission line.

(6) Gas supply unit

The reacting gases were ultra high pure grades (99.999% purity). The gas supply unit consisted of four mass flow controllers (Type 1159B, MKS Instruments, Inc.) and a flow readout unit (Model 247C, MKS Instruments, Inc.) to control the flow of the processing gases. Source gases were mixed before reaching the inlet on the baseplate.

3.3 CVD Diamond Technology

The fabrication of CVD diamond is categorized into nucleation, patterning, and doping. The technologies used and developed for the study are investigated in detail.

3.3.1 Nucleation

Diamond has been shown to nucleate on a wide variety of materials. Due to the low nucleation density on non-diamond materials, the substrates are treated to enhance the nucleation density. The commonly used pre-treatment techniques are abrading [156,157], ultrasonic nucleation [158,159], bias enhanced nucleation (BEN) [160,161], and electrophoresis [162]. Diamond powder loaded fluids with different carrier fluids, diamond particle sizes, and densities are used to enhance the nucleation density for this study. The details of diamond particle loaded fluids are summarized in Table 3-1. N10 and DW (DuPont industrial diamond) are diamond particles dispersed in mainly water and suspending agent.

Table 3-1: Details of diamond powder loaded fluid

	N10	DW	DPR
Carrier Fluid	Water	Water	Photoresist
Mean Powder Size	10 nm	38 nm	100 nm
Density	250 carats/liter	40 carats/liter	12 carats/liter
Nucleation Density	$\sim 10^{11}$ cm^{-2}	$\sim 10^{10}$ cm^{-2}	$\sim 10^{8}$ cm^{-2}
Application Method	Brushing	Spray, spin or brushing	Spin

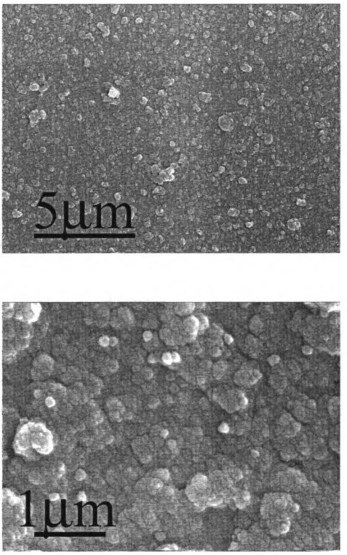

Figure 3-4: Diamond nucleated by brush-coating of N10.

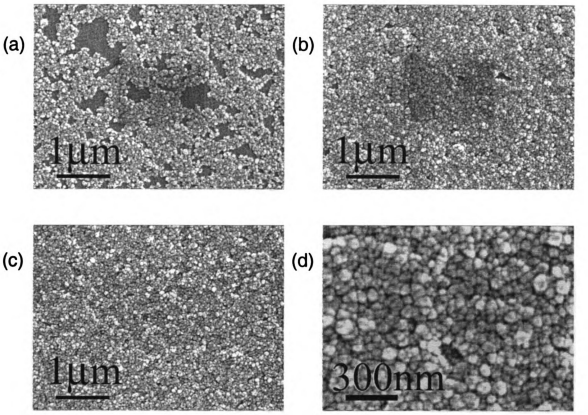

Figure 3-5: **DW spin coating; (a) spin/growth, (b) spin/growth/spin/growth, and (c,d) spin/growth/spin/growth/spin/growth. The sample is spun at 2500 rpm for 20 sec, followed by 5 min growth.**

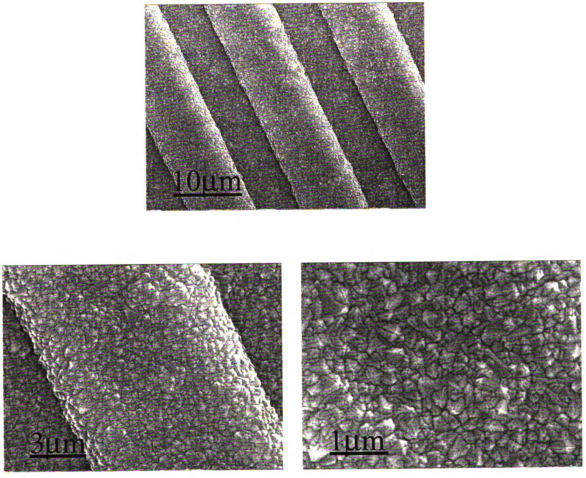

Figure 3-6: DW coated Si structures.

N10 and DW provided high nucleation densities resulting continuous film in a short growth time. Although the nucleation density was high, diamond film seeded by brush-coating of N10 exhibited diamond particle constellations as shown in Figure 3-4. This may be due to the applying method and the ultra high density of diamond particles in the fluid. DW was spin-coated in order to reduce the agglomeration of particles. Figure 3-5(a) shows diamond film after growth for 5 min at 800 C. No pinholes were observed after the seeding and growth sequence was repeated three times as seen in Figures 3-5(c) and (d). DPR was prepared by suspending fine diamond particles with a mean size of 0.1 μm into photoresist [163]. The uniform nucleation density of 10^8 cm^{-2} was achieved. The advantages of DPR method include simplicity of application, compatibility with standard IC fabrication process, and reproducibility.

3.3.2 Patterning

Various patterning techniques have been developed to fulfill the need of desirable structures in microelectronics and microsensor applications. Patterning of diamond is obtained through either selective deposition or selective etching.

The selective deposition is achieved by pre-deposition nucleation on the desired area, or by masking the undesirable area during the diamond deposition. Ar sputtering in undesired regions was used to suppress

nucleation after the substrate was pretreated by ultrasonic method [164]. ZnO, amorphorous silicon, SiO_2, and Si_3N_4 were used as a sacrificial layer for lift-off process to generate diamond patterns [165,166].

Reactive ion etching (RIE) [167], ion-beam-assisted diamond etching [168], bias-assisted etching [169,170], electron cyclotron resonance (ECR) plasma etching [171], and plasma enhanced etching [172,173,174] of chemical vapor deposition (CVD) diamond films in various gas mixture and different temperatures has been investigated. The etch rates varied widely from 6 to 300 nm per minute, depending on the process conditions. Excimer-laser etching and patterning of diamond was performed in the direct writing mode [175]. Graphitic layer was generated in the process of etching. Etch rate of 0.2 μm/pulse was achieved. Diamond etching was observed by exposing to oxygen plasma at the substrate temperature of less than 100 C using a Ni mask [176].

Most of the techniques either caused damages on the substrate surfaces or produced undesirable byproducts. Non-destructive and IC compatible patterning process has been developed at Michigan State University. DPR patterning technique and direct patterning system are described.

3.3.2.1 Photolithographic Method

The standard photolithography process can be employed in DPR patterning since DPR is photoresist mixed with diamond particles.

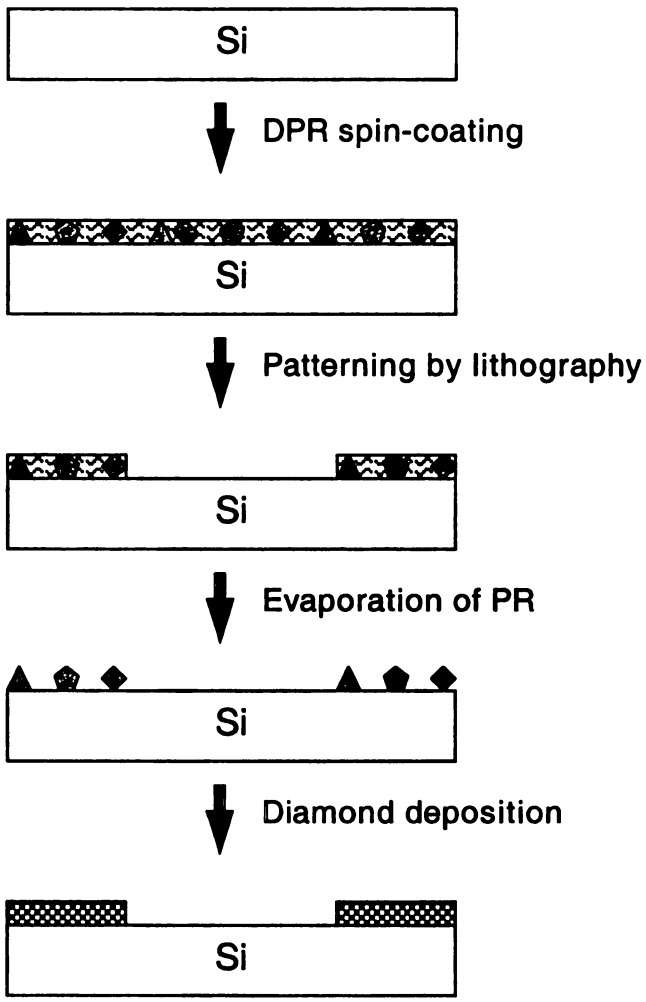

Figure 3-7: Schematic diagram of DPR patterning process.

The schematic diagram of DPR patterning procedure is shown in Figure 3-7. DPR was spin-coated on Si wafer at a spin speed of 3000 rpm for 30 sec, which gave 1μm thick layer, and patterned by photolithography (Model MJB3, Karl Suss). A 200 W mercury short-arc lamp was used. Primary exposure wavelengths were 350 – 500 nm. The aligner performed exposures in a soft contact mode. The carrier fluid was evaporated at the initial stage leaving behind diamond particles which acted as seeds for diamond growth.

3.3.2.2 Direct Patterning Method

Two methods are explored; a locally built direct patterning system and a commercially available printer modified to print seeding patterns.

❖ **Direct patterning system**

The direct patterning system was constructed and evaluated its performance. The block diagram of the system and the picture of substrate stages and nozzle are depicted in Figures 3-8 and 3-9. The system consisted of a computer controlled stage, flow controller unit, temperature controller unit, and a nozzle in a stainless steel vacuum chamber. The components that placed in the vacuum chamber were prepared to be vacuum compatible to minimize the contamination.

(1) Motion stage

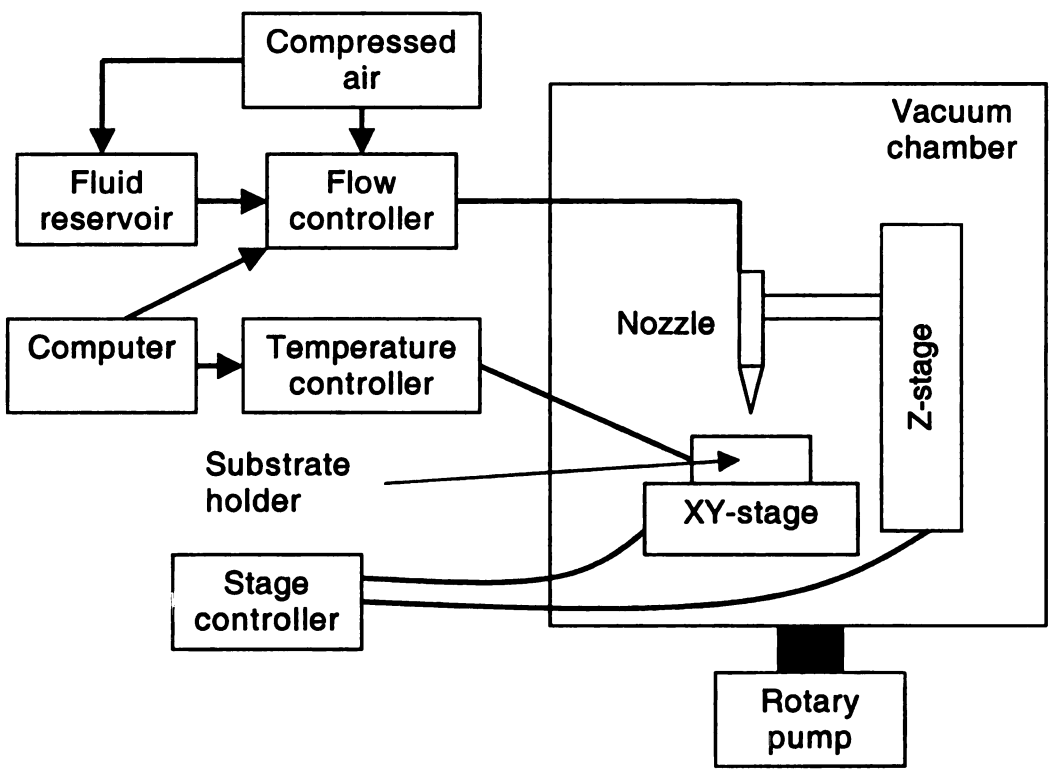

Figure 3-8: Schematic diagram of the direct patterning system.

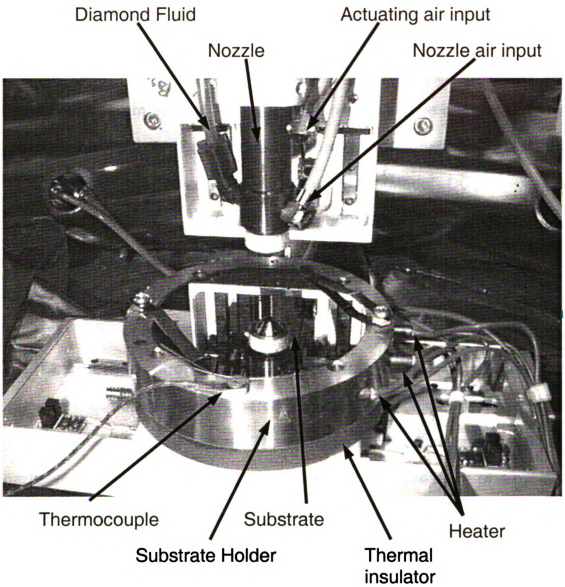

Figure 3-9: Substrate stage and nozzle.

Three manipulating stages (Model ATS-100, Aerotech, Inc.) with a linear resolution of 1 μm and a travel length of 100 mm for substrate and 50 mm for nozzle along with motion controller (Model U12R, Aerotech, Inc.) were used to control the positions of the substrate and the nozzle. The motion controller was interfaced with a computer via IEEE-488 interface. The cables coming from each of the three motion stages were connected to the motion controller via the 20-pin feedthroughs (Model IF20-275, MDC Vacuum, Inc.) with in-vacuum ribbon socket (Model DGCD-10, MDC Vacuum, Inc.). A ceramic disk spacer (Model CS20-2, MDC Vacuum, Inc.) was attached to the feedthrough to avoid accidental shorting of the pins.

(2) Flow controller unit

Compressed nitrogen was regulated into three different pressure regimes. The nozzle was triggered by an input gas with an optimal operation pressure of 70 - 90 psi. The pressure of atomizing gas for a spray nozzle was in the range of 15 – 20 psi. The nitrogen pressure of 4 psi was used to pressurize the diamond fluid. A solenoid valve (Honeywell) controlled the on/off of compressed nitrogen, thus determined the open time of the nozzle. The solenoid valve was interfaced with a computer via an electrical solid state relay through RS-232. The fluid from reservoir flowed to the nozzle via fluid feedthrough (Model LF-275, MDC Vacuum, Inc.). The schematic diagram of flow controller unit is shown in Figure 3-10(a).

(3) Temperature controller unit

Four round tubular heaters with single end terminals (Omega Engineering, Inc.) were inserted into the stainless steel substrate holder to achieve uniform heating over the sample area. The temperature controller (Model CN371-KC2, Omega Engineering, Inc.) was utilized to maintain a constant substrate temperature during seeding. A thermocouple (Type K, Omega Engineering, Inc.) connected to the temperature controller monitored the substrate temperature. A 0.5 inch thick thermal insulating material was inserted between the heating plate and the motion stages. The schematic diagram of temperature controller unit is given in Figure 3-10(b).

(4) Nozzle

Two different nozzles, needle valve (Model 740V-SS, EFD)and spray valve (Model 780S-SS, EFD), were evaluated to study diamond nucleation and patterning. The detail specifications of the nozzles were shown in Figures 3-11 and 3-12. The amount of fluid that flows was determined by the valve open time, fluid pressure, flow control adjustment, dispense tip output size, and fluid viscosity. During operation of a needle valve, controlled pulsed air acted on the position to withdraw the needle a preset distance from the needle seat providing fluid flow. The stainless steel shut off needle seat in the hub of dispensing tip so that fluid cutoff is as close as possible to the dispensing orifice.

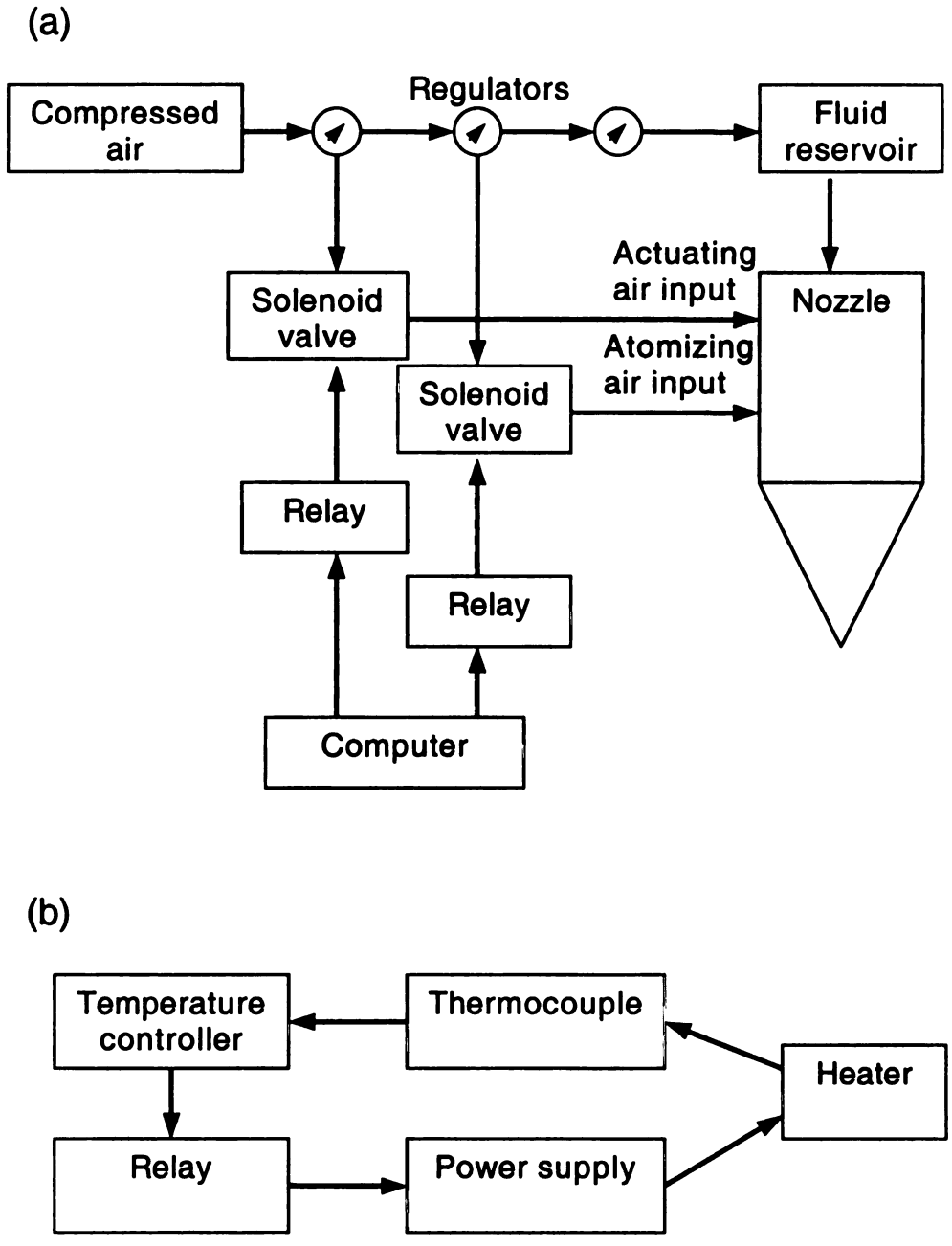

Figure 3-10: Block diagrams of (a) flow controller unit and (b) temperature controller unit.

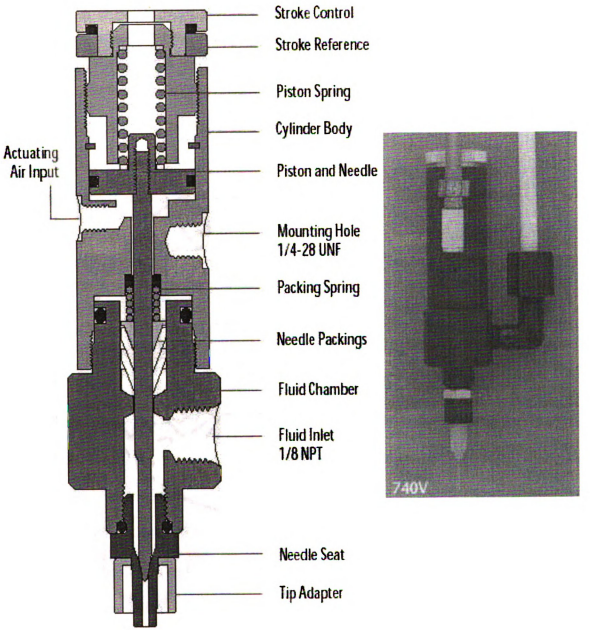

Figure 3-11: Detail specification of needle valve.

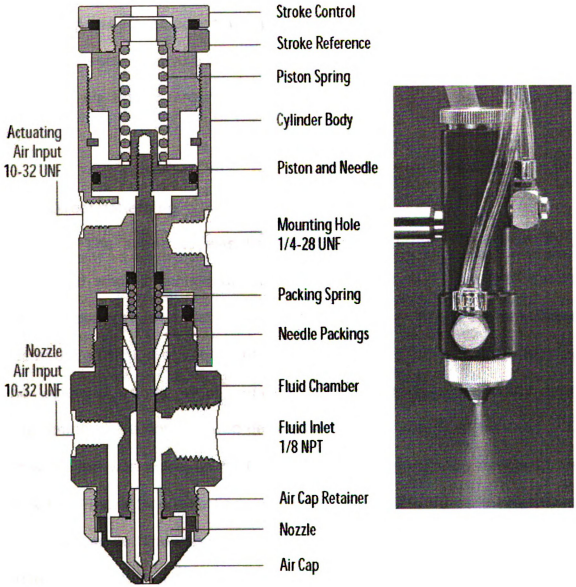

Figure 3-12: Detail specification of spray valve.

A spray valve provided round patterns with diameters ranging from 3/16 to 3 inches (4.8 to 76.2 mm). The combination of adjustable fluid flow, adjustable nozzle air, and post-air cutoff provided spray control. Actuating input air pressure acted on the piston that retracted the stainless steel precision needle from the nozzle, allowing liquid to flow. Simultaneously, atomizing air flowed around the nozzle, dispersing the liquid into fine droplets.

❖ **Direct patterning**

The substrate was heated at 75 C so that the carrier fluid evaporated when it landed on the substrate surface. Figure 3-13 shows diamond patterns on 4 inch wafers by the direct patterning system. There was about a fraction of second of delay on the response of solid state relay and solenoid valve, which resulted of dispensing more fluids than programmed. The dot size was determined by the amount of the fluid. 330 μm wide line was achieved by DW using a 125 μm opening needle tip as shown in Figure 3-14. The line width could be controlled by the speed of the motion stage. The faster the stage moves, the thinner the line gets. The circles of diameter of 1 cm were drawn by DPR with the same size needle tip. DPR patterns expanded on the Si surface. DW coating by spray nozzle did not cover uniformly over the substrate as seen in Figure 3-15(a). The size of droplets was in the range of less than a micron to 30 microns.

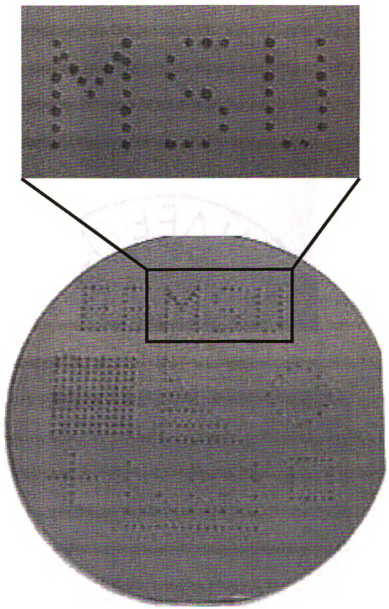

Figure 3-13: Diamond patterns on 4 inch substrate using direct patterning system.

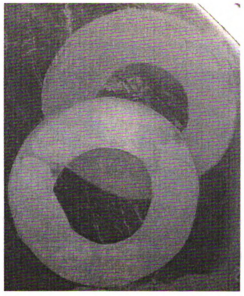

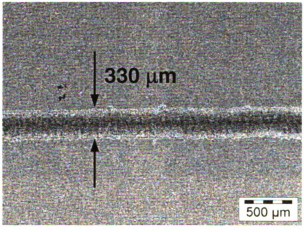

Figure 3-14: Diamond patterns by needle valve.

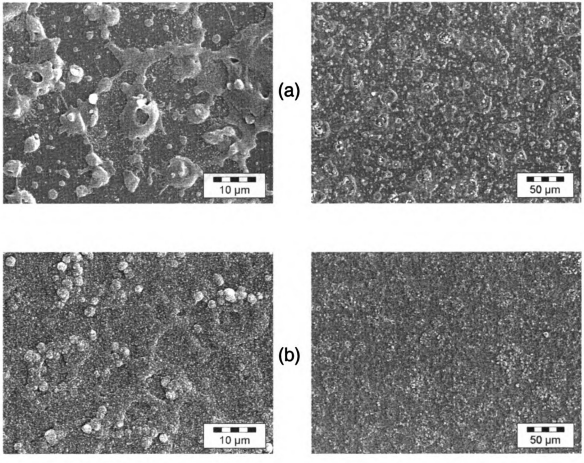

Figure 3-15: Diamond coated by spray nozzle.

(a)

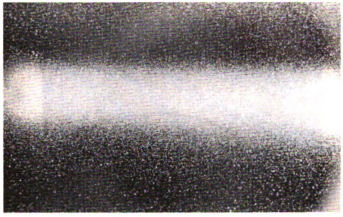

(b)

Figure 3-16: Line patterns by spray nozzle.

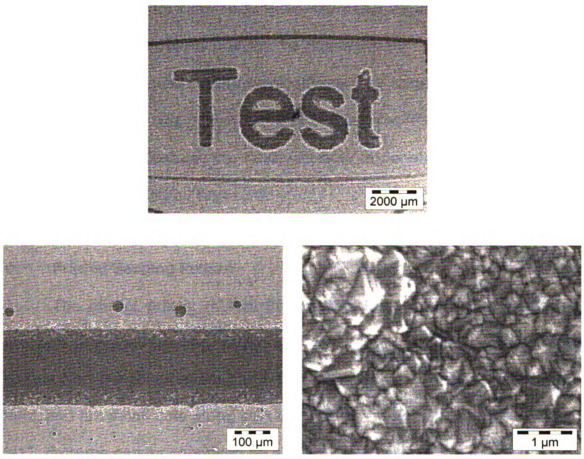

Figure 3-17: Diamond patterns generated by printer.

Big droplets exhibited circular shape with more particles along the perimeter. This was caused by the surface tension of carrier fluid. The atomizing air controlled the size of the liquid droplets. Figure 3-15(b) shows the diamond film coated by spray nozzle with optimized conditions. The roughness of the film still needs to be improved. Figure 3-16(a) shows a 5 mm line obtained by spray nozzle. The line is not well defined. The 400 and 600 μm lines in Figure 3-16(b) were obtained by spraying fluid through a shadow mask that was in contact with a substrate. The edges of the lines were not straight because the fluid was able to penetrate under the mask by the high atomizing air pressure.

❖ **Printed Seeding Pattern**

The ink jet printer (Model Stylus C60, Epson) was investigated to produce diamond seeding patterns. A cartridge was filled with DW. The patterns on the Si substrate shrank because of the surface tension of the fluid, and left small dots along side of the main patterns as shown in Figure 3-17. Patterns can be enhanced by a printer with better resolution.

3.3.3 Doping

Boron has shown to be an acceptor in diamond. Boron acceptor level lies 0.37 eV above the valence band. Although doping in diamond may be accomplished during deposition, diffusion, or ion implantation, there are some difficulties with diffusion doping and ion implantation. Diffusion

doping of diamond is difficult because of the low diffusivity in diamond [177]. The diffusion of boron into diamond was achieved [178]. However, the penetration depth of boron was only 50 nm. The boron diffusion coefficient in diamond is 100 times smaller than the one in Si. Ion implantation is also difficult because of residual damage to the diamond [179]. If the damage exceeds a critical threshold, then a subsequent anneal will produce graphite. Reliable boron doping in diamond has been successfully accomplished through in situ doping during deposition [180,181].

The resistivity of diamond decreased as the average grain size of the diamond films decreased [182,183]. It was found that heavy doping was deleterious in the early stage of diamond growth, but did not degrade growth on an existing high quality diamond [184]. Trimethylboron [$B(CH_3)_3$, TMB] was used as boron doping source of diamond films, which was less toxic than B_2H_6. TMB is in the vapor state at room temperature, and is easily diluted by argon, helium, hydrogen, nitrogen, and silane gases.

In this study, doping of diamond was carried out by 0.1% TMB diluted in H_2 by MPCVD. The resistivity was measured from four point probes (Model S-301, Signatone) with a probe separation of 62.5 mils. The resistivity values were averaged over a number of measurements. All measurements were performed at room temperature. Figure 3-18 illustrates the change of resistivity as a function of TMB flow.

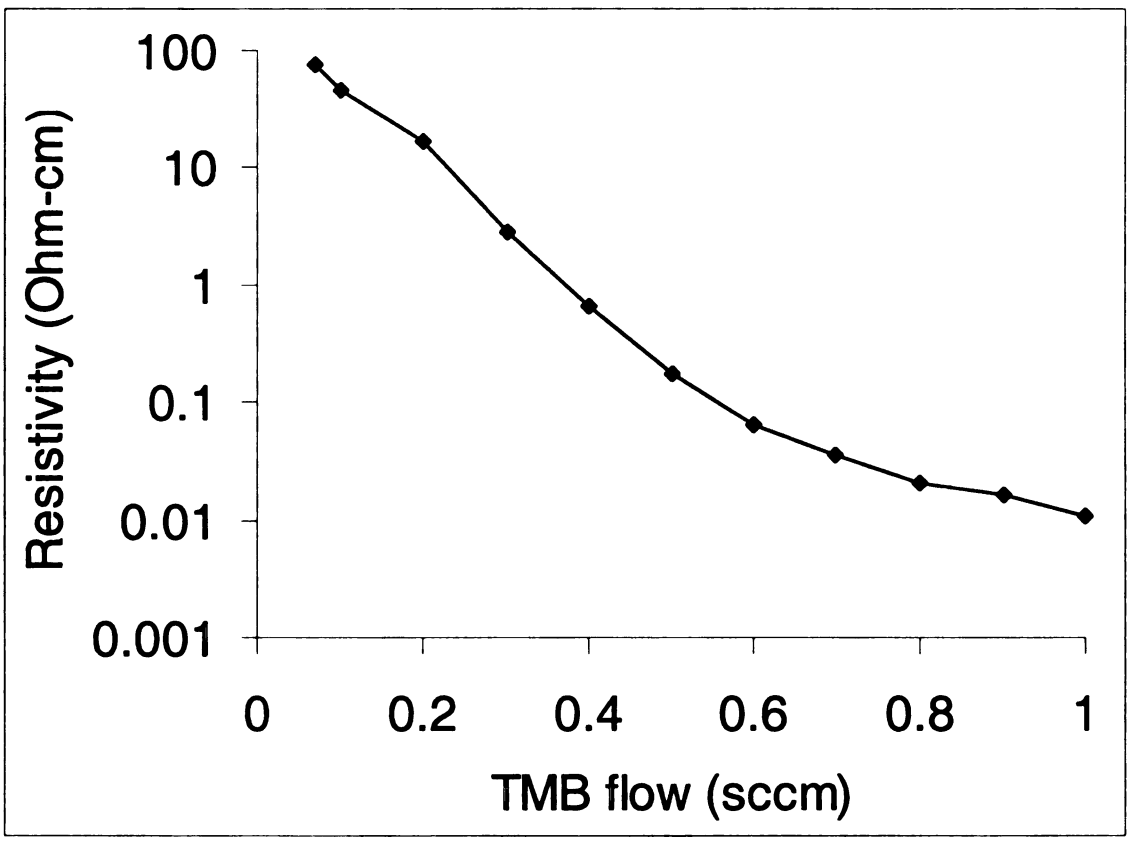

Figure 3-18: Resistivity versus TMB flow.

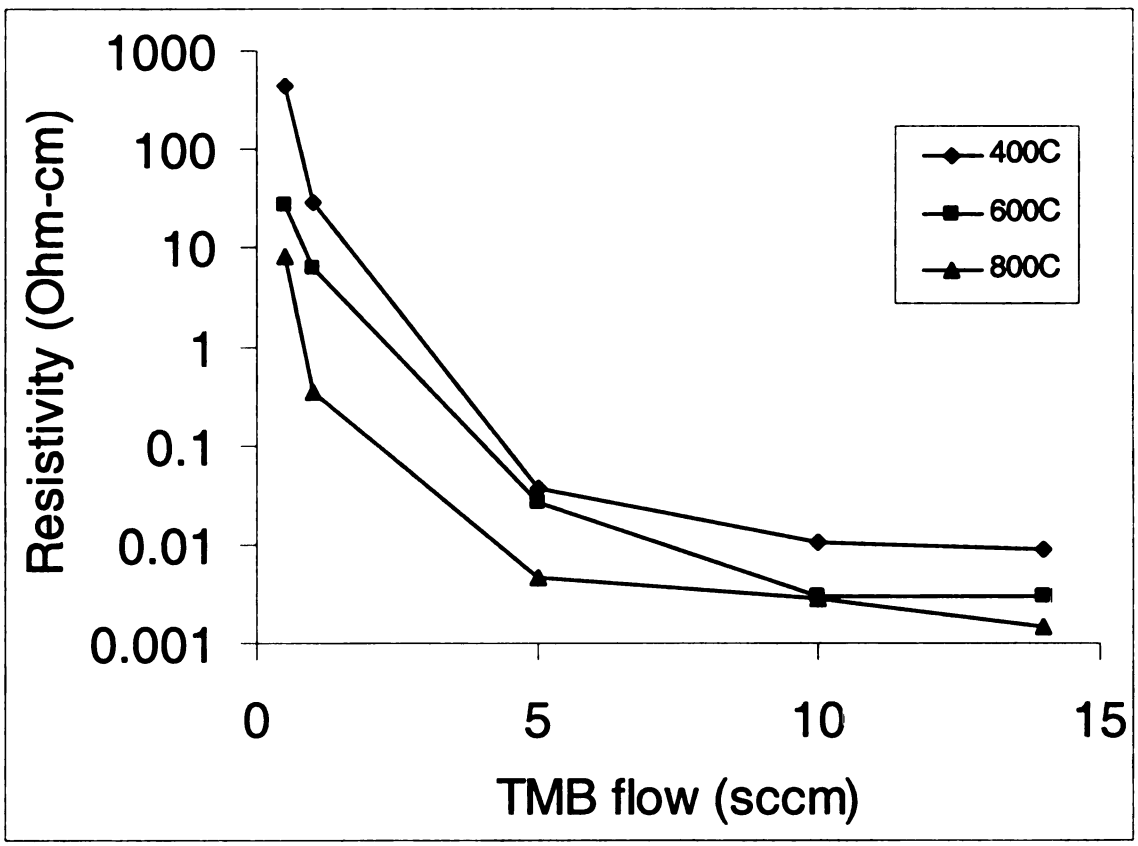

Figure 3-19: The growth temperature dependence of resistivity.

B-doped diamond was deposited on undoped diamond at 800 C for 2 hours with 1.5% CH_4. The resistivity decreased as TMB flow increased and reached about 0.01 Ωcm. The resistivity changes by nearly four orders of magnitude. Although the conduction is mainly due to the boron doping, the segregation of boron and graphitic phase formed in grain boundaries may also attribute to the reduction of resistivity. The resistivity of the films measured as a function of deposition temperature for various doping level is shown in Figure 3-19. As expected, the resistivity was higher with decreasing of growth temperature. The impurities and defects incorporated in the films deposited at low temperature may contribute in the conduction as the quality of CVD diamond degrades with decreasing substrate temperatures.

3.3.4 Characterization

A careful characterization is necessary to control and enhance the quality and properties of the diamond films deposited by CVD. Raman spectroscopy, scanning electron microscopy, and atomic force microscopy as characterization tools are described in detail.

- **Raman spectroscopy**

The Raman spectroscopy is widely used in the analysis of materials, and the identification of trace elements [192,193]. The wavenumber shift of 1332 corresponds to sp^3 diamond peak. The Raman system (R-2001, Ocean

Optics, Inc.) consists of a diode laser, a focused probe, a CCD-array spectrometer, an analog-to-digital converter, and operating software. The 532 nm green laser with a power of 50 mW is used. The optical resolution is ~15 cm^{-1}. The focused probe consists of 90 μm excitation fiber and 200 μm collection fiber. The focal length of the probe is 5 mm.

- **Scanning electron microscopy (SEM)**

The SEM consists of an electron gun (LaB_6) in a vacuum chamber column and images by collecting the secondary electrons emitted from samples due to the incident electron beam [194]. It has a large depth of field which can be up to four hundred times greater than that of a light microscope. It is widely utilized to inspect the surface morphology, crystal orientation, the grain sizes, nucleation density, and film thickness. The need for a conducting specimen somewhat limits its utility for undoped films. The environmental SEM (ESEM) is developed to overcome the disadvantage. ESEM maintains the sample chamber in a near-atmospheric environment more conductive to examination of wet samples and non-conducting samples, and has a completely different environment, high vacuum, in the remainder of the column.

- **Atomic force microscopy (AFM)**

The AFM is another useful tool for studying the nucleation density, crystal structure, and surface morphology of films. A very fine tip, mounted

on a cantilever, is scanned through the sample to obtain the surface profile. The advantages of AFM are high resolution and great sensitivity to define profile differences of vertical variations in the sample [196]. In addition, no vacuum is needed for the operation of AFM, and it can be used on non-conducting surfaces.

3.4 Carbon Nanotube Technology

In the present study, we make use of the many control parameters accessible in an MPCVD reactor to selectively grow nanotubes with particular morphologies and orientations. Similar to all other nanotube synthesis techniques, incorporation of defects cannot be avoided during the growth. A post-growth cleaning process is usually required before using the nanotubes in device structures.

3.4.1 Catalyst/Patterning

Iron, nickel, and cobalt were commonly used as catalysts for carbon nanotube growth [185,186,187]. For this study, iron (Fe) or nickel (Ni) was used as transition metal catalysts on titanium (30 nm) coated Si substrates. A thin film of Ni or Fe (100 nm) was sputter deposited. Ferric nitrate ($Fe(NO_3)_3$) as iron source was dissolved in methanol, Fe coating was applied by dipping the substrate into the Fe solution. The patterning of carbon nanotubes was achieved by growing tubes on patterned catalyst.

3.4.2 Growth Study

Various shapes of carbon nanotube growth were obtained by varying synthesis conditions. Purification process is discussed.

3.4.2.1 Growth

The flexibility of the MPCVD system, which permits a modification of plasma shape through tuning of the cavity, allows synthesizing a wide variety of carbon allotropes, ranging from nano-diamond [188] to nanotubes. Nanotubes were fabricated by MPCVD. Typical parameters varied in this study were growth temperature (450 – 900 C), growth time (0.5 - 120 min), atmosphere ($N_2/H_2/CH_4$), and pre- (N_2/H_2) and post-growth treatment. An overview of nanotube structures grown under varying deposition parameters is summarized in Table 3-2. There was no appreciable nanotube growth below 600 C. For growth temperatures in the range of 800 - 900 C, etching of carbon nanotubes was observed. A very uniform growth was achieved at temperatures between 650 C and 750 C. As shown in Figure 3-20(a), clusters were formed on top of the nanotubes during deposition at 650 C. The diameters of tubes grown under these conditions were in the range of 20–100 nm, implying multi-wall nanotubes. Energy-dispersive spectroscopy (EDS) indicated the presence of carbon in these clusters, as shown in Figure 3-21. A gold peak was due to the thin Au coating on the sample to improve the resolution of the image in SEM.

Table 3-2: Summary of carbon nanotube growth conditions.

Specimen	Catalyst	Growth parameters					Tube diameter (nm)
		Pre-growth treatment	Process gas flow (sccm)	Temp.	Growth time	Substrate	
Figure 3-20(a)	FN*(3g) in MT#(30ml)	5min at 650C in H_2/N_2	$H_2(90)/N_2(10)$ $/CH_4(6)$	650 C	15 min	Fe/Ti/Si	20 – 100
Figure 3-20(b)	FN*(3g) in MT#(30ml)	5min at 750C in H_2/N_2	$H_2(90)/N_2(10)$ $/CH_4(6)$	750 C	15 min	Fe/Ti/Si	100 – 400
Figure 3-22	FN*(3g) in MT#(30ml)	5min at 650C in H_2/N_2	$H_2(90)/N_2(10)$ $/CH_4(6)$	~650 C	15 min	Si/Ti/Fe	20 – 80
Figure 3-23(a)	FN*(3g) in MT#(30ml)	5min at 650C in H_2/N_2	$H_2(90)/N_2(10)$ $/CH_4(6)$	650 C	0.5 min	Fe/Ti/Si	20 – 100
Figure 3-23(b)	FN*(3g) in MT#(30ml)	5min at 650C in H_2/N_2	$H_2(90)/N_2(10)$ $/CH_4(6)$	650 C	120 min	Fe/Ti/Si	20 – 100
Figure 3-24(a)	FN*(2g) in MT#(20ml)	5min at 650C in H_2/N_2	$H_2(90)/N_2(10)$ $/CH_4(2)$	650 C	10 min	Fe/Ti/Si	20 – 100
Figure 3-24(b)	FN*(2g) in MT#(20ml)	5min at 650C in H_2/N_2	$H_2(90)/N_2(10)$ $/CH_4(8)$	650 C	10 min	Fe/Ti/Si	20 – 100
Figure 3-25(a,b)	FN*(3g) in MT#(30ml)	No	$H_2(90)/N_2(10)$ $/CH_4(6)$	650 C	15 min	Fe/Ti/Si	20 – 100

* FN: Ferric Nitrate
\# MT: Methanol

Table 3-2: Continued.

Specimen	Catalyst	Growth parameters					Tube diameter (nm)
		Pre-growth treatment	Process gas flow (sccm)	Temp.	Growth time	Substrate	
Figure 3-25(c,d)	FN*(3g) in MT#(30ml)	5min at 650C in H_2/N_2	$H_2(90)/N_2(10)$ /$CH_4(6)$	650 C	15 min	Fe/Ti/Si	20 – 100
Figure 3-26(a)	FN*(450mg) in MT#(15ml)	5min at 650C in H_2/N_2	$H_2(90)/N_2(10)$ /$CH_4(6)$	650 C	15 min	Fe/Ti/Si	20 – 100
Figure 3-26(b)	Ni thin film	5min at 650C in H_2/N_2	$H_2(90)/N_2(10)$ /$CH_4(6)$	650 C	15 min	Ni/Ti/Si	60 – 100
Figure 3-27	FN*(450mg) in MT#(15ml)	5min at 650C in H_2/N_2	$H_2(90)/N_2(10)$ /$CH_4(6)$	650 C	15 min	Fe/etched Ti/Si	20 – 80
Figure 3-29	FN*(450mg) in MT#(15ml)	5min at 650C in H_2/N_2	$H_2(90)/N_2(10)$ /$CH_4(6)$	650 C	15 min	Fe/patterned Ti/Si	20 – 100
Figure 3-30	FN*(2g) in MT#(20ml)	5min at 650C in H_2/N_2	$H_2(90)/N_2(10)$ /$CH_4(6)$	650 C	15 min	Fe/patterned Ti/Si	20 – 100
Figure 3-31(a,b)	FN*(2g) in MT#(20ml)	5min at 650C in H_2/N_2	$H_2(90)/N_2(10)$ /$CH_4(6)$	650 C	30 min	Fe/Ti/Si	20 – 100

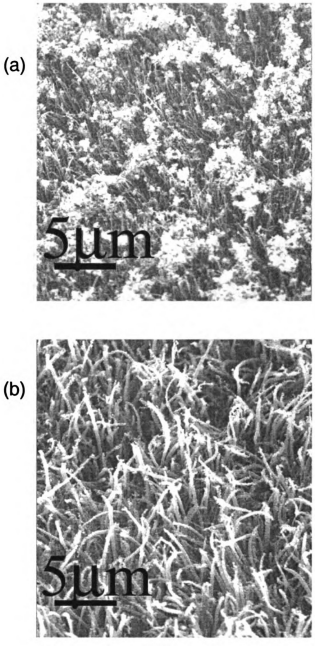

Figure 3-20: Carbon nanotubes grown for 15 min at (a) 650 C and (b) 750C.

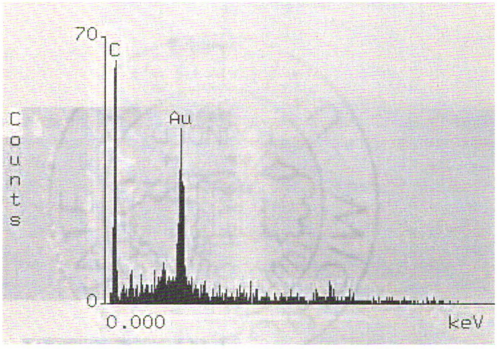

Figure 3-21: Energy dispersive spectroscopy of clusters deposited on carbon nanotubes.

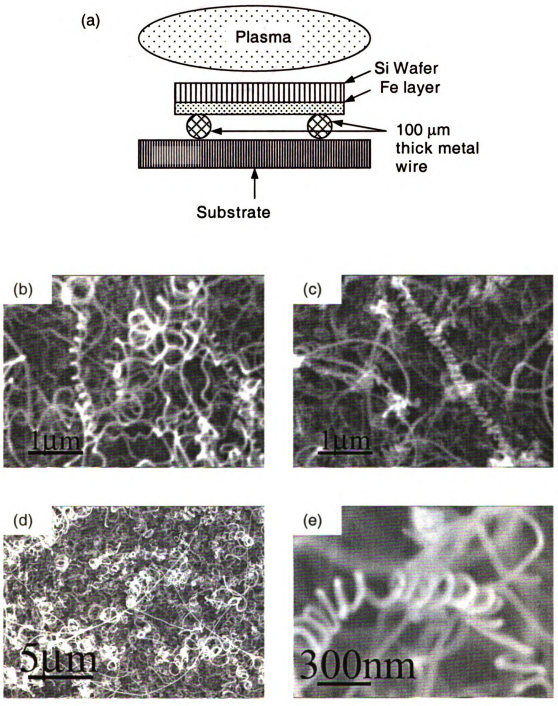

Figure 3-22: (a) Schematic diagram of growth setup and (b,c,d,e) spiral growth of carbon nanotubes.

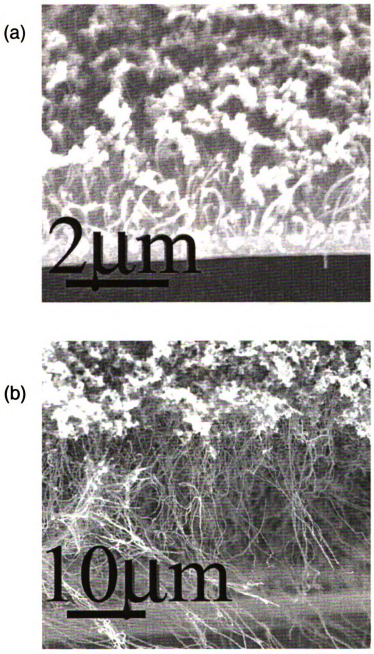

Figure 3-23: Carbon nanotubes grown for (a) 30 sec and (b) 120 min.

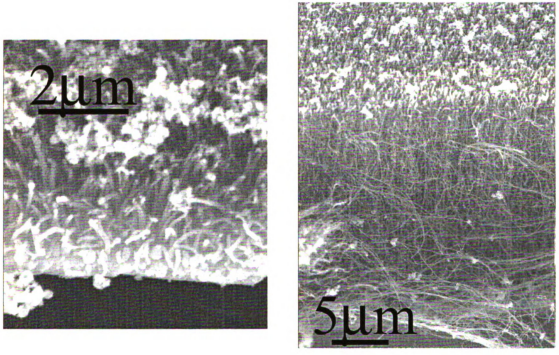

Figure 3-24: Carbon nanotubes grown for 10 min with (a) 2% and (b) 8% CH_4 in H_2 and N_2.

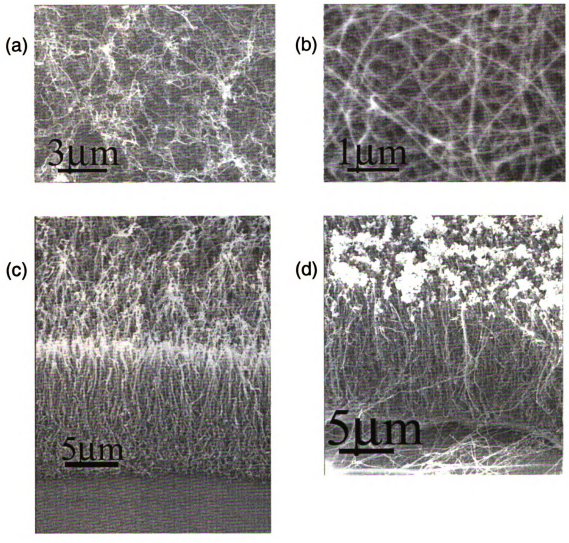

Figure 3-25: (a,b) Lateral growth and (c,d) vertical growth of Carbon nanotubes.

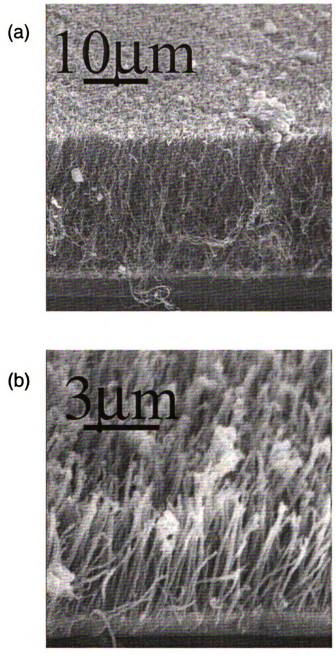

Figure 3-26: Carbon nanotubes grown for 15 min at 650 C on (a) Fe and (b) Ni coated substrates.

Increasing the deposition temperature to 750 C reduced the size of these clusters, but increased the diameter of the tubes to 100–400 nm as shown in Figure 3-20(b). We interpreted this diameter increase by improved growth kinetics at higher temperatures, in agreement with other study [189]. The build-up of clusters was strongly suppressed if nanotubes were grown by placing the Fe-coated substrate upside down, leaving a gap between the growing surface and the substrate holder. In this case, tubes were grown downward and the plasma has to reach the growing surface. The processing pressure and applied microwave power were 32 Torr and 1650 Watts, respectively. Spiral growth of nanotubes was observed with 100 μm separation as shown in Figure 3-22. At the growth temperature of 650 C, the tube lengths were found to increase from approximately 1 μm to over 100 μm if the growth time was increased from 30 sec to 120 min, as seen in Figure 3-23. The tube diameter was not affected by the growth time. Also in this case, terminating clusters can be clearly seen. Figure 3-24 shows that methane concentration certainly affects the growth rate. Both vertical and horizontal growth of nanotubes was observed. A pre-growth treatment of Fe catalyst in nitrogen plasma enhanced vertical growth as shown in Figure 3-25. The effect of Fe and Ni as a catalyst was investigated, while keeping the growth parameters the same. Although the growth on Fe or Ni yielded similar ranges of diameters, density and orientation (vertical or horizontal), the growth rate was faster for Fe than

that for Ni, consistent with the higher catalytic activity of Fe. Morphology of nanotube films grown on Fe and Ni is shown in Figure 3-26.

Different nanotube shapes were obtained when the substrate was etched by a mixture of sulfuric acid (1 part) and hydrogen peroxide (1part) for a minute before applying the Fe coating. This treatment lead to "macaroni" shapes with a hollow core, which appeared to be woven out of very fine nanotubes, as seen in Figure 3-27. This technique has the potential of creating different types of "fibers" made of nanotubes.

Transmission electron microscopy (TEM) was used for accurate measurements of the tube diameter. As seen in Figure 3-28, TEM images of nanotubes grown at 650 C showed two distinct features, namely a straight hollow and a repeating arrowhead shape. For straight hollow tubes, the width of hollow region was in the range of 11–55 nm, with a wall thickness in the range of 20-38 nm depending on the tube diameter. The tip of the arrowhead was in the range of 8-12 nm, while the wide side of arrowhead was in the range of 15-30 nm. It is interesting to know that the average tube diameter was different from the hollow structures. The tubes with a straight hollow core were about 20 nm larger in diameter than the ones with an arrowhead shape. The tip of the tubes was tapered and closed. The black spots on the walls seemed to be the structural defects generated during growth. As shown in Figure 3-29 and Figure 3-30, patterned substrates such as a gear and 250 x 250 μm^2 square were used to deposit nanotubes selectively.

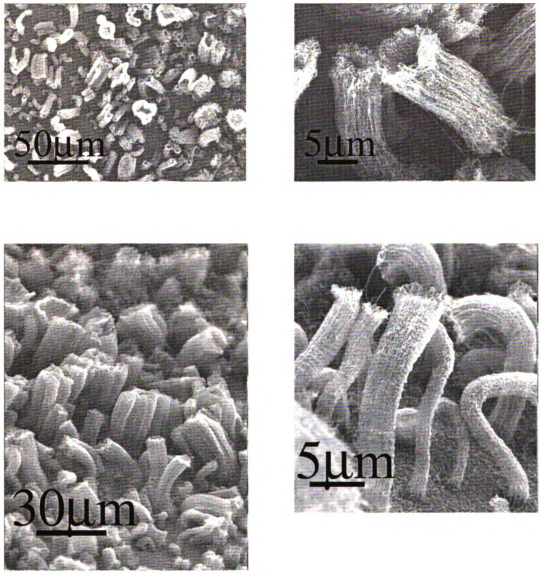

Figure 3-27: Macaroni shape of carbon nanotubes.

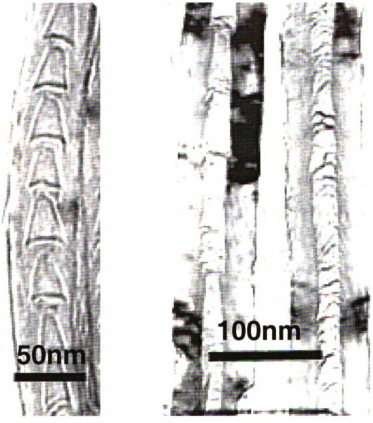

Figure 3-28: TEM micrographs of carbon nanotubes.

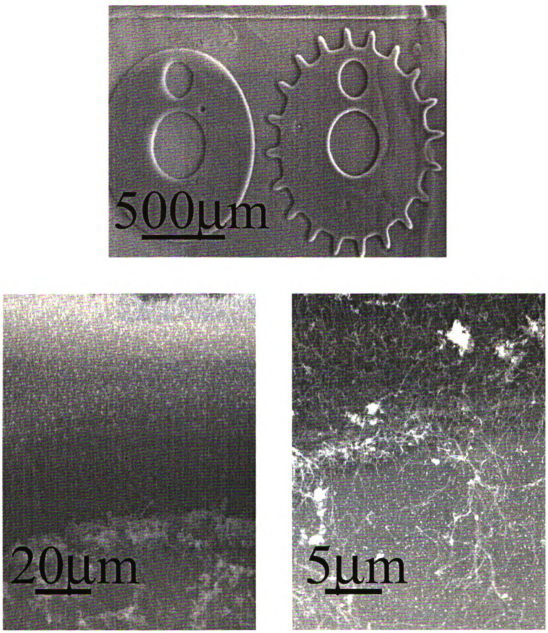

Figure 3-29: Gear patterned carbon nanotubes.

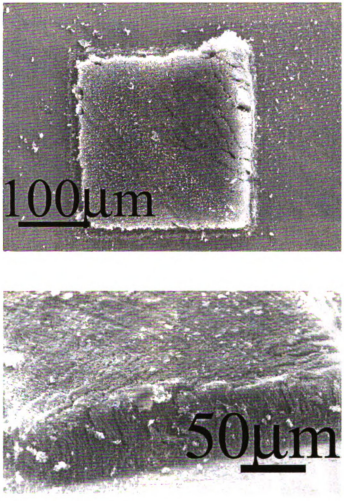

Figure 3-30: Square patterned carbon nanotubes.

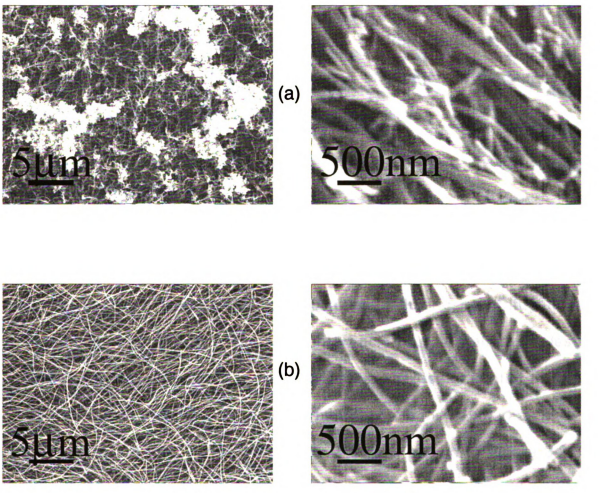

Figure 3-31: (a) As-grown carbon nanotubes and (b) carbon nanotubes subjected to ultrasonic treatment.

The substrate was treated in H_2/N_2 plasma at 650 C for 5 minutes, followed by exposure to CH_4. The growth lasted for 15 min. SEM observations indicated that carbon nanotubes were also grown outside of the patterned area, as seen in Figure 3-29. This might be caused by that titanium on the substrate, which enhanced the adhesion of iron particles, was not completely etched away. The alignment and orientation of nanotubes in Figure 3-30 were uniform across the deposited area.

3.4.2.2 Purification

Previously reported purification methods [190,191], designed to remove clusters and other undesirable structures from the nanotube material, involved laborious steps such as refluxing, centrifugation, sedimentation and filtration, or boiling in an acid bath. An alternate, less laborious way to purify CVD grown nanotubes was demonstrated in this study. It involves treatment of as-grown nanotubes in methanol in an ultrasonic bath for 15 min. Tubes cleaned in this way, shown in Figure 3-31, became free of the cluster residue. CVD grown nanotubes adhered well to the substrate, thus suggesting their application as field electron emitters.

3.4.3 Characterization

Carbon nanotubes exhibited two Raman peaks at 1350 and 1580 cm^{-1}. The growth orientation, diameter, length, and density of tubes were

inspected by SEM. In addition to Raman spectroscopy and SEM as described in section 3.3.4, TEM was utilized to characterize the carbon nanotubes.

- **Transmission electron microscopy (TEM)**

The TEM produces a transmitted electron image of a thin specimen, magnified from 100 to approximately 500000 times, and with a resolving power of approximately 0.2 nm [195]. To produce the standard bright-field TEM image, the electron beam must be able to penetrate the sample. A TEM is used to obtain high-resolution images of fine internal structures of carbon nanotubes.

3.5 Summary

MPCVD was employed to fabricate poly-diamond and carbon nanotube films. Diamond was nucleated by different particle densities and particle sizes. The patterning of diamond was performed by photolithography and direct patterning system. The direct patterning system was constructed and evaluated its capability. The uniform coating and 330 μm line was obtained. The conventional printer was tested for diamond patterning. The resistivity was achieved in the range of 0.001 – 450 Ωcm using TMB as boron doping source. High density of carbon nanotubes with different morphologies was synthesized by varying the deposition conditions in a MPCVD reactor. A cleaning procedure,

consisting of ultrasonic treatment of nanotubes in methanol, was found to efficiently remove any amorphous residue formed during the synthesis.

CHAPTER 4

FIELD EMISSION CHARACTERIZATION

4.1 Introduction

The detail of the field emission characterization system is described. The field emission and field emission mapping studies from poly-diamond and carbon nanotube are discussed.

4.2 Field Emission Characterization System

The field emission characterization system was designed and built locally. It consists of vacuum chamber, pumps, pressure gauges and readouts, power supply, measurement instruments, and computer controlled xyz-stages. The schematic of the system is shown in Figure 4-1. The system can be categorized into the following subsystems.

(1) Chamber

(2) Vacuum system

(3) Pressure

(4) Motion stage

(5) Measurement setup

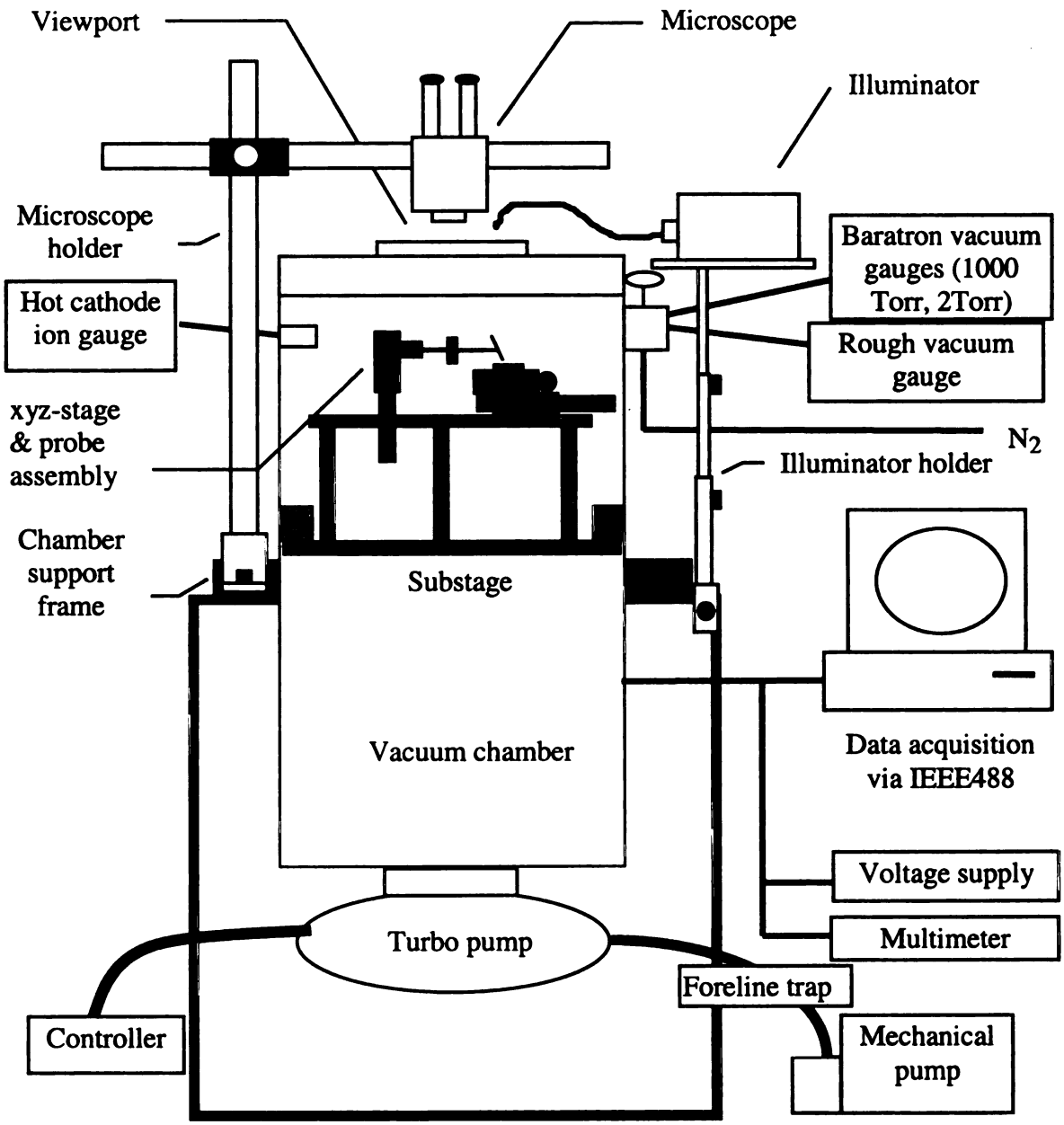

Figure 4-1: Setup of field emission characterization system.

(1) Chamber

The height and inner diameter of the vacuum chamber were 26 inches and 15 inches, respectively. There was a glass view port attached to the top plate which allows monitoring of the sample setup inside the chamber from above. This was accomplished by an optical microscope (Model Stereo Zoom 5, Bausch & Lomb) with a magnification of 10x attached to a custom built microscope holder. Sample illumination through the viewport was accomplished via a fiberoptic illuminator (Model 1177E, Reichert Jung).

(2) Vacuum system

The chamber was connected to a turbopump (TPU330 with TCP300 controller, Balzers) with a rotary vane backing pump (Model 5KC49ZG1412, General Electrics). The mechanical pump can be shut off by means of an inline valve in the forevacuum connection.

(3) Pressure

The pressure inside the system was monitored by a Baratron gauge (Type 122A, MKS) from atmospheric pressure down to 1 Torr, and a thermocouple gauge (Type DC-3M, MDC) for rough vacuum pressures from 1000 mTorr to 1 mTorr. Then a hot cathode ion gauge was switched on (IMR132 gauge head and IMG070 ion gauge controller, Balzers).

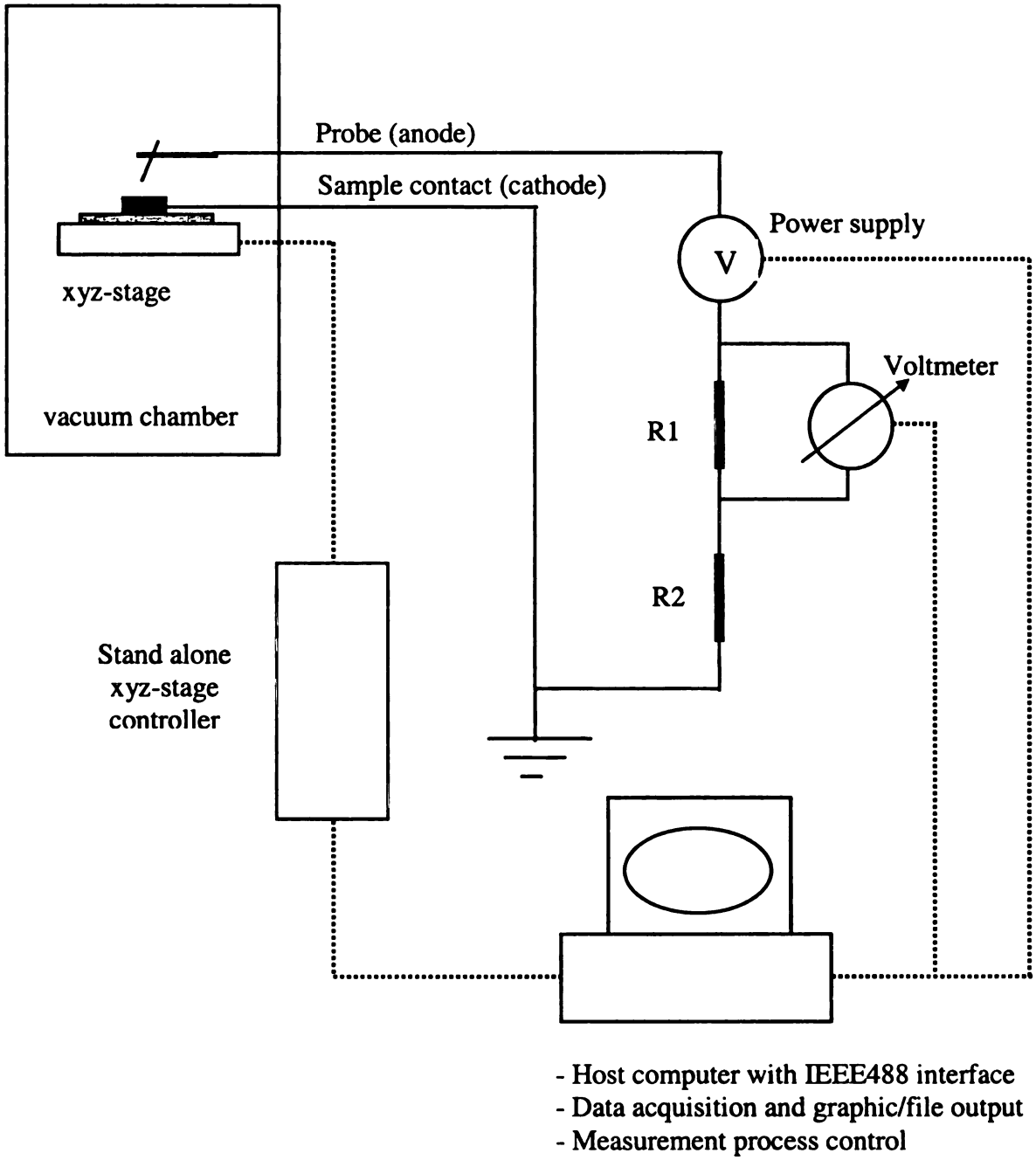

Figure 4-2: Electrical setup for field emission measurement.

The desired final pressure was below 10^{-7} Torr. The Baratron gauge, the thermocouple gauge, and the nitrogen venting valve could be shut off from the rest of the system by means of an inline valve (IV-150M, MDC).

(4) Motion stage

Inside the chamber a computer controlled xyz-stage (CTC-290-3, DynaOptic motion) made of Al with a travel range of 50 mm in each direction and a precision of 1 μm was mounted onto a custom built substage which allowed coarse and find adjustment. The 6-line flat cables coming from each of the three stage motors were connected to the inside contacts of the 20-pin feedthrough with screw-on inline barrels. The z-stage was mounted separately from the xy-stage. The probe tip (Signatone) was screwed to a brass probe holder with insulating Teflon intermediate layer. The insulation was required because the xyz-stage, the substage, and the chamber walls were all connected electrically conductive. The probe holder fitted into a manufactured stainless steel adapter that was screwed into threaded holes in the z-stage. It protruded horizontally over the xy-stage where the sample was mounted on an insulating ceramic plate and clamped to the stage surface by means of Teflon clamps. Several holes spread over the xy-stage allowed samples of different size or even multiple samples to be mounted.

(5) Measurement setup

The setup for the electrical measurements performed is given in Figure 4-2. The emission current was measured indirectly by measuring the voltage drop across the resistor R1 by nano-voltmeter (Model 181, Keithley). The resistor R2 which was at least ten times higher in value serves as security resistor for the case of arc breakdown. The voltage supply (Model 248 High Voltage Supply, Keithley) allowed for dc voltages from 20 V to 5000 V.

4.3 Field Emission/Mapping Study

The field emission and field emission mapping from CVD diamond and carbon nanotube films are studied using the computer controlled system described in section 4.2.

4.3.1 CVD Diamond

Diamond films were deposited by a chemical vapor deposition system. A metal plate anode was used to measure the current density over the emitting surface and a pointed tungsten tip was used for mapping the emission current and emission site density.

4.3.1.1 Field emission

The reported emission current densities was typically below 1 A/cm^2, and was affected by diamond deposition parameters [66] and non-uniformity of emission sites [197]. While the presence of grain boundaries and/or defects in

diamond seemed to be necessary for appreciable field emission, it was not clear whether the non-uniformity of emission sites was related to variation in defect densities, diamond quality (sp^3/sp^2 ratio), electron affinity, grain size or grain-tip height. A study of the effect of film deposition parameters showed that low sp^3/sp^2 ratio, ion-implanted defects, patterned structures, or low-temperature diamond lead to higher current densities [29,30,39,45,198,199]. To generate more data for understanding the non-uniformity of emission sites, it is important to study the effect of doping, deposition temperature, post treatment and seeding method on the uniformity of emission sites for poly-diamond films.

- **Fabrication**

Employing different seeding densities, summarized in Table 3-1, undoped low-temperature polycrystalline diamond films were synthesized on p-type Si substrates by MPCVD using 1% CH_4 in H_2. The temperatures, monitored by an optical pyrometer, were kept at the 500, 550 and 600 C. Figure 4-3 shows SEM micrographs for DPR grown at 500, 550 and 600 C for 2 hours. Aluminum was thermally evaporated on the backside of Si wafer to provide an ohmic contact. Then, the samples were annealed at 450 C in nitrogen for 30 min using a rapid thermal processor.

- **Field emission study**

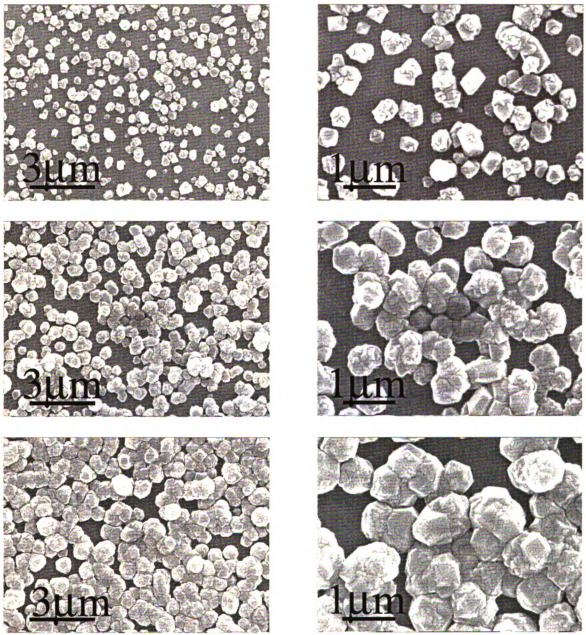

Figure 4-3: SEM micrographs of DPR deposited at (a) 500 C, (b) 550 C, and (c) 600 C for two hours.

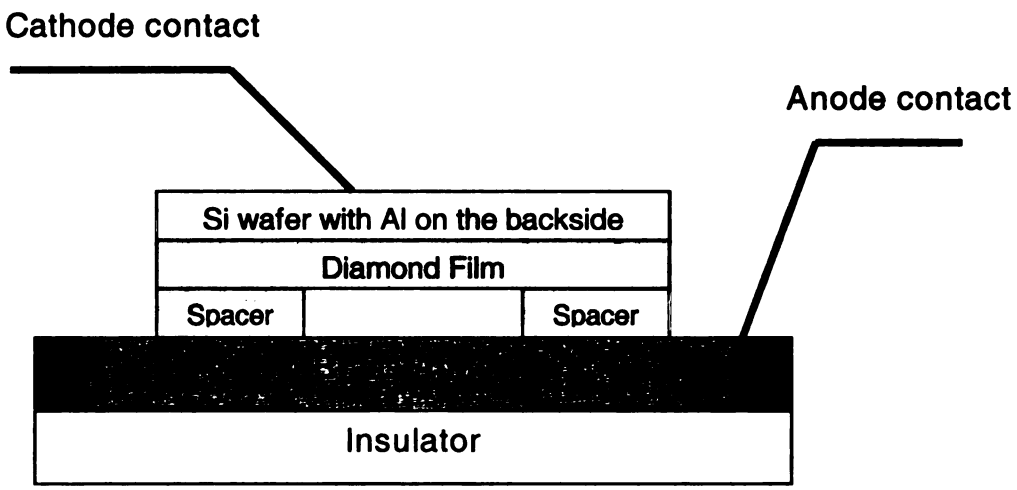

Figure 4-4: Setup for field emission measurement using flat anode.

Table 4-1: Grain densities and electric fields to achieve 1 $\mu A/cm^2$ for diamond grown at 600 C.

	Final Grain Density	Electric field (V/μm) for 1 $\mu A/cm^2$		
	(cm^{-2}) for 600C film	500C	550C	600C
DPR	2.5×10^8	22.5	17.5	15.81
DW-b*	4.8×10^9	16.25	16.13	15.69
DW-s*	8.5×10^9	15.63	14.63	14.06
N10	1.6×10^{10}	15	14.38	13.06

* b is brush seeded and s is spray seeded.

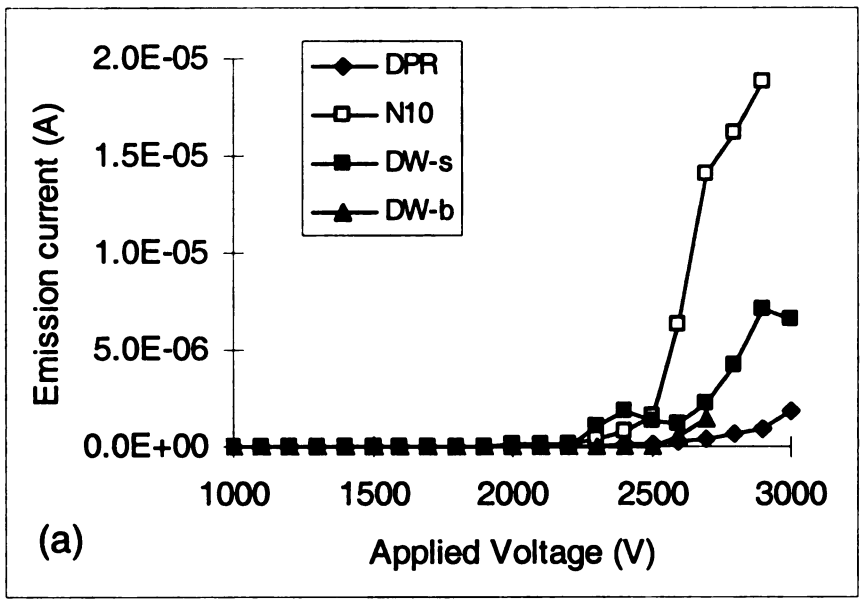

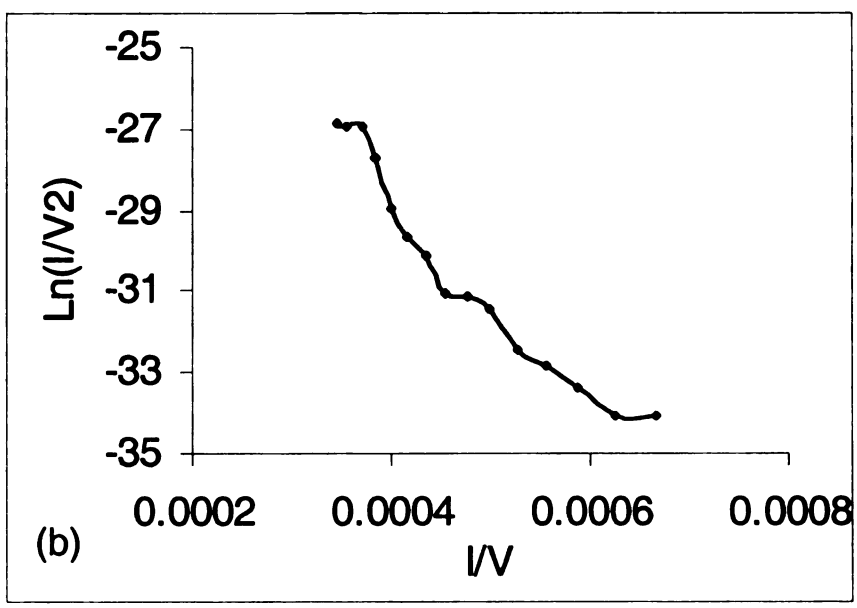

Figure 4-5: (a) I-V characteristics of diamond grown at 600 C with different seeding methods and (b) Fowler-Nordheim plot of N10 film grown at 600 C.

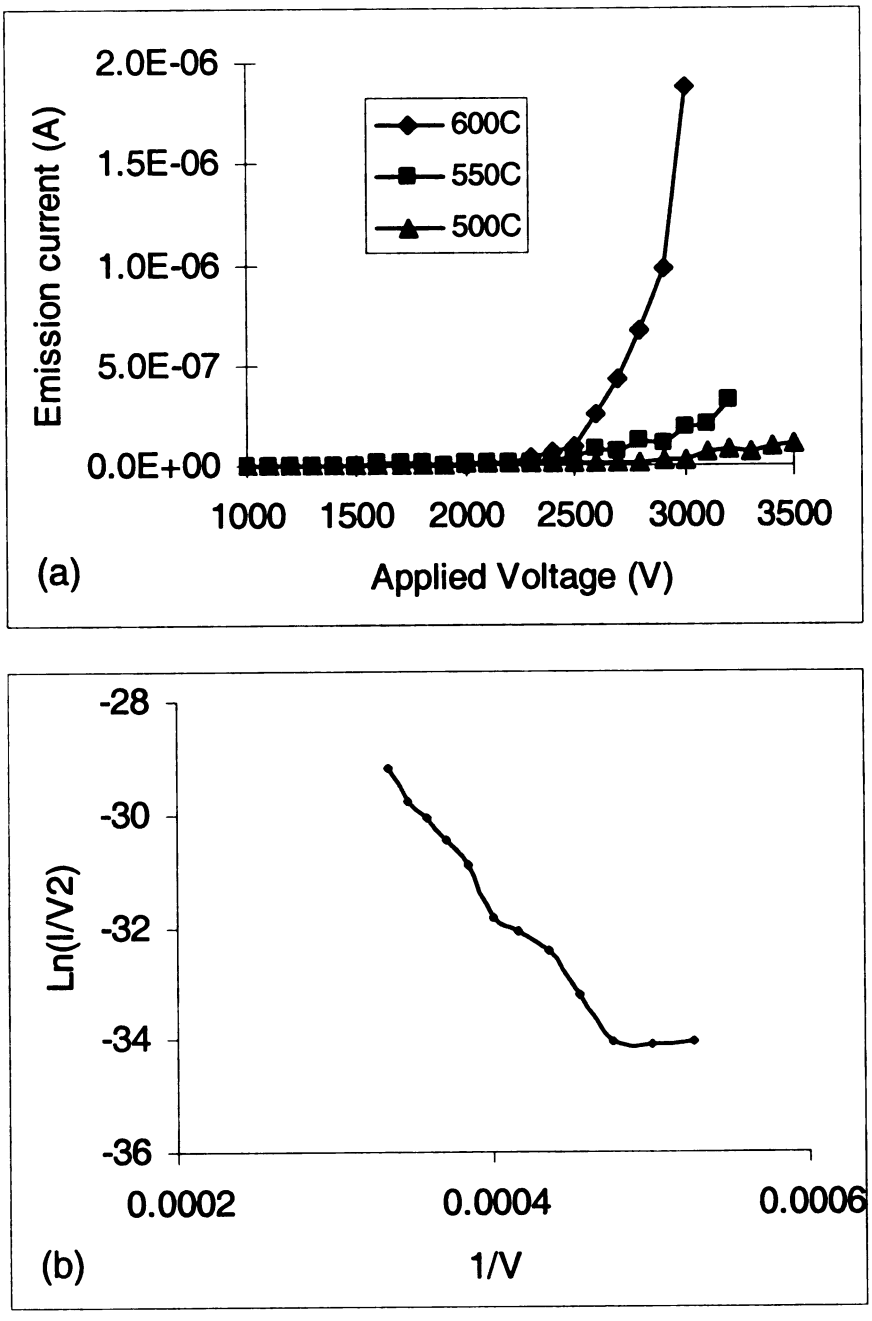

Figure 4-6: (a) I-V characteristics of DPR film grown at 500, 550, and 600 C and (b) Fowler-Nordheim plot of DPR film grown at 600 C.

For a systematic study of field emission from diamond, diamond films were deposited at 500, 550 and 600 C on Si wafers seeded under different conditions. The field emission current versus voltage (I-V) characteristics were measured using a brass plate anode keeping the spacing between anode to emitter at 160 μm by an insulating spacer as shown in Figure 4-4. Table 4-1 summarizes the grain density and turn-on electric field by the effects of seeding method. The grain size was the smallest for the N10 film and the largest for the DPR film. Thus, the N10 film had the highest grain densities which resulted in the lowest emission field. The emission varied inversely with grain size.

Figure 4-5 shows the emission current for the 600 C films. The high emission current for the smaller grain sizes was consistent with earlier results for doped diamond films prepared by hot filament CVD [66]. Table 4-2 summarizes the effect of deposition temperatures and Figure 4-6 illustrates the emission currents for DPR films grown at different temperatures. As all these films were not intentionally doped, the scattering in the data might be due to emission instabilities usually observed for high resistivity films. The results in the present study were opposed to the earlier study [199] that diamond films grown at lower temperature showed higher current densities. The difference between two works was that films in the earlier works were continuous, but they were not in this study. The surface grain densities were slightly decreasing but the grain boundary densities were increasing with increasing deposition temperature as shown in Figure 4-3. The graphitic inclusions or enhanced conductivity along grain boundaries had been suggested to aid the electron emission [6,62,201].

The Fowler-Nordheim plots of N10 and DPR films grown at 600 C were shown in Figures 4-5(b) and 4-6(b), respectively. The plots yielded approximately straight lines, which indicated the field emission behavior.

4.3.1.2 Field emission mapping

The electron emission from the surface of CVD polycrystalline diamond (poly-diamond) had been intensively studied for its application in field emission displays (FED) [6,201]. The experimentally observed electron emission from the surface of undoped or p-type polycrystalline diamond gave a great variance in spatial uniformity which arises from non-uniformity of emission sites. It was, however, not clear whether this non-uniformity was related to variation of electron affinity (dependent on hydrogen passivation of diamond surface), surface roughness (always present on unpolished polycrystalline diamond surface), surface defects (intrinsic or impurity related) or grain size. The deposition parameters, such as temperature, doping and gas mixture ratio, influenced the film morphology and defect contents. A clear correlation between emission properties and material properties could not be established at present.

- **Film fabrication**

The polycrystalline diamond films were deposited on p-type Si (100) substrate and free-standing diamond by MPCVD. Substrates were placed on a graphite substrate holder.

Table 4-2: Summary of deposition conditions and field emission current density.

Sample	Deposition Parameters				Emission current density ($\mu A/cm^2$)
	Process Gases (sccm)		Temperature (C)	Deposition Time (hours)	
	H_2, TMB + H_2	CH_4			
MS1	Flows for H_2 and 0.1% TMB* in H_2 are 199 and 1 sccm for all samples, respectively.	2	700	2	0.1
MS2		8	700	2	5912
MS3		14	700	2	2.4
MS5		8	600	5	1342
MS9		8	700	2	5850

* TMB: Trimethylboron

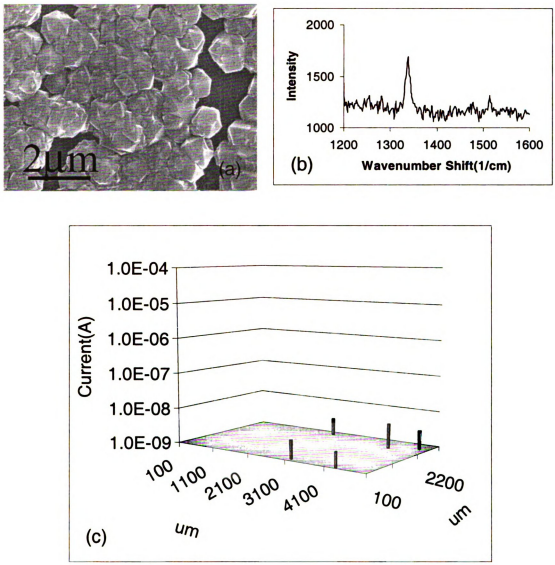

Figure 4-7: (a) SEM micrograph, (b) Raman spectra, and (c) field emission mapping for diamond film deposited at 700 C with 1% CH_4 in H_2.

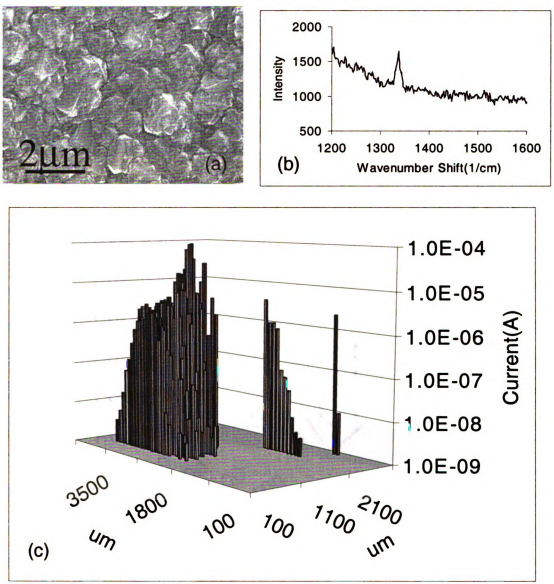

Figure 4-8: (a) SEM micrograph, (b) Raman spectra, and (c) field emission mapping for diamond film deposited at 700 C with 4% CH_4 in H_2.

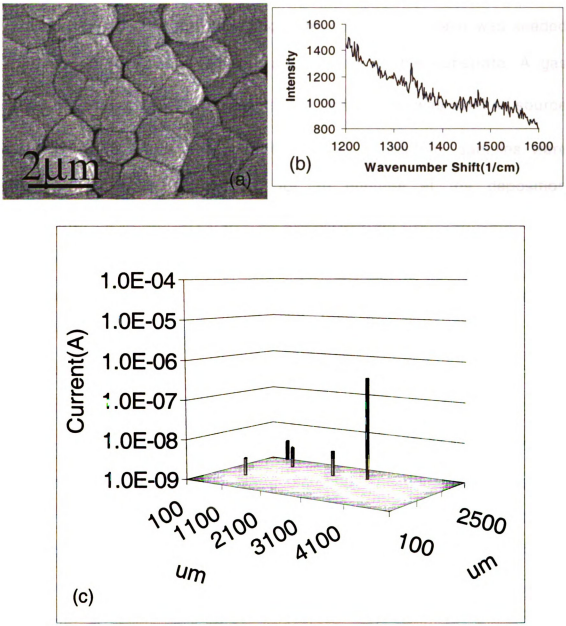

Figure 4-9: (a) SEM micrograph, (b) Raman spectra, and (c) field emission mapping for diamond film deposited at 700 C with 7% CH_4 in H_2.

Substrate temperature was measured by means of infrared pyrometer (Model OS3707, OMEGA), which recorded thermal radiation from the substrate. Before diamond deposition, the substrate surface was seeded with diamond particles. DPR was spin-coated on the substrate. A gas mixture consisting of 0.1% trimethylboron (TMB) in H_2 was used as source for in-situ of boron. At the end of diamond deposition, samples were treated in hydrogen atmosphere for 10 minutes at the deposition temperature.

For a systematic study of field emission from diamond, diamond films were deposited under different growth conditions. Table 4-2 summarizes the deposition conditions of the films. The first set of films was deposited at various methane concentrations, while keeping substrate temperature constant at 700C. The deposition temperature with same methane concentration was varied for the second set. The third set was deposited on polished free-standing diamond. The diamond film quality was monitored by scanning electron microscopy (SEM) and Raman spectroscopy.

- **Field emission study**

The film with 1% CH_4 in H_2, shown in Figure 4-7, displayed well faceted grains.

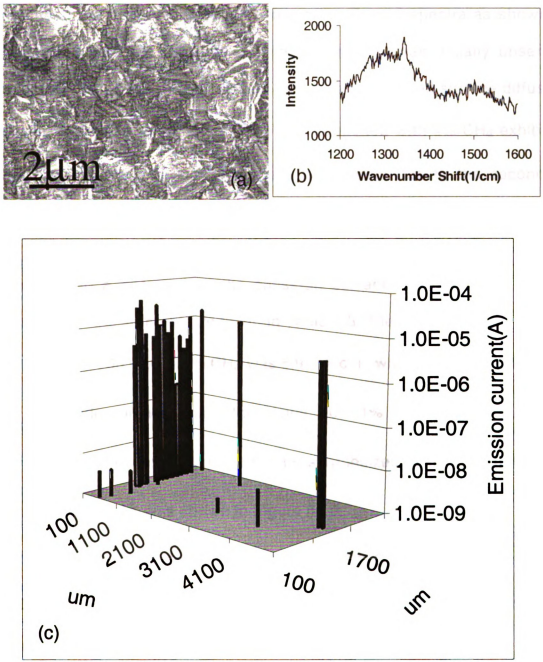

Figure 4-10: (a) SEM micrograph, (b) Raman spectra, and (c) field emission mapping for diamond film deposited at 600 C with 4% CH_4 in H_2.

The increase of CH_4 ratio exhibited degradation in grain facets and decreased the diamond peak intensity in the Raman spectra as shown in Figures 4-8 and 4-9. Cauliflower type morphology was usually observed under the conditions of high carbon saturation on limited surface diffusion causing extensive renucleation. The film deposited with 4% CH_4 exhibited high densities of microtips and grain boundaries due to the secondary nucleation, and showed more emission sites and high emission current. High quality (sample MS1) and cauliflower type (sample MS3) diamond films lead to a decrease of the emission current. The emission current densities for the samples are listed in Table 4-3. The current density for the film grown at 700 C with 4% CH_4 was 5.9 mA/cm^2 which was several orders of magnitude higher than the ones for 1% and 7% CH_4 films. Representative microstructures of films synthesized at 600C with 4% CH_4 concentration in H_2 was shown in Figure 4-10.

Although films deposited at 600 and 700 C with 4% CH_4, samples MS2 and MS5, showed comparable densities of microtwins and grain boundaries, Raman peak at 1332 cm^{-1} was sharper for the 700 C sample (MS2), indicating a higher quality, than that for the 600 C sample (MS5).

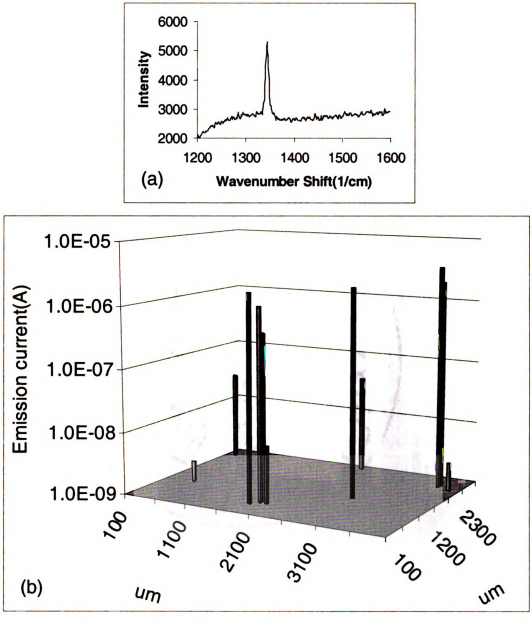

Figure 4-11: (a) Raman spectra and (b) field emission mapping for free-standing diamond film.

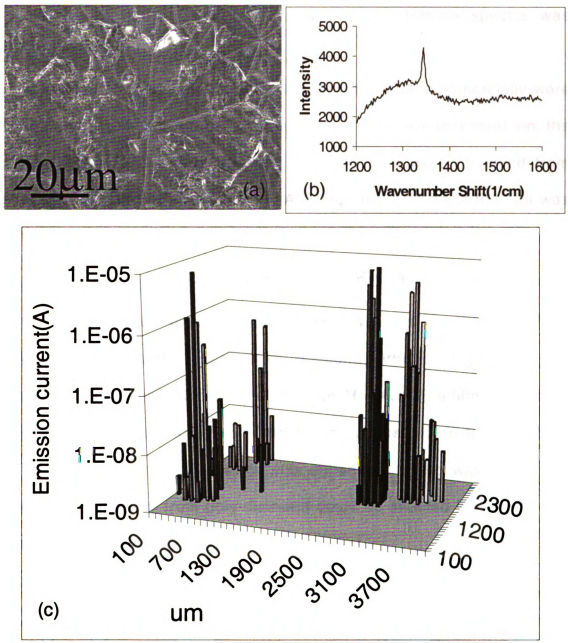

Figure 4-12: (a) SEM micrograph, (b) Raman spectra, and (c) field emission mapping for free-standing diamond film deposited at 700 C with 4% CH_4 in H_2.

The fact that the density of emission sites for the 700 C sample (MS2) was high seemed to support the model that high density of grain boundaries in the vicinity of high quality grains indicated by Raman spectra was important for field emission.

Polished free-standing diamond wafers available commercially were used to minimize the effect of a geometric field enhancement on the surface. Figure 4-11 shows that few emission sites were observed from polished free-standing diamond film. Although the surface of the film was relatively smooth, the grooves were found after doped diamond growth at 700 C with 4% CH_4 for two hours as shown in Figure 4-12. The doped film (MS9) showed higher emission site density than that for undoped free-standing diamond wafer. High quality diamond without a high density of grain boundaries showed low emission sites. However, if a film with a high density of grain boundaries and defects was deposited on top of a high quality diamond film, the emission was enhanced. It also was found that the electron emission from poly-diamond could be affected by defects and field enhancement at the tips [62].

4.3.2 Carbon Nanotubes

Carbon nanotubes were deposited on Si wafer coated with metal catalyst and pointed metal tips using chemical vapor deposition system. Field emission characteristics from carbon nanotubes were studied.

4.3.2.1 Carbon Nanotube Film

Carbon nanotubes have been attracting considerable attention because of their unique properties and potential for use as an electron field emitter. It is possible to achieve high emission current at moderate extraction voltages as a result of the high aspect ratio. The field emission properties of nanotubes with different orientations and after cleaning the residual particles were studied.

- **Fabrication**

Nanotubes were produced by MPCVD system using Fe or Ni as catalysts on Si wafer. The growth of nanotubes at a temperature of 650 C using a mixture of methane, hydrogen, and nitrogen lead to nanotubes with (i) different densities, (ii) horizontal or vertical growth and (iii) diameters in the range of 20-100 nm. Carbon nanotubes with density of 10^8–10^9 cm^{-2} were deposited uniformly on the substrate.

- **Field Emission**

The field emission mapping was performed on as-grown nanotube film. Figure 4-13 shows the non-uniformity of emission site and emission current which may be due to residual clusters sitting on the films. The nanotube film was treated in an ultrasonic bath.

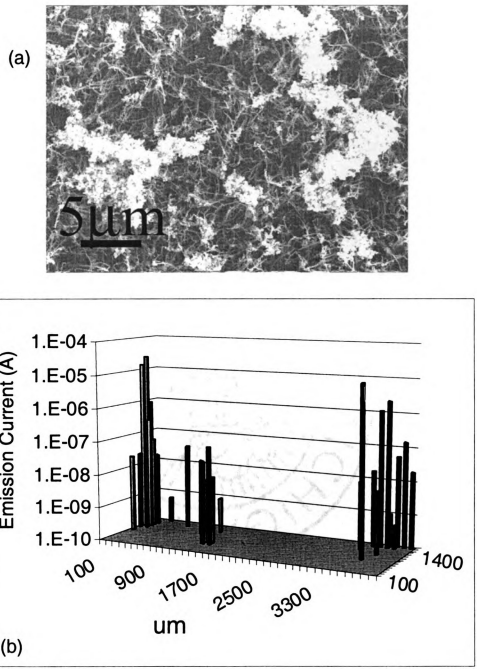

Figure 4-13: (a) SEM micrograph and (b) field emission mapping for carbon nanotube film grown at 650 C.

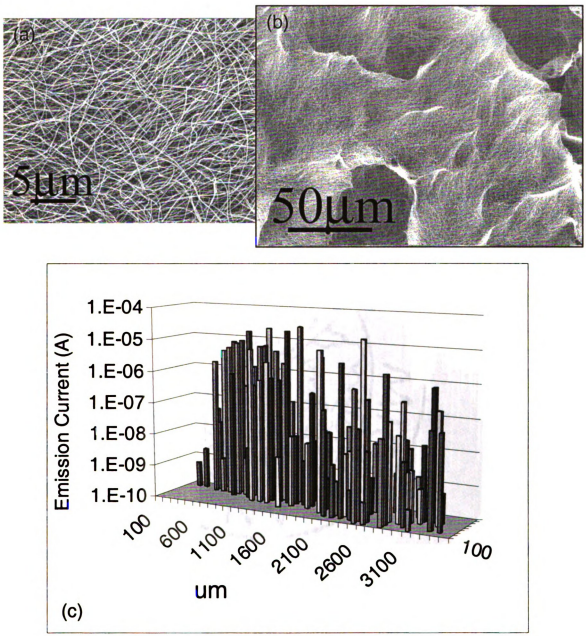

Figure 4-14: (a,b) SEM micrographs and (c) field emission mapping for carbon nanotube film of Figure 4-13 after cleaning.

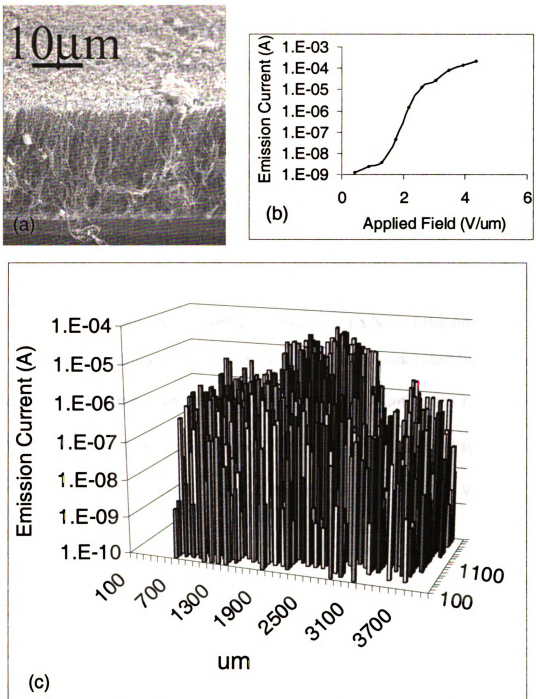

Figure 4-15: (a) SEM micrograph, (b) I-V characteristics, and (c) field emission mapping for highly oriented carbon nanotube film.

The emission mapping revealed that electron emission was improved by removing the clusters in an ultrasonic treatment as shown in Figure 4-14. Highly oriented nanotube film as seen in Figure 4-15 was studied for field emission properties.

The site density and uniformity of electron emission from nanotubes treated in ultrasonic was not as high as vertically oriented nanotubes. Nanotubes lost its orientation during the ultrasonic process as seen in Figure 4-14(b). This resulted in different local fields for each emitting sites. An emission site density was enhanced dramatically and the emission was uniform over the film surface. By using a flat anode separated by insulating spacers, current densities of 10 $\mu A/cm^2$ and 350 $\mu A/cm^2$ were measured at 2.3 V/μm and 4.3 V/μm, respectively. The reported turn-on field to produce a current density of 10 $\mu A/cm^2$ was in the range of 0.75 – 7.7 V/μm [2.142-2.145].

4.3.2.2 Nanotubes on a pointed tip

The use of carbon nanotubes as tips in scanning probe microscopies had been fascinating since high aspect ratio, mechanical robustness, and electrical conductivity provide great advantages over conventional silicon tips [203,204]. Most nanotube probe tips was made by mechanical attachment of nanotubes to silicon tips by the van der Waals force or an acrylic glue under optical or electron microscope [205,206,207].

To overcome the time consuming attaching process, the direct growth of nanotube on metal catalyzed Si tips by CVD was reported [208,209].

Besides their applications as tips in scanning probe microscopes, nanotubes were investigated as an electron point source. Recent studies show that nanotubes provided high currents at relatively low field with good stability for a long period of time [210,211,212]. The electronic structure, emission stability, and energy distribution of emitted electrons of a single nanotube mounted on metal tips was studied to better understand the field emission mechanism [134,137,213].

- **Fabrication**

Carbon nanotubes were synthesized on metal tips using CVD process. Four different sizes of 100 μm, 200 μm, 500 μm, and 1000 μm of Ni and Fe wires were used to form a pointed tip. Electrolytic etching was performed on these wires. The etching setup and etchant are described in Figure 4-16 and Table 4-3, respectively. Mixtures of water (30 ml), sulfuric acid (15 ml) and phosphoric acid (70 ml) for Ni wire, and sulfuric acid (60 ml) and water (40 ml) for Fe wire were used for electrolytic etching. The etching rate was enhanced by heating the solution to around 50 C. DC voltage (6V) was applied between the anode and the cathode. 500 μm wires were only used for CNT fabrication because of the long etching time for 1000 μm and handling for 100 and 200 μm wires. The tip radii of etched wires were in the range of 0.2 to 3 microns as seen in Figure 4-17.

Table 4-3: Etchant for electrolytic etching of nickel and iron wires.

Material	Etchant	Cathode
Nickel	30 ml DI water, 70 ml phosphoric acid, 15 ml sulfuric acid	Nickel
Iron	40 ml DI water, 60 ml sulfuric acid	Platinum

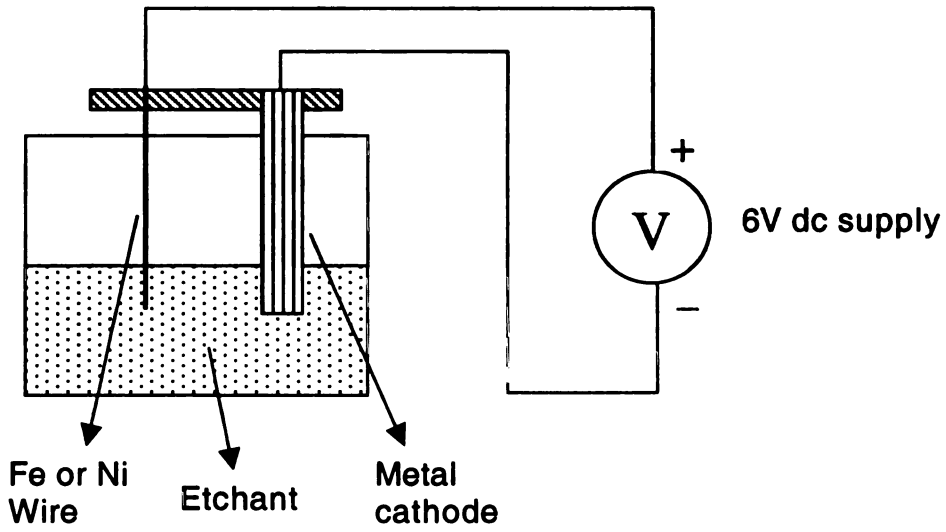

Figure 4-16: Diagram of electrolytic etching setup.

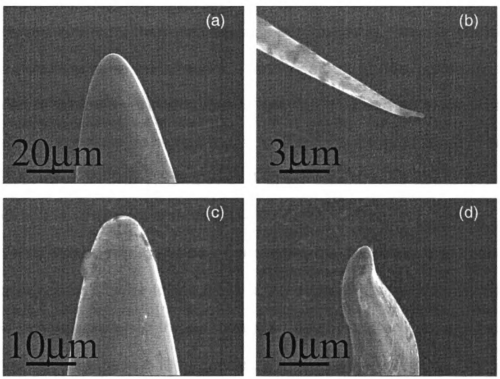

Figure 4-17: SEM micrographs of nickel wires after electrolytic etching. (a) 100 μm, (b) 200 μm, (c) 500 μm, and (d) 1000 μm.

MPCVD was employed to synthesize carbon nanotubes. The wires were placed in the holes of a ceramic disk in such a way that they were pointing towards the plasma as shown in Figure 4-18(a). The processing pressure and applied microwave power were 22 Torr and 1300 Watts, respectively. The wires were heated in the mixture of 90 sccm of hydrogen and 10 sccm of nitrogen for 5 min, then methane was introduced to grow nanotubes. The flow rate of methane was 6 sccm. The deposition of CNT lasted for 5 min. The dense plasma was locally formed around the sharp tip of the wire. This caused an increase of temperature at the tip area and resulted in less nanotube growth. The etching of CNT at the temperature above 800 C was observed in earlier experiments [214].

A different configuration of wire placement was used to reduce the direct exposure of wire to the plasma. An etched Fe or Ni wire was placed at the center parallel to the substrate holder. The side view and top view are depicted in Figure 4-18(b) and (c). A silicon wafer supported by 500 μm wires at the two sides was positioned onto the sample wire. The tip of the wire was located under the Si wafer. 1650 Watts of microwave power and 32 Torr of operation pressure were used to retain the temperature of the specimen at approximately 650 C. The flow rates of processing gases were kept the same as the one for the configuration in Figure 4-18(a). The density of nanotubes was improved with this configuration. The SEM micrographs of nanotubes grown on Fe and Ni tips were shown in Figures 4-19 and 4-20.

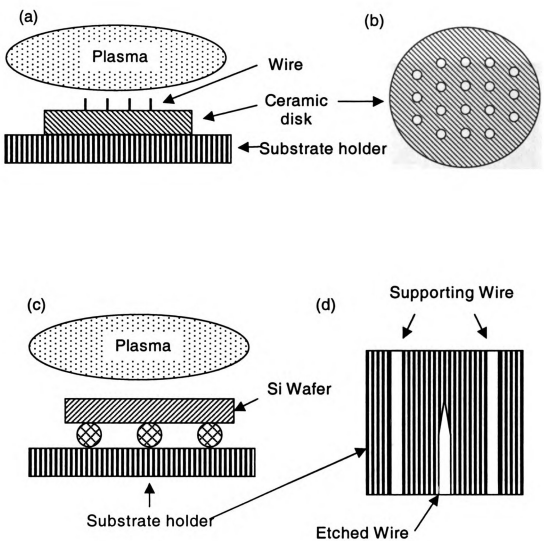

Figure 4-18: Diagrams of wire placement in MPCVD. (a) side view and (b) top view of configuration 1, (c) side view and (d) top view of configuration 2.

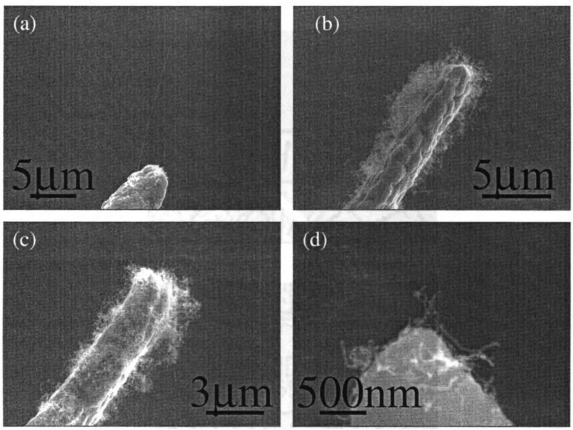

Figure 4-19: (a-d) SEM micrographs of nanotubes grown on Fe tips.

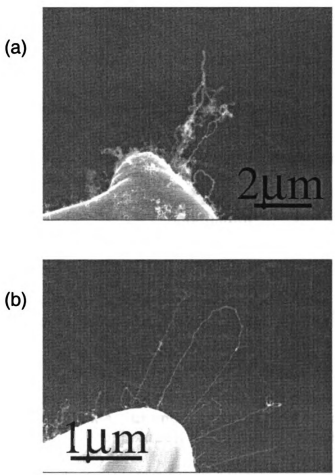

Figure 4-20: (a,b) SEM micrographs of nanotubes grown on Ni tips.

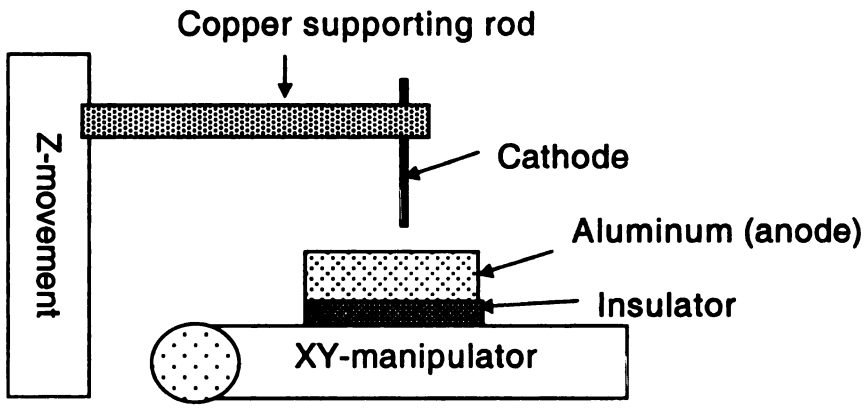

Figure 4-21: Measurement setup of field emission from carbon nanotubes on a pointed tip.

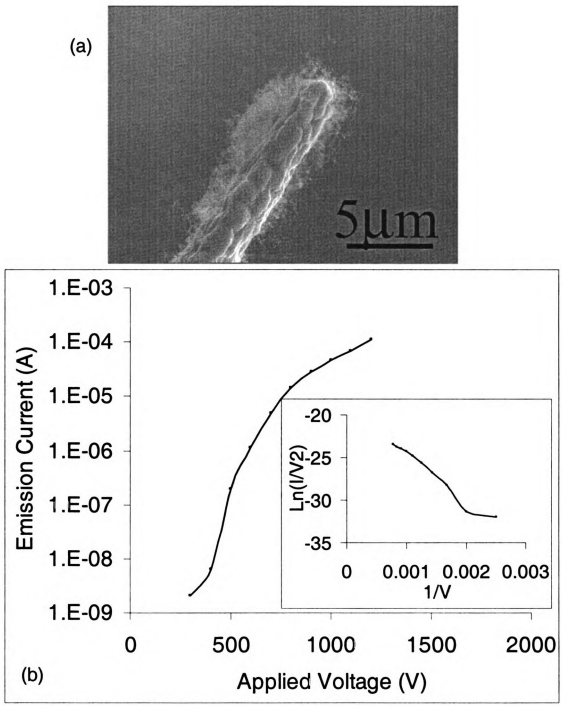

Figure 4-22: (a) SEM micrograph and (b) I-V characteristics of nanotubes grown on Fe tip. The inset is Fowler-Nordheim plot.

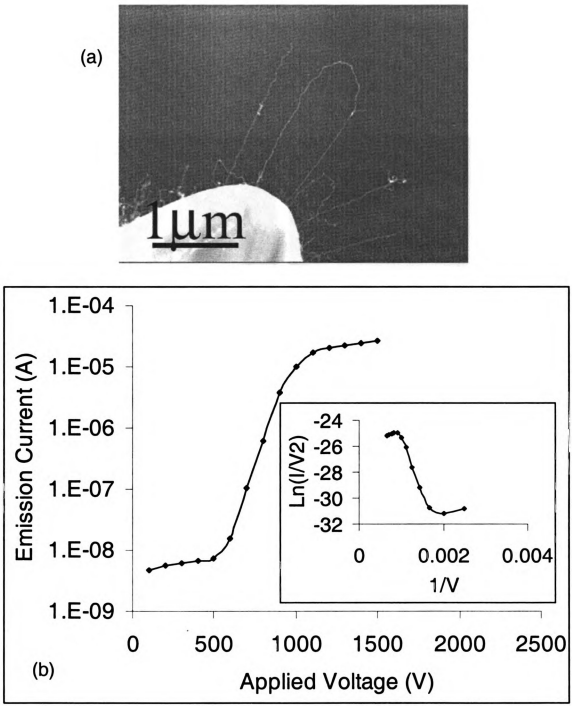

Figure 4-23: (a) SEM micrograph and (b) I-V characteristics of nanotubes grown on Ni tip. The inset is Fowler-Nordheim plot.

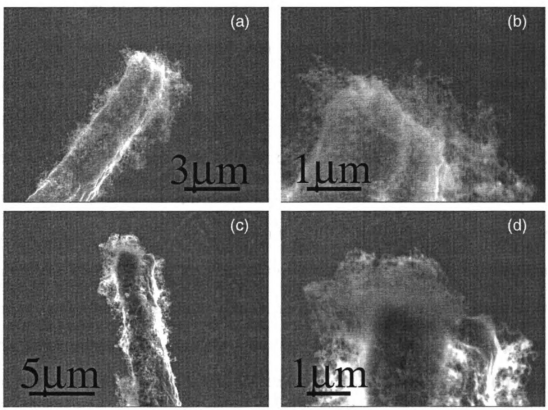

Figure 4-24: SEM images of nanotube on Fe tip: (a,b) as grown and (c,d) after field emission measurement at 6.7 μA.

The tip had various densities of tubes, ranging from a single tube to bundles of tubes. The tube diameter was approximately 40 nm, which indicated multi-walled carbon nanotubes, protruding 2 to 6 μm from the tip.

- **Field emission study**

The nanotube deposited wire was placed on the copper rod, as shown in Figure 4-21. An aluminum plate was used as an anode. The distance between anode and cathode could be adjusted by the vertical movement of the stage. The separation was measured approximately 100 - 500 μm. There was no appreciable emission current from a metal tip with typical fields of CNT measurement before nanotube deposition or a nanotube coated metal tip with reverse bias. The electron emission was mostly governed by a single nanotube that protruded slightly further than the other nanotubes. A single nanotube protruded and would experience an enhanced electric field. The I-V characteristics of nanotubes on Fe and Ni tips are displayed in Figure 4-22 and 4-23. The saturation current at high fields as shown in Figure 4-23(b) might be owing to the limited carrier concentration in a nonmetallic emitter [215]. It was reported that the electron emission from carbon nanotube was from the localized levels near the Fermi level, which suggested that the localized states at the nanotube tips were responsible for the emission [216]. The position of these levels with respect to the Fermi level depended on the tube chirality, diameter,

and the presence of defects [217]. According to Fowler-Nordheim theory, the current density is given by

$$J = 1.56\times10^{-6}\frac{F^2}{\phi}\exp(-6.83\times10^{7}\frac{\phi^{3/2}}{F}) \qquad (4.1)$$

F is the local field at the emitting surface in V/cm and ϕ is the work function of the emitter material in eV. The resulting electric field at the emitting surface can be defined as $F = \beta E = \beta V/d$, where V is the applied potential, d the distance between cathode and anode, β the field enhancement factor, and $E = V/d$ the macroscopic field. A Fowler-Nordheim plot should be linear if the current was governed by field emission. Work function was assumed to be that of graphite (~5 eV) and a field enhancement factor could be calculated from the Fowler-Nordheim curve. The calculated values of β were 39400 and 72970 cm^{-1} for nanotubes grown on Ni and Fe tips, respectively. The reported values of the field enhancement factors were in the range of 500 to 10000 cm^{-1} for an array of carbon nanotubes [125,9,139,218] and 30000 to 240000 for single nanotube [137,213]. Figure 4-26 shows that nanotubes on the tip were intact after the field emission measurement.

4.4 Summary

Field emission mapping revealed non-uniform distribution of emission sites and emission currents. Secondary nucleation on the diamond film surface

which resulted in an increase of density of grain boundaries played an important role in improving the electron emission. High quality diamond grains in the vicinity of high density of grain boundaries were crucial for high field emission current.

The clusters deposited during nanotube fabrication hindered field emission. The electron emission was dependent on the orientation of nanotube. The turn-on field to produce 10 $\mu A/cm^2$ from nanotube film was obtained at 2.3 V/μm. The field emission of nanotubes deposited on metal tips was studied. I-V characteristics followed the Fowler-Nordheim behavior, indicating that electron emission was due to the field emission process.

CHAPTER 5

FIELD EMISSION ELECTRO-LUMINESCENCE (FEEL) IN POLY-C

5.1 Introduction

Although electro-luminescence during field emission from carbon nanotubes was studied by other researchers, we reported field emission electro-luminescence (FEEL) on CVD diamond for the first time. I-V characteristics and spectral data of FEEL were studied. The qualitative models for FEEL and hysteresis behavior of emission current are proposed.

5.2 Field Emission Electro-luminescence Characterization Setup

The collected luminescence spectra through the optical fiber (1000 μm thick fused silica, Ocean Optics, Inc.) were analyzed by the spectrometer (PC2000 PC plug-in spectrometer, Ocean Optics, Inc.). The spectrometer was responsive from 350 to 1000 nm and couples via an SMA 905 connector to the optical fiber. The resolution was 5 nm full width at half maximum (FWHM). The slit with 50 μm wide and 1000 μm tall was installed. The schematic of the system is shown in Figure 5-1.

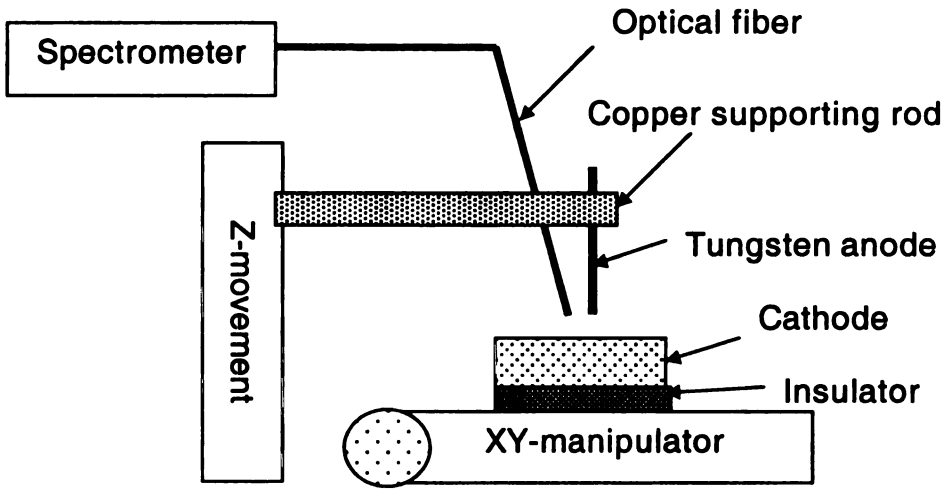

Figure 5-1: Schematic diagram of field emission electro-luminescence characterization setup.

The optical fiber was attached by the anode in the field emission characterization system which is described in Figure 4-1. The jacket and sheathing of the fiber inside the vacuum chamber were removed to minimize outgasing from them, and to attach easily to the probe anode. The fiber was positioned at 2 mm above the emitting surface.

5.3 Field Emission Electro-luminescence

Electro-luminescence during field emission from poly-diamond and carbon nanotubes was observed. The emission current characteristics and spectral data from FEEL are discussed.

5.3.1 CVD Diamond

The poly-diamond films grown by CVD methods contained structural defects and non-diamond phases, which gave rise to localized electronic states within the band gap [30,45,200]. There was experimental evidence that electron emission was related to defects in the films [29,39,198,199].

- **Film fabrication**

Diamond films were grown on p-type Si (100) and free-standing diamond substrates by MPCVD. Trimethylboron (diluted in H_2) was used as a doping source for boron. Diamond films were deposited at 700 C with 1.5 % CH_4 in H_2.

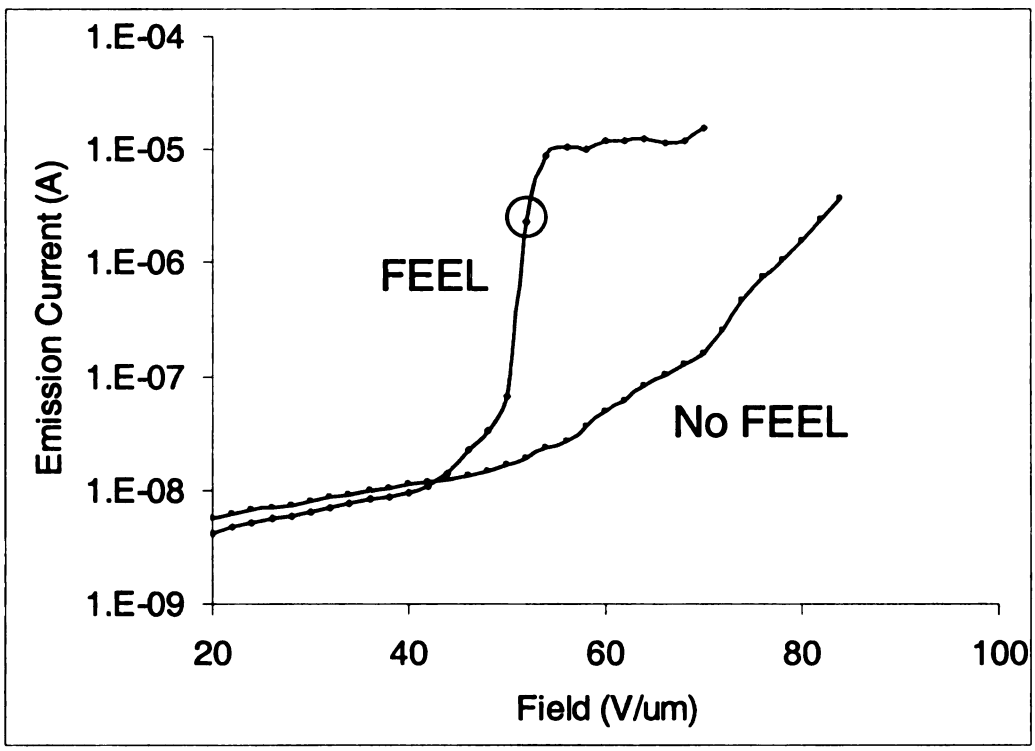

Figure 5-2: I-V characteristics with and without FEEL for undoped polycrystalline diamond film.

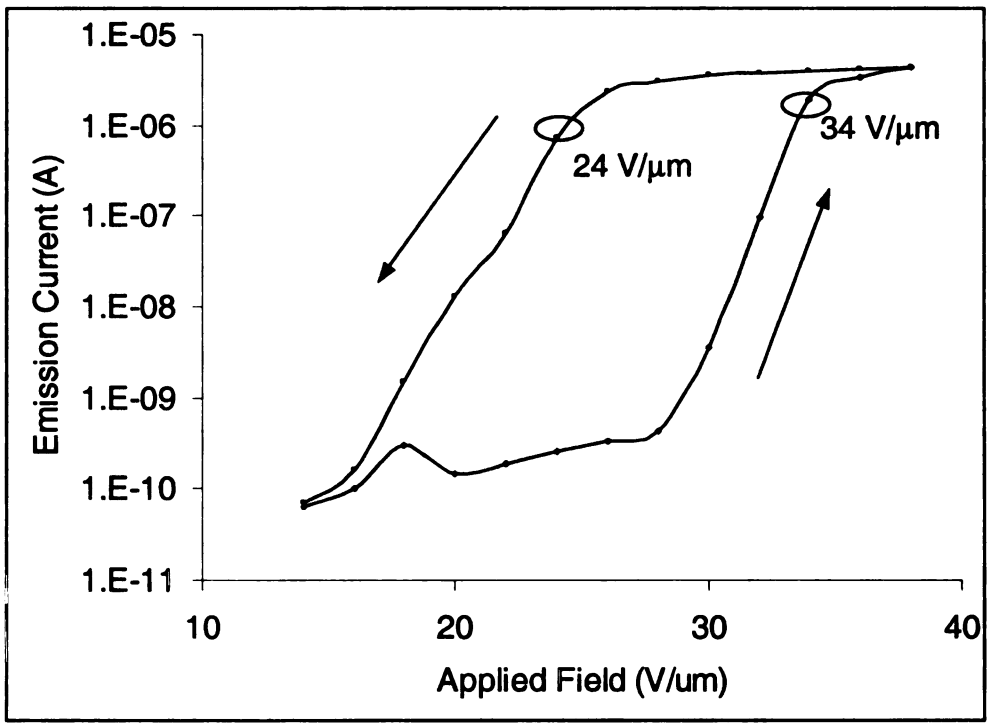

Figure 5-3: I-V characteristics with FEEL from B-doped free-standing diamond film.

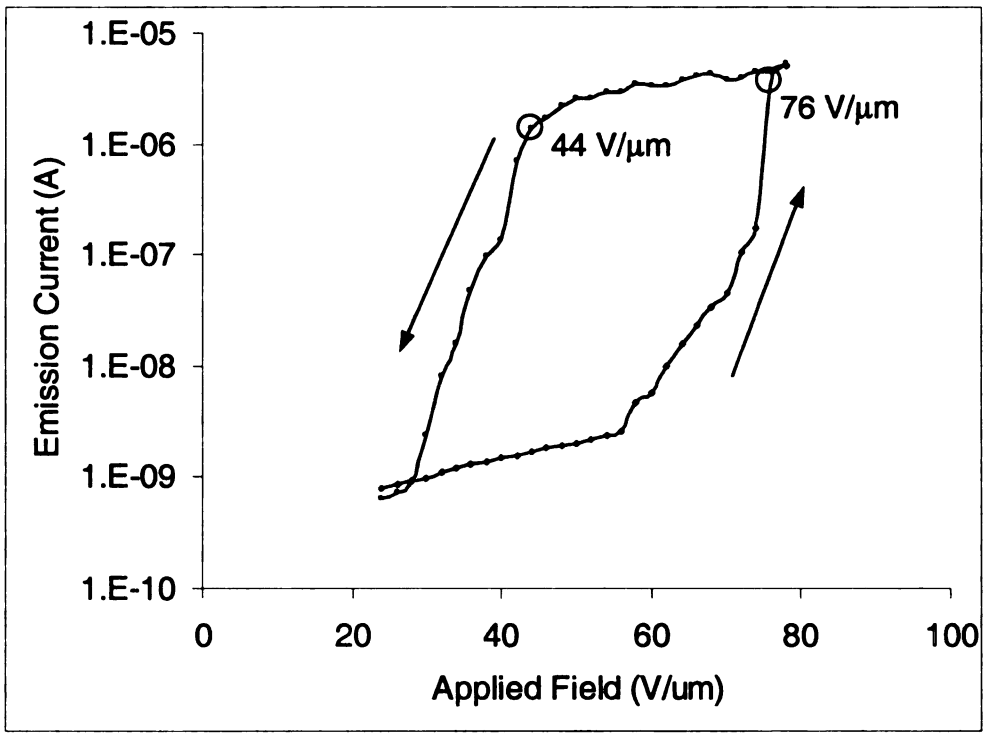

Figure 5-4: I-V characteristics with FEEL from undoped poly-diamond.

No precise values of resistivity of B-doped films were available since no electrical insulating layers were used between the films and p-type substrates. The resistivity for B-doped poly-diamond was roughly in the range of 0.05 – 0.5 Ωcm from the doping study in Section 3.3.3. The resistivity for the doped films on the free-standing diamond wafer was about 0.275 Ωcm. There was no intention of doping for undoped films. However, all films were terminated with hydrogen plasma for 5 min after growth.

- **Field emission electro-luminescence**

The field emission measurements were carried out at room temperature in a dark chamber to isolate it from surrounding light sources. Figure 5-2 shows two field emission curves measured at two different points on a poly-diamond film. FEEL was observed only for sites which showed a rapid increase of emission current. The emission current gradually saturated at high fields. The combination of space charge buildup and carrier saturation was taken into account for the current saturation. It was proposed that the vacuum space charge surrounding an emission site reduced the actual electric field at the emitter at high current [210]. Saturation of the emitter current due to limited carrier concentration could add to the space charge effect [219]. However, in this work, electrons contributed to field emission as well as electro-luminescence. The intensity of luminescence was almost a linear function of emission current, which

will be discussed later in this chapter. In other words, electrons taking part in electro-luminescence remained constant if the emission current saturated. The current at the low field regime of less than 40 V/μm was believed to be leakage currents. For sites that exhibited FEEL, an emission current of 1μA was required both for increasing and decreasing emission fields as seen in Figures 5-3 and 5-4, which were for B-doped large grain free-standing diamond and undoped poly-diamond, respectively. Once activated at the threshold, FEEL was sustained at electric fields much lower than the threshold field. The FEEL from B-doped free-standing diamond, initiated around 34 V/μm, continued at decreasing fields and stopped at 24 V/μm. FEEL, once triggered, was very stable and reproducible. The hysteresis behavior was repeatable. The field emission current behavior with FEEL from undoped poly-diamond was similar to the one from doped free-standing diamond except that luminescence was observed at the higher field than B-doped free-standing diamond. FEEL was observed at 76 V/μm with increasing field, and was terminated at 44 V/μm on decreasing field. Figure 5-5 shows luminescence spectra acquired at the emission current of 17.2 μA from B-doped free-standing diamond. The peak position of the main luminescence center occurred at 482 nm and a small peak appears at 638 nm. The main peak had a shoulder at 442 nm. A peak at 482 nm was observed from the electro-luminescence study of diamond film [90]. The peaks at 442 and 638 nm could be associated with growth induced dislocation and vacancy, respectively [86,87].

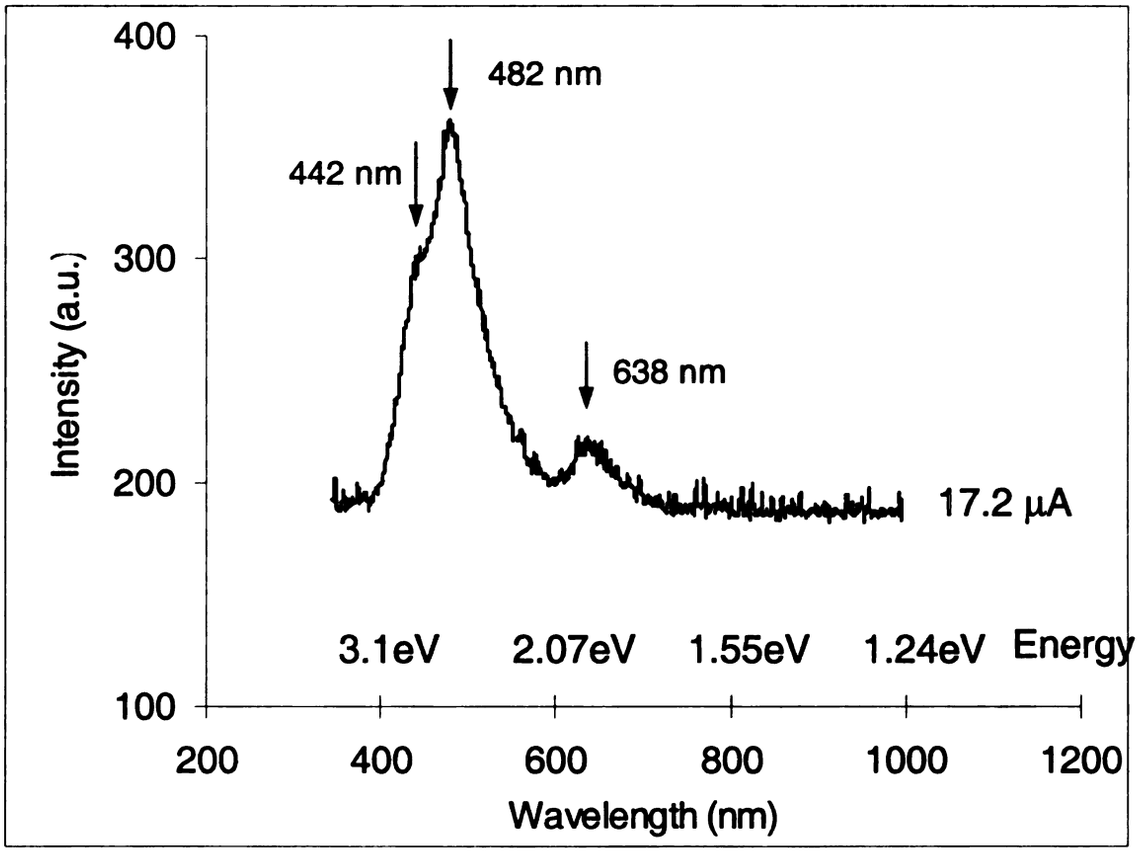

Figure 5-5: Luminescence spectra from B-doped free-standing diamond film.

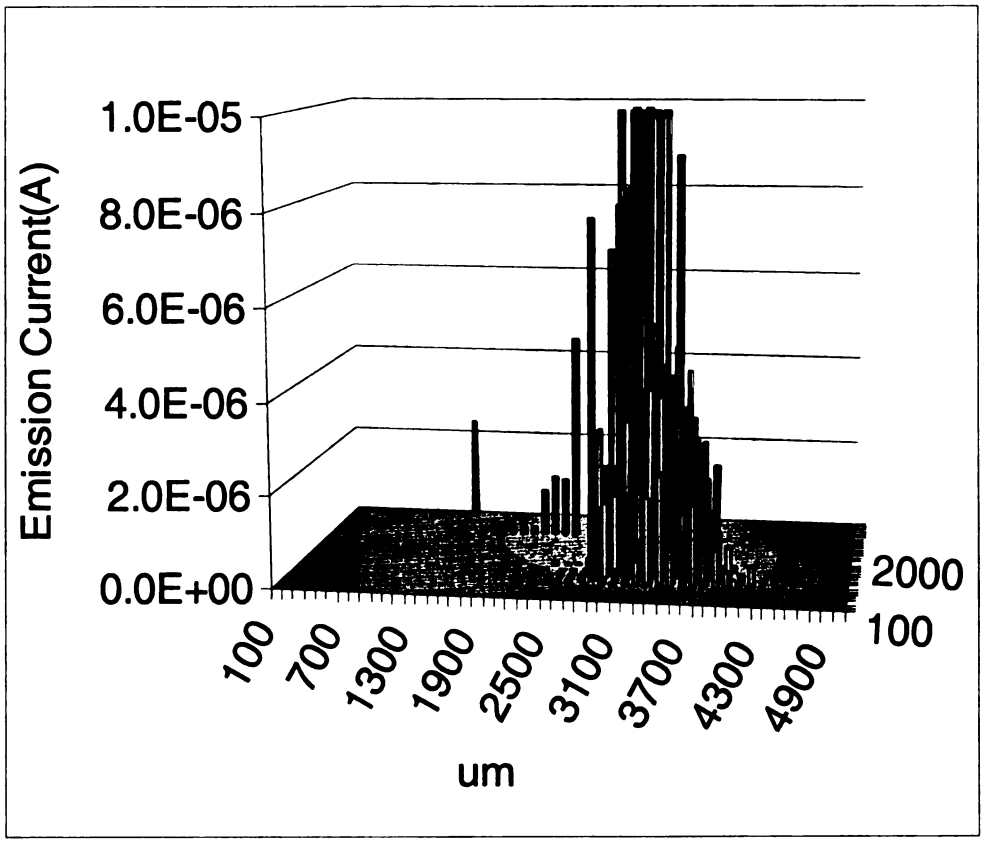

Figure 5-6: Field emission mapping for B-doped poly-diamond.

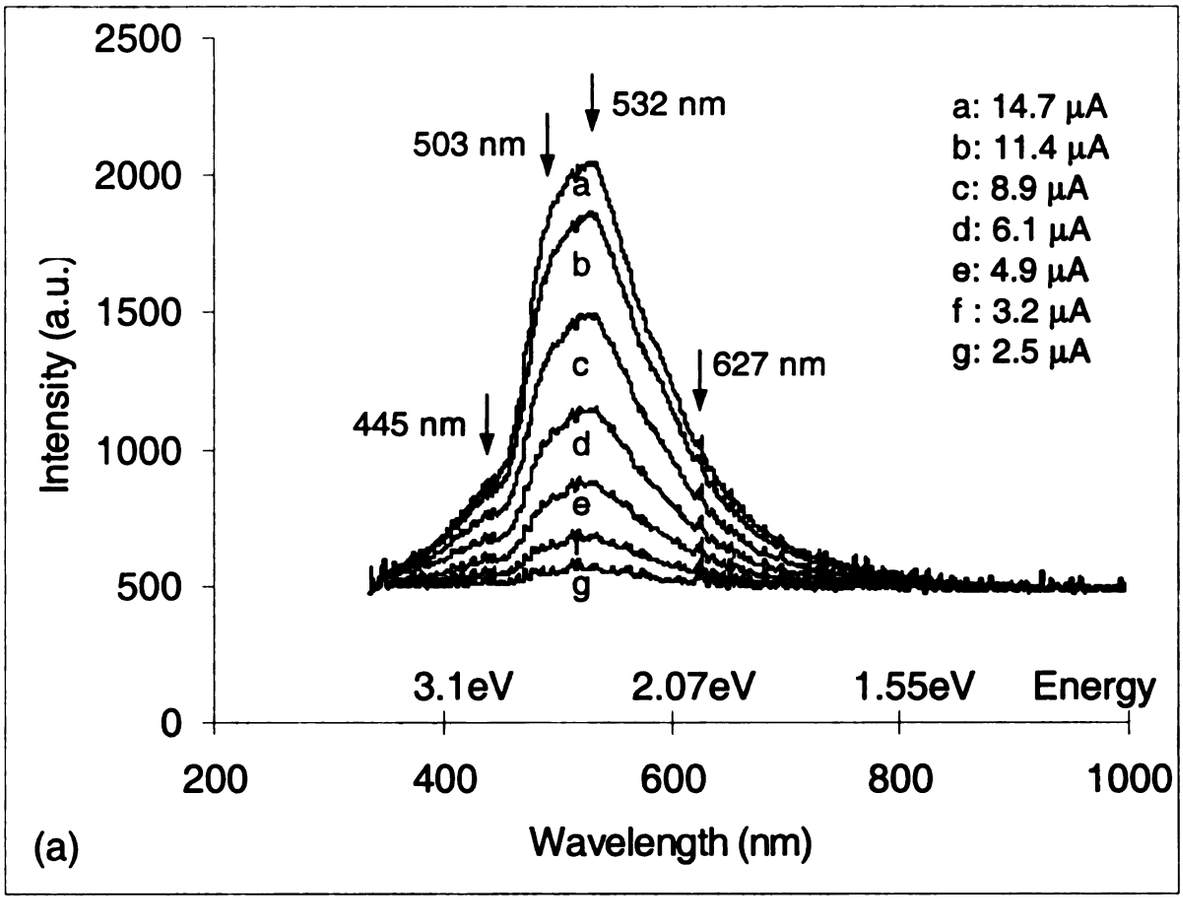

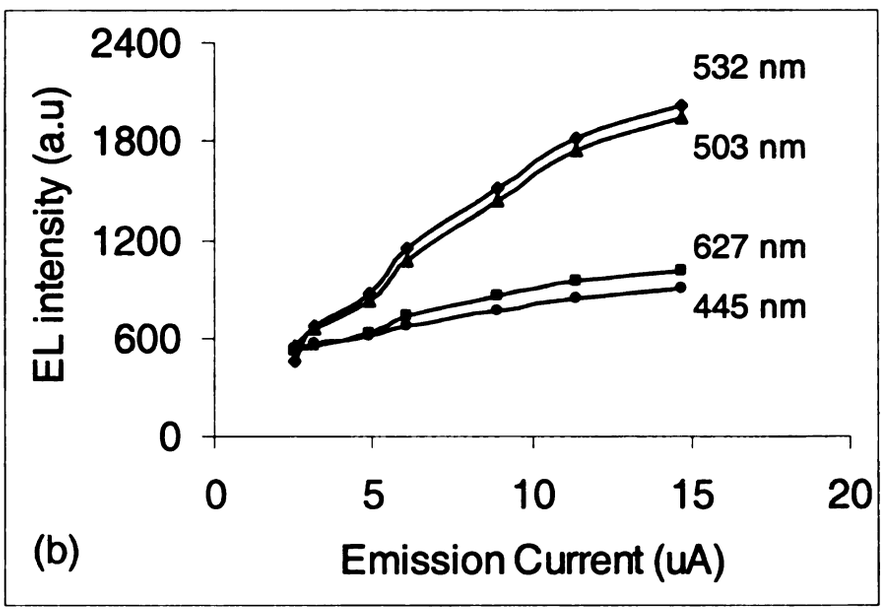

Figure 5-7: (a) Luminescence spectra with variation of emission current and (b) luminescence intensity as a function of emission current.

The field emission mapping of B-doped poly-diamond film is shown in Figure 5-6. The film was grown at the temperature of 700 C with the mixture of 4% of CH_4 in H_2 and trimethylboron for 2 hours. The field emission mapping revealed that there were a number of sites emitting currents above 1 μA. However, not every site exhibited FEEL. Some of the lower current sites showed a higher intensity of luminescence than the higher current sites. The intensity of luminescence at each emission site increased with the emission current as seen in Figure 5-7. The peak positions remained constant. The corresponding emission currents were in the range of 2.5 to 14.7 μA. The peak at 532 nm could be related to nitrogen [76]. Figure 5-7(b) shows that the luminescence intensity was nearly a linear function of emission current at different wavelengths.

5.3.2 Carbon Nanotubes

Highly oriented carbon nanotubes were deposited uniformly on the substrate. The diameter and density of the tubes were in the range of 20 – 100 nm and 10^8 - 10^9 cm^{-2}, respectively. The field emission mapping study on carbon nanotube films discussed in the section 4.3.2.1 showed relatively uniform emission current and high density of emission sites. The luminescence was observed during the field emission using a pointed tungsten anode at a distance of 50 μm. Three luminescence spectra from different emitting sites were shown in Figure 5-8.

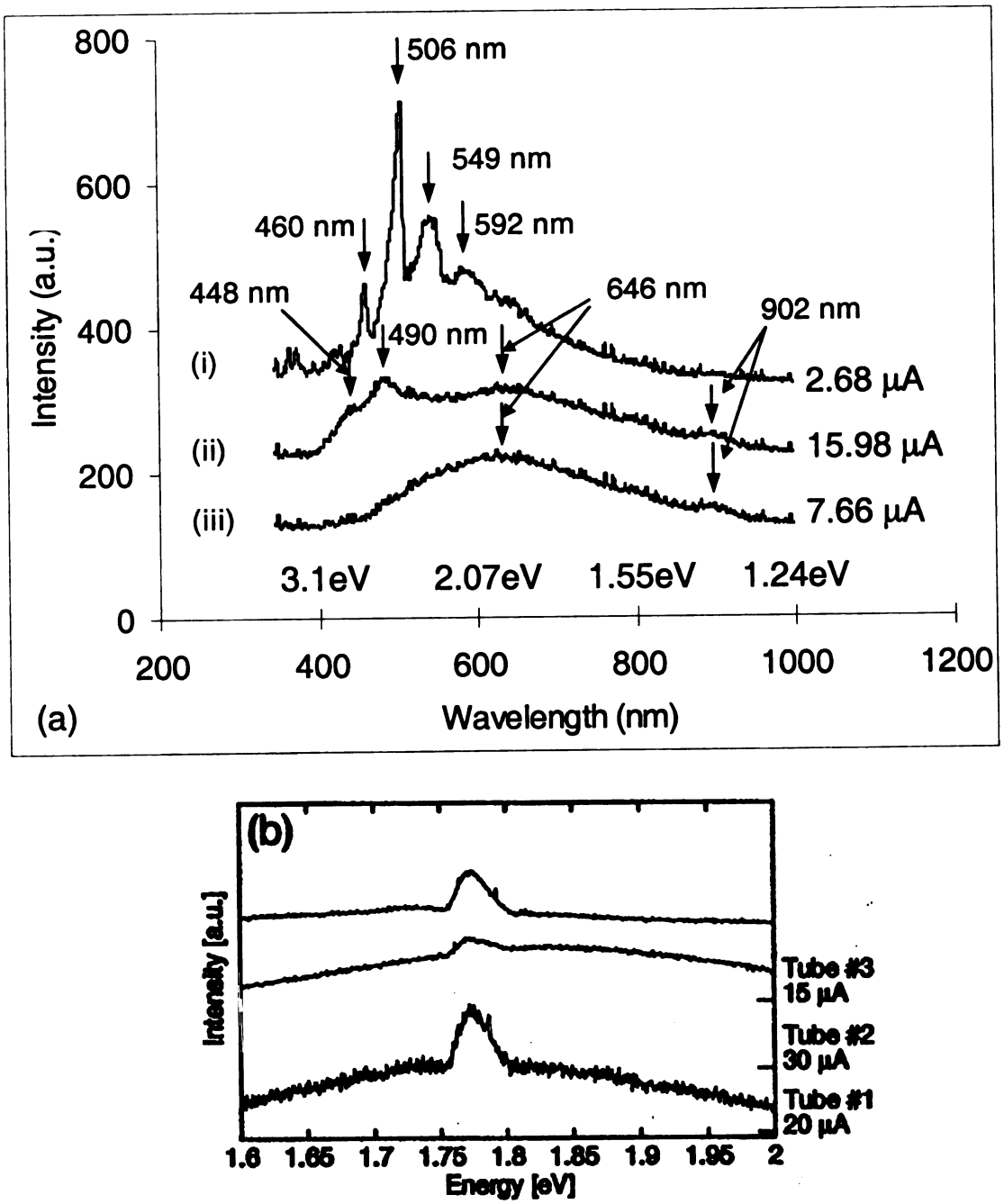

Figure 5-8: (a) Luminescence spectra of different FEEL sites from carbon nanotube film and (b) spectra from MWNTs in literature [2.148].

The sharp and broad peaks were superimposed on the spectra. The sharp peaks were indicative of discrete transitions between energy levels whereas broad bands indicative variable transition energies [73]. Most of the peaks were within visible range (430 – 690 nm) and their positions were different from the values reported in the literature [155]. Interestingly, the four peaks (460, 506, 549, 592 nm) in the spectra (i) in Figure 5-8 were roughly equally spaced. The spectra (iii) exhibited a broad peak at 646 nm. The second spectra consisted of two narrow peak at 448 and 490 nm positioned on top of the spectra (iii).

5.4 Qualitative Model

The qualitative models for FEEL and hysteresis loop of the emission current from poly-diamond films are described in detail.

5.4.1 Field Emission Electro-luminescence

A constant supply of electrons is needed to sustain electron emission. It was speculated that the grain boundary might form a conduction channel [220,221]. However, electron emission at low field was also achieved on mono-crystalline diamond. It was observed that impurity conduction existed in synthetic diamond [222]. However, the impurity level in B-doped diamond was less than 0.4 eV above the valence band and hence the conduction channel was several eVs below the emitting states.

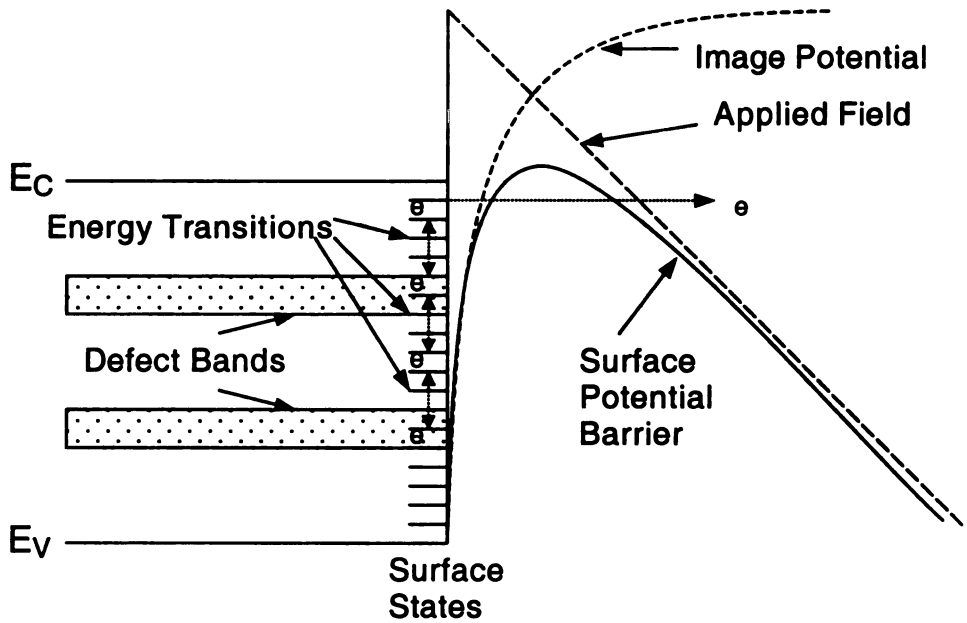

e: Electron

Figure 5-9: Quantitative model of field emission electro-luminescence from poly-diamond film.

Another possible way of transporting electrons to the emitting surface was through defect states. It was found that vacancy defects in diamond films were substantial [223,224]. Dangling bonds are expected to exist in the defects. If defect concentration is significant, the electron states in these defects can form a band or bands in the band gap. The formation of these defect bands may raise the Fermi level into the upper part of the band gap, and thus reduce the energy barrier that the electrons must tunnel through. If defect bands exist in the band gap, they transport electrons to the surface states. If the surface states are closely spaced, electrons can be hopping to the higher surface states closer to the conduction band and contribute to the field emission current. A fraction of electrons at the surface states drops to lower energy levels. The direct energy transitions between surface states are suggested to lead to FEEL. Figure 5-9 illustrates the schematic diagram of FEEL.

5.4.2 Hysteresis Loop

The field emission current with FEEL from poly-diamond film show hysteresis behavior with respect to the increasing and decreasing fields. Steady-state heat balance may account for hysteresis in the electro-luminescence of diamond films.

The rate R_+ of energy deposition and heating in a region of sample subjected to an external field E is given by

$$R_{+} = \eta I(T_{\text{int}})E \tag{5.1}$$

Where I is the emission current and η describes the efficiency of current conversion to heat. η is assumed to be temperature-independent in the relevant temperature range and is non-Ohmic in origin. At the same time, it is to be expected that η depends on defect density, since this alters resistivity by changing the electron scattering length. It is also assumed that current depends implicitly on a temperature T_{int} in the field region through a temperature-dependent resistivity.

The rate of cooling R_{-} is assumed to depend on the difference between the temperature T_{int} of atoms or molecules in the field region of the film and the temperature T_{ext} of the substrate. With the definition $\Delta T \equiv T_{int} - T_{ext}$, we write

$$R_{-} = c\Delta T \tag{5.2}$$

where c is assumed to be a constant in the relevant temperature range. The sample dependence implicit in cooling constant c can be parameterized by assuming proportionality to thermal conductivity κ, through a density- and geometry-dependent factor g ($c = g\kappa$).

Under steady-state conditions we can equate the heating and cooling rates from Equations (5.1) and (5.2) by setting

$$R_{+} = R_{-} \tag{5.3}$$

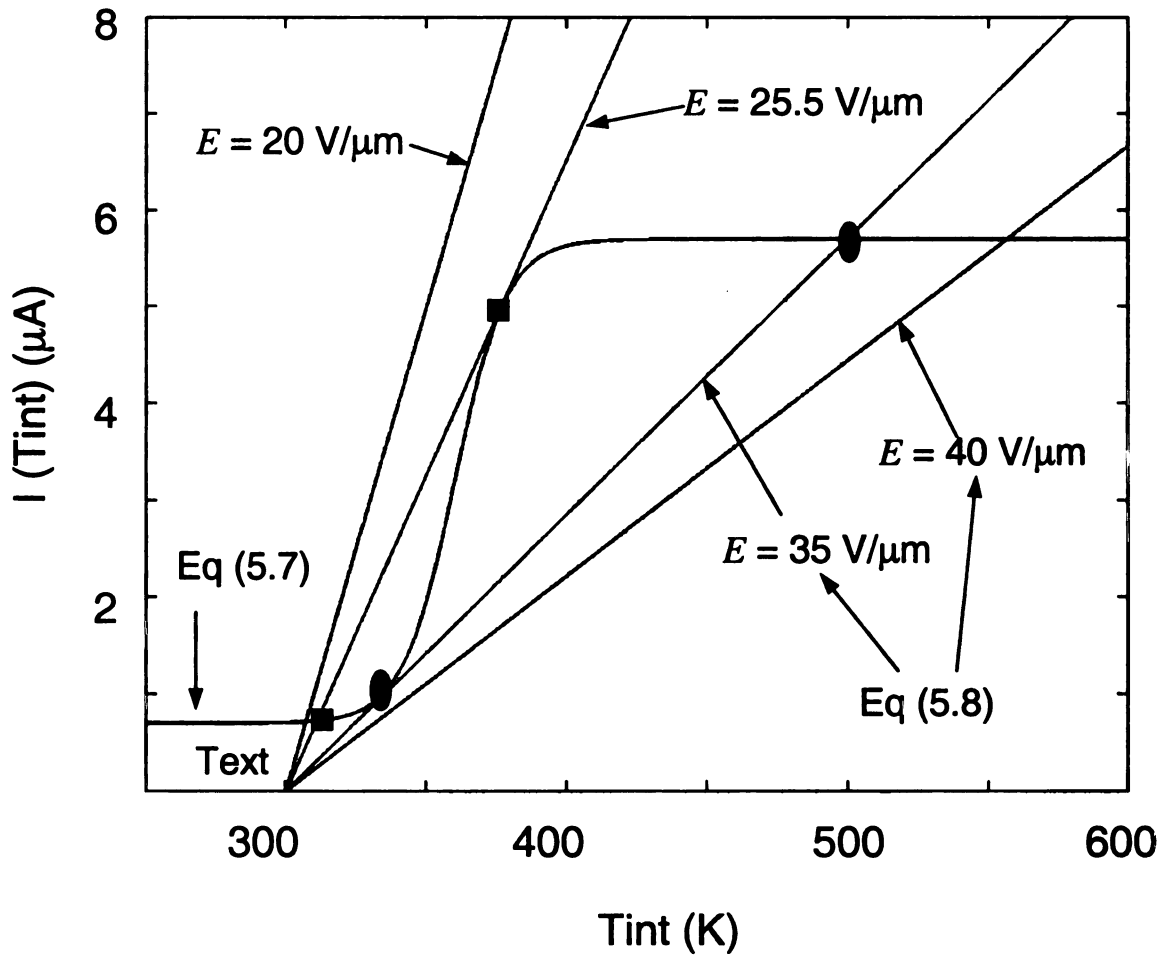

Figure 5-10: Dependence of current on temperature. The straight lines are plots of $\frac{\Delta T}{\xi E}$ for different values of E.

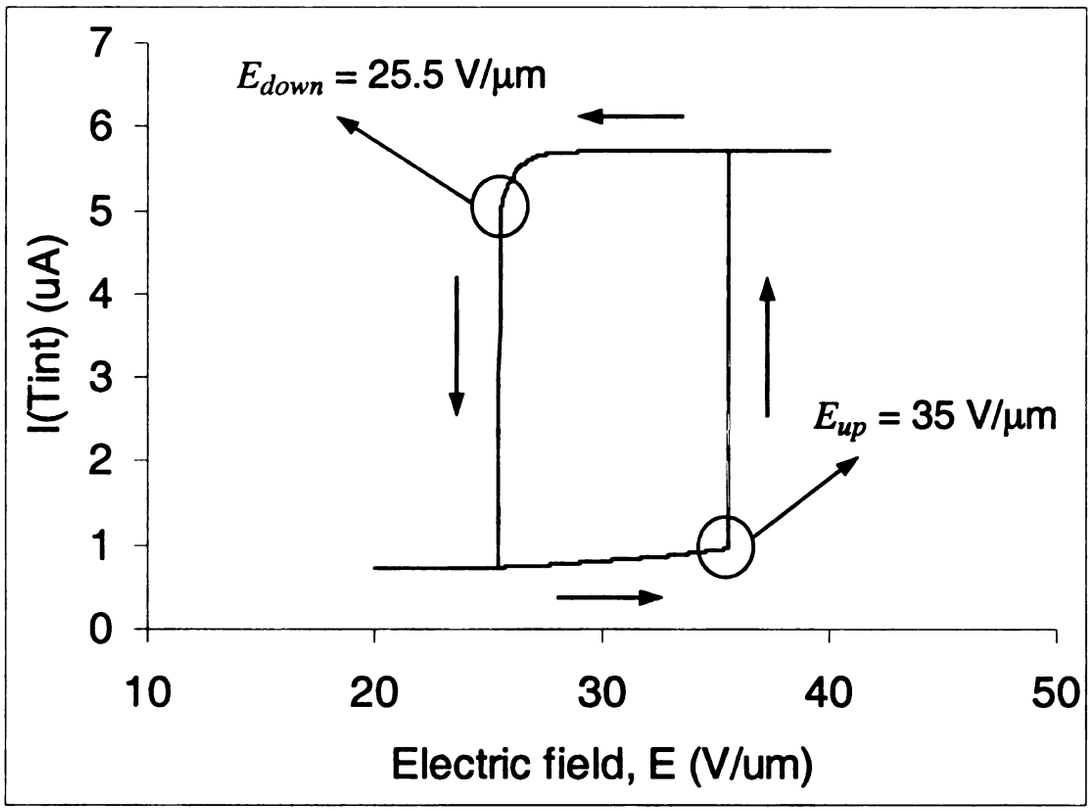

Figure 5-11: Replot of Figure 5-10; Dependence of current on electric field.

By substituting Equations (5.1) and (5.2) into Equation (5.3), it becomes

$$\eta I(T_{\text{int}})E = c\Delta T \tag{5.4}$$

$$I(T_{\text{int}}) = \frac{c}{\eta}\frac{\Delta T}{E} \tag{5.5}$$

By defining the ratio of heating and cooling constants to be $\xi \equiv \eta / c$, this yields an equation relating current to the applied field and temperature.

$$I(T_{\text{int}}) - \frac{\Delta T}{\xi E} = 0 \tag{5.6}$$

The current for a fixed field is determined at different equilibrium temperatures of the sample. This establishes the functional dependence of current on temperature, $I(T_{int})$. In a defective material, a temperature-dependent current might be expected on the basis of a thermally-mediated release of charge carriers. In order to illustrate the dependence of current on temperature, a hyperbolic tangent function is used.

$$I(T_{\text{int}}) = a * Tanh((T_{\text{int}} - b)/c) + d \tag{5.7}$$

a, b, c, and d are chosen to be 0.0000025, 360, 18.6, and 0.0000032, respectively, to make a fit into the experimental data. Figure 5-10 displays that solutions of Equation (5.6) can be obtained graphically as the intersections of the curve for Equation (5.7) with the plot

$$I(T_{\text{int}}) = \frac{1}{\xi E}(T_{\text{int}} - T_{ext}) \tag{5.8}$$

T_{ext} and ξ are assumed to be room temperature (300 K) and 0.1, respectively. The straight lines in Figure 5-10 are plotted by varying E values in Equation (5.8). The intersecting point is initially single valued as the straight line of Equation (5.8) crosses only once the curve for current (Equation 5.7). As E increases, there are two intersecting points at E = 25.5 V/μm. The current does not jump to the higher point since the local solution is available. Once the field exceeds the value E = 35 V/μm, the local solution is no longer available. The current is forced to jump to the non-local solution which has a much higher current level indicated by dots in Figure 5-10. There is a single solution for Equation 5.6 when the field is greater than 35 V/μm. When the field is decreasing, similar arguments can be applied. The current has a single value to begin with. The second solution is possible at E = 35 V/μm, but the current stays at the local solution. When the field crosses the value at E = 25.5 V/μm, the current drops to lower value. Presuming that the optical emission rates are proportional to the current, the luminescence intensity jumps to a higher value at the same time. According to this analysis, the switching fields are E_{up} = 35 V/μm and E_{down} = 25.5 V/μm. Figure 5-10 is replotted in Figure 5-11 in terms of the current values with respect to the increasing and decreasing electric fields. The current stays low level and jumps to high level at E = 35 V/μm when the field is increasing. At decreasing fields, the current stays high level until E = 25.5 V/μm. The current vs. electric field plot generates a hysteresis behavior. The FEEL turn-on and terminating fields from the theoretical values are in good

agreement with the experimental data of 34 and 24 V/μm for B-doped diamond film, as shown in Figure 5-3.

5.4 Summary

FEEL was observed from B-doped/undoped microcrystalline and large-grain freestanding poly-diamond and carbon nanotube films. The FEEL intensity increased with the emission current. However, there was no change in the peak position with the current. The analysis of luminescence spectra revealed that the luminescence centers were related to the defects. The quantitative models for FEEL and hysteresis behavior of emission current from poly-diamond were discussed.

CHAPTER 6

CONCLUSIONS AND FUTURE RESEARCH

6.1 Summary and Conclusions

- **Direct patterning of diamond**

A computer controlled patterning system was constructed. A 330 μm line and various patterns on 4 inch substrate were generated successfully by direct writing method. Diamond uniform seeding over a 2 inch substrate by spray nozzle was achieved. Diamond seeding patterns were produced successfully by a modified printer.

- **Fabrication of electron emitters**

The resistivity in diamond films was achieved in the range of 0.001 – 450 Ωcm using TMB as boron doping source. Procedures was developed for oriented nanotube growth and post-cleaning of nanotubes. Nanotubes were successfully grown on a pointed metal tip.

- **Spatial mapping of electron emission**

Field emission mapping revealed non-uniform distribution of emission sites and emission currents. High quality diamond grains in the

vicinity of high density of grain boundaries was crucial for high field emission current. The electron emission was dependent on the orientation of nanotube. Nanotubes on a tip was demonstrated as good electron source.

- **Field emission electro-luminescence**

FEEL was observed from poly-diamond for the first time. The FEEL intensity increased with the emission current. The analysis of luminescence spectra revealed that the luminescence centers were related to the defects. The quantitative models for FEEL and hysteresis behavior of emission current were proposed.

6.2 Future Research

Although in the present study, field emission electro-luminescence was observed and characterized for the first time, the following areas need to be addressed.

(i) The fabrication of practical cathodes remains unresolved. As field emission mapping study revealed, efforts should be made to improve the uniformity and site density of electron emission

(ii) Exact mechanisms of the electron transport through the film, as well as of electro-luminescence during field emission remain subjects of theoretical modeling and discussions.

Bibliography

[1] K. R. Shoulders, Adv. Computers 2, 135, 1961.

[2] C. A. Spindt, I. Brodie, L. Humphrey, and E. R. Westerberg, "Physical properties of thin film field emission cathodes with molybdenum cones", J. Appl. Phys., 47, 5248, 1976.

[3] T. Utsumi, "Vacuum microelectronics: what's new and exciting", IEEE Trans. Electron Dev., 38, 2276, 1991.

[4] H. H. Busta, "Review vacuum microelectronics - 1992", J. Micromech. Microeng., 2, 43, 1992.

[5] I. Brodie and P. R. Schwoebel, "Vacuum microelectronic devices", Proc. IEEE, 82, 1006, 1994.

[6] D. S. Hong and D. M. Aslam, "Poly-diamond gated field-emitter display cells", IEEE Trans. Electron Dev., 46, 787, 1999.

[7] K. Okano, K. Hoshina, M. Iida, S. Koizumi, and T. Inuzuka, "Fabrication of a diamond field emitter array", Appl. Phys. Lett., 64, 2742, 1994.

[8] J. M. Bonard, J. P. Salvetat, T. Stockli, L. Forro, and A. Chatelain, "Field emission from carbon nanotubes: perspectives for applications and clues to the emission mechanism", Appl. Phys. A 69, 245, 1999.

[9] X. Xu and G. R. Brandes, "A method for fabricating large-area, patterned, carbon nanotube field emitters", Appl. Phys. Lett., 74, 2549, 1999.

[10] U. Hoffmann, A. Weber, T. Lohken, C.-P. Klages, C. Spaeth, F. Richter, "Electron field emission of amorphous carbon films", Diamond Relat. Mater., 7, 682, 1998.

[11] Y. Sohda, D. M. Tanenbaum, S. W. Turner, and H. G. Craighead, "Fabrication of arrayed glassy carbon field emitters", J. Vac. Sci. Technol. B 15, 343, 1997.

[12] M. W. Geis, J. C. Twichell, and T. M. Lyszczarz, "Diamond emitters fabrication and theory", J. Vac. Sci. Technol. B 14, 2060, 1996.

[13] L. A. Chernozatonskii, Y. V. Gulyaev, Z. Y. Kosakovskaya, N. I. Sinitsyn, G. V. Torgashov, Y. F. Zakharchenko, E. A. Fedorov, and V. P. Valchuk, "Electron field-emission from nanofilament carbon-films", Chem. Phys. Lett., 233, 63, 1995.

[14] Yu. V. Gulyaev, L. A. Chernozatonskii, Z. Ja. Kosakovskaja, N. I. Sinitsyn, G. V. Torgashov, and Yu. F. Zakharchenko, "Field emitter arrays on nanotube carbon structure films", J. Vac. Sci. Technol. B, 13, 435, 1995.

[15] F. J. Himpsel, J. A. Knapp, J. A. Van Vechten, and D. E. Eastman, "Quantum photoyield of diamond (111) - a stable negative-affinity emitter", Phys. Rev. B 20, 624, 1979.

[16] J. B. Cui, R. Graupner, J. Ristein, and L. Ley, "Electron affinity and band bending of single crystal diamond (111) surface", Diamond Relat. Mater., 8, 748, 1999.

[17] S. Iijima and T. Ichihashi, "Single-shell carbon nanotubes of 1-nm diameter", Nature, 363, 603, 1993.

[18] T. W. Ebbesen and P. M. Ajayan, "Large-scale synthesis of carbon nanotubes", Nature, 358, 220, 1992.

[19] C. Journet and P. Bernier, "Production of carbon nanotubes", Appl. Phys. A, 67, 1, 1998.

[20] L. Nilsson, O. Groning, C. Emmenegger, O. Kuttel, E. Schaller, L. Schlapbach, H. Kind, J.-M. Bonard, and K. Kern, "Scanning field emission from patterned carbon nanotube films", Appl. Phys. Lett., 76, 2071, 2000.

[21] A. T. Collins, "Diamond, SiC, and Relatred Wide Bandgap Semiconductors", J. T. Glass, R. Messier, N. Fujimori Eds., Pittsburg, PA; Material's Research Society, 3, 1990.

[22] G. G. P. van Gorkan and A. M. E. Hoeberechts, "Performance of silicon cold cathodes", J. Vac. Sci. Technol. B 4, 108, 1986.

[23] P. K. Bachmann and R. Messier, "Emerging technology of diamond thin films", C&EN Special Report, 1989.

[24] P. K. Baumann and R. J. Nemanich, "Electron affinity and Schottky barrier height of metal-diamond (100), (111), and (110) interfaces", J. Appl. Phys., 83, 2072, 1998.

[25] Z. H Haung, P. H. Cuttler, N. M. Kiskovsky, and T. E. Sullivan, "Calculation of electron field emission from diamond surfaces", J. Vac. Sci. Technol. B 13, 526, 1995.

[26] E. I. Givargizov, V. V. Zhirnov, A. V. Kuznetsov, and P. S. Plekhanov, "Cold emission from the single-crystalline microparticle of diamond on a Si tip", J. Vac. Sci. Technol. B 14, 2030, 1996.

[27] P. Lerner, P. Cutler, and N. M. Miskovsky, "Theoretical analysis of field emission from a metal diamond cold cathode emitter", J. Vac. Sci. Technol. B 15, 337, 1997.

[28] Y. Gotoh, T. Kondo, M. Nagao, H. Tsuji, J. Ishikawa, K. Hayashi, and K. Kobashi, "Estimation of emission field and emission site of boron-doped diamond thin-film field emitters". J. Vac. Sci. Technol. B 18, 1018, 2000.

[29] M. W. Geis, N. N. Efremow, J. D. Woodhouse, M. D. Aleese, M. Marchywka, D. G. Socker, and J. F. Hochedez, "Diamond cold cathode", IEEE Elec. Dev. Lett., 12, 456, 1991.

[30] M. W. Geis, J. C. Twichell, C. O. Bozler, D. D. Rathman, N. N. Efremow, K. W. Krohn, M. A. Hollis, R. Uttaro, and T. M. Lyszczarz, Proc. 6th Int. Vacuum Microelectronics Conf., 160, 1993.

[31] C. Xie, C. N. Potter, R. L. Fink, C. Hilbert, A. Krishnan, D. Eichman, N. Kumar, H. K. Schimidt, M. H. Clark, A. Ross, B. Lin, L. Fredin, B. Baker, D. Patterson, and W. Brookover, "Use of diamond thin films for low cost field emission displays", Proc. 7th Int. Vacuum Microelectronics Conf., 229, 1994.

[32] K. Wu, E. G. Wang, J. Chen, and N. S. Xu, "Nitrogen-incorporated distorted nanocrystalline diamond films: Structure and field emission properties", J. Vac. Sci. Technol. B 17, 1059, 1999.

[33] M. V. Ugarov, V. P. Ageev, A. V. Karabutov, E. N. Loubnin, S. M. Pimenov, V. I. Konov, and A. Bensaoula, "Laser-induced modification of electron field emission from nanocrystalline diamond films", J. Appl. Phys., 85, 8436, 1999.

[34] S. Jou, H. J. Doerr, and R. D. Bunshah, "Electron emission characterization of diamond thin films grown from a solid carbon source", Thin Solid Films, 280, 256, 1996.

[35] V. V. Zhirnov, O. M. Kuttel, O. Groning, A. N. Alimova, P. Y. Detkov, P. I. Belobrov, E. Maillard-Schaller, and L. Schlapbach, "Characterization of field emission cathodes with different forms of diamond coatings", J. Vac. Sci. Technol. B 17, 666, 1999.

[36] A. N. Obraztsov, I. Yu. Pavlovsky, A. P. Volkov, E. V. Rakova, and S. P. Nagovitsyn, "Electron field emission from chemical vapor deposited diamond films", J. Electrochem. Soc., 145, 2572, 1998.

[37] B. Ju, Y. Lee, and M. Oh, "Fabrication and field emission properties of poly-diamond films", Microelectronics J., 29, 855, 1998.

[38] S. Kwon, Y. Shin, D. M. Aslam, and J. Lee, "Field emission properties of the polycrystalline diamond film prepared by microwave-assisted plasma chemical vapor deposition", J. Vac. Sci. Technol. B 16, 712, 1998.

[39] W. Zhu, G. P. Kochanski, S. Jin, L. Seibles, D. C. Jacobson, M. Mc Cormack, and A. E. White, "Electron field emission from ion-implanted diamond", Appl. Phys. Lett., 67, 1157, 1995.

[40] N. A. Fox, S. Mary, T. J. Davis, W. N. Wang, P. W. May, A. Bewick, J. W. Steeds, and J. E. Butler, "Field-emission studies of boron-doped CVD diamond films following surface treatments", Diamond Relat. Mater., 6, 1135, 1997.

[41] W. Zhu, G. P. Kochanski, S. Jin, and L. Seibles, "Electron field emission from chemical vapor deposited diamond", J. Vac. Sci. Technol. B 14, 2011, 1996.

[42] Y. Chen, C. Hu, and I. Lin, "Field emission characteristics of boron-doped diamond films prepared by MPE-CVD", Appl. Surf. Sci., 142, 516, 1999.

[43] K. Perng, K. Liu, and I. Lin, "Modification on the band structure and the related emission characteristics of defective diamond films doped with boron", Appl. Surf. Sci., 142, 494, 1999.

[44] C. Nutzenadel, O. M. Kuttel, O. Groning, and L. Schlapbach, "Electron field emission from diamond tips prepared by ion sputtering", Appl. Phys. Lett., 69, 2662, 1996.

[45] W. Zhu, G. P. Kochanski, S. Jin, and L. Seibles, "Defect-enhanced electron field emission from chemical vapor deposited diamond", J. Appl. Phys., 78, 2707, 1995.

[46] K. Okano, T. Yamada, A. Sawabe, S. Koizumi, R. Matsuda, C. Bandis, W. Chang, and B. B. Pate, "Characterization of electron emission from N-doped diamond using simultaneous field emission and photoemission technique", Appl. Surf. Sci., 146, 274, 1999.

[47] M. W. Geis, J. C. Twichell, N. N. Efremow, K. Krohn, and T. M. Lyszczarz, "Comparison of electric field emission from nitrogen-doped, type Ib diamond, and boron-doped diamond", Appl. Phys. Lett., 68, 2294, 1996.

[48] K. Okano, S. Koizumi, S. Ravi, P. Silva, and G. A. J. Amaratunga, "Low-threshold cold cathodes made of nitrogen-doped chemical-vapour-deposited diamond ", Nature, 389, 140, 1996.

[49] M. W. Geis, N. N. Efremow, K. E.. Krohn, J. C. Twichell, T. M. Lyszczarz, R. Kalish, J. A. Greer, and M.D. Tabat, "A new surface electron-emission mechanism in diamond cathodes", Nature, 393, 431, 1998.

[50] C. Kimura, K. Kuriyama, S. Koizumi, M. Kamo, and T. Sugino, "Field emission characteristics of phosphorus-doped hommoepitaxial diamond films", Appl. Surf. Sci., 146, 295, 1999.

[51] K. Park, S. Lee, K. Song, J. Park, K. Park, S. Han, S. Na, N. Lee, and K. Koh, "Field emission characteristics of defective diamond films", J. Vac. Sci. Technol. B 16, 724, 1998.

[52] W. Mueller, H. S. Dewan, H. Chen, G. T. Mearini, and I. L. Krainsky, "Field emission from gated diamond arrays", Appl. Surf. Sci., 146, 328, 1999.

[53] S. Albin, W. Fu, A. Carghese, A. C. Lavarias and G. R. Myneni, "Diamond coated silicon field emitter array", J. Vac. Sci. Technol. A 17, 2104, 1999.

[54] V. V. Zhirnov, E. I. Givargizov, A. V. Kandidov, B. V. Seleznev, and A. N. Alimova, "Emission characterization of diamond-coated Si field emission arrays". J. Vac. Sci. Technol. B 15, 446, 1997.

[55] S. Yang, and M. Yokoyama, "Electron emission behaviors of polycrystalline-diamond-coated silicon emitters", Jpn. J. Appl. Phys., 38, 209, 1999.

[56] J. Liu, V. V. Zhirnov, A. F. Myers, G. J. Wojak, W. B. Choi, J. J.Hren, S. D. Wolter, M. T. McClure, B. R. Stoner, and J. T. Glass, "Field emission characterization of diamond coated silicon field emitter", J. Vac. Sci. Technol. B 13, 422, 1995.

[57] J. Chen, Z. Deng, N. S. Xu, K. H. Wu, and E. G. Wang, "Observation of a non Fowler-Nordheim field-induced electron emission phenomenon from chemical vapor deposited diamond films", Appl. Phys. Lett., 75, 1323, 1999.

[58] M. Liao, Z. Zhang, W. Wang, and K. Liao, "Field-emission current from diamond film deposited on molybdenum", J. Appl. Phys., 84, 1081, 1998.

[59] A. Wisitsora-at, W. P. Kang, J. L. Davidson, W. Li, J. F. Xu, and D. V. Kerns, "Efficient electron emitter utilizing boron-doped diamond tips with sp^2 content", Appl. Surf. Sci., 146, 280, 1999.

[60] Z. Tolt, R. L. Fink, and Z. Yaniv, "Electron emission from patterned diamond flat cathodes", J. Vac. Sci. Technol. B 16, 1197, 1998.

[61] M. W. Geis, "Application of diamond films and related materials", Elsevier, Amsterdam, 309, 1991.

[62] C. Wang, A. Garcia, D. C. Ingram, M. Lake, and M. E. Kordesch," Cold field-emission from cvd diamond films observed in emission electron-microscopy". Electron Lett., 27, 1459, 1991.

[63] A. A. Blyablin, A. V. Kandidov, A. A. Pilevskii, A. T. Rakhimov, V. A. Samorodov, B. V. Seleznev, N. V. Suetin, and M. A. Timofeev, "Examination of electron field emission efficiency and homogeneity from CVD carbon-type films", Proc. 11th Int. Vacuum Microelectronics Conf., 234, 1998.

[64] W. Zhu, G. P. Kochanski, and S. Jin, "Low-field electron emission from undoped nanostructured diamond", Science, 282, 1471, 1998.

[65] Y. Show, F. Matsuoka, M. Hayashi, H. Ito, M. Iwase, and T. Izumi, "Influence of defects on electron emission from diamond films", J. Appl. Phys., 84, 6351, 1998.

[66] D. Hong and D. M. Aalam, "Technology and characterization of diamond field emitter structures", IEEE Trans. Electron Dev., 45, 977, 1998.

[67] F. Lacher, C. Wild, D. Behr, and P. Koidl, "Electron field emission from thin fine-grained CVD diamond films", Diamond Relat. Mater. 6, 1111, 1997.

[68] J. Luo, K. Liu, J. Lee, I. Lin and H. Cheng, "The influence of film-to-substarate characteristics on the electron field emission behavior of the diamond films", Diamond Relat. Mater., 7, 704, 1998.

[69] B. L. Weiss, A. Badzian L. Pilione, T. Badzian, and W. Drawl, "Fabrication of thin-film cold cathodes by a modified chemical vapor deposited diamond process", J. Vac. Sci. Technol. B 16, 681, 1998.

[70] I. T. Han, N. Lee, S. W. Lee, S. H. Kim and D. Jeon, "Field emission of nitrogen-doped diamond films", J. Vac. Sci. Technol. B 16, 2052, 1998.

[71] M. Q. Ding D. M. Gruen, A. R. Krauss, O. Auciello, T. D. Corrigan, and R. P. H Chang, "Studies of field emission from bias-grown diamond thin films", J. Vac. Sci. Technol. B 17, 705, 1999.

[72] A. R. Lang, A. P. W. Makepeace, and J. E. Butler, "Synchrotron X-ray microdiffraction measurements of lattice tilts within CVD diamond crystallites terminated by cathodoluminescent blue-cross-quartered cube facets", Diamond Relat. Mater., 7, 1698, 1998.

[73] G. Faggio, M. Marinelli, G. Messina, E. Milani, A. Paoletti, S. Santangelo, A. Tucciarone, and G. V. Rinati, "Comparative study of band-A cathodoluminescence and Raman spectroscopy in CVD diamond films", Diamond Relat. Mater., 8, 640, 1999.

[74] K. Hayashi, S. Yamanaka, H. Watanabe, T. Sekiguchi, H. Okushi, and K. Kajimura, "Investigation of the effect of hydrogen on electrical and optical properties in chemical vapor deposited on homoepitaxial diamond films", J. Appl. Phys., 81, 744, 1997.

[75] H. Kawarada, Y. Yokota, Y. Mori, K. Nishimura, and A. Hiraki, "Cathodoluminescence and electroluminescence of undoped and boron-doped diamond formed by plasma chemical vapor-deposition", J. Appl. Phys., 67, 983, 1990.

[76] L. H. Robins and D. R. Black, "Defect mapping of a synthetic diamond single-crystal by cathodoluminescence spectroscopy", J. Mater. Res., 9, 1298, 1994.

[77] A. T. Collins and S. C. Lawson, "Cathodoluminescence studies of isotope shifts associated with localized vibrational-modes in synthetic diamond". J. Phys. Condens. Mater., 1, 6929, 1989.

[78] A. T. Collins and G. S. Woods, "Isotope shifts of nitrogen-related localized mode vibrations in diamond". J. Phys. C 20, L797, 1987.

[79] A. T. Collins, G. Davies, H. Kanda, and G. S. Woods, "Spectroscopic studies of c-13 synthetic diamond". J. Phys. C 21, 1363, 1988.

[80] A. T. Collins, M. Kamo, and Y. Sato, "A spectroscopic study of optical-centers in diamond grown by microwave-assisted chemical vapor-deposition"J. Mater. Res., 5, 2507, 1990.

[81] T. Feng and B. D. Schwartz, "Characteristics and origin of the 1.681 ev luminescence center in chemical-vapor-deposited diamond films", J. Appl. Phys., 73, 1415, 1993.

[82] Y. D. Glinka, K. W. Lin, H. C. Chang, and S. H. Lin, "Multiphoton-excited luminescence from diamond nanoparticles", J. Phys. Chem. B 103, 4251, 1999.

[83] L. Diederich, O. M. Kuttel, P. Aebi, and L. Schlapbach, "Electron affinity and work function of differently oriented and doped diamond surfaces determined by photoelectron spectroscopy", Surf. Sci., 418, 219, 1998.

[84] V. S. Tatarinov, Y. S. Mukhachev, and W. A. Parifianovich, "High-temperature electroluminescence of diamond", Sov. Phys. Semicond., 13, 956, 1979.

[85] H. Sternschulte, J. Horseling, T. Albrecht, K. Thonke, and R. Sauer, "Characterization of doped and undoped CVD-diamond films by cathodoluminescence", Diamond Relat. Mater., 5, 585, 1996.

[86] X. Yang, A. V. Barnes, M. M. Albert, R. G. Albridge, J. T. McKinley, N. H. Tolk, and J. L. Davidson, "Cathodoluminescence and photoluminescence from chemical-vapor-deposited diamond", J. Appl. Phys., 77, 1758, 1995.

[87] J. W. Steeds, S. Charles, T. J. Davis, A. Gilmore, J. Hayes, D. Pickard, and J. E. Butler, "Creation and mobility of self-interstitials in diamond by use of a transmission electron microscope and their subsequent study by photoluminescence microscopy", Diamond Relat. Mater., 8, 94, 1999.

[88] K. Iakouvovskii, G. J. Adriaenssens, M. Nesladek, and L. M. Stals, "Photoluminescence excitation and quenching spectra in CVD diamond films", Diamond Relat. Mater., 8, 717, 1999.

[89] J. te Nijenhuis, S. M. Olsthoorn, W. J. P. van Enckevort, and L. J. Giling, "Red luminescence in phosphorous-doped chemically vapor deposited diamond", J. Appl. Phys., 82, 419, 1997.

[90] B. Zhang, S. Shen, J. Wang, J. He, H. R. Shanks, M. W. Leksono, and R. Girvan, "Blue-green electroluminescence of free-standing diamond thin films", Chin. Phys. Lett., 11, 235, 1994.

[91] C. Manfredotti, F. Wang, P. Polesello, E. Vittone, F. Fizzotti, and A. Scacco, "Blue-violet electroluminescence and photocurrent spectra from polycrystalline chemical vapor deposited diamond film", Appl. Phys. Lett., 67, 3376, 1995.

[92] R. Saito, G. Dresselhaus, and M. S. Dresselhaus, "Physical Properties of Carbon Nanotubes", Imperial College Press, London, 1998.

[93] M. S. Dresselhaus, G. Dresselhaus, and R. Saito, "Physics of carbon nanotubes", Carbon, 33, 883, 1995.

[94] R. Saito, M. Fujita, G. Dresselhaus, and M. S. Dresselhaus, "Electronic structure of chiral graphene tubules", Appl. Phys. Lett., 60, 2204, 1992.

[95] N. Hamada, S.–I. Sawada, and A. Oshiyama, "New one-dimensional conductors: graphitic microtubules", Phys. Rev. Lett., 68, 1579, 1992.

[96] L. Langer, V. Bayot, E. Grivei, J.-P. Issi, J. P. Heremans, C. H. Olk, L. Stockman, C. Van Haesendonck, and Y. Abruynseraede, "Quantum

transport in a multiwalled carbon nanotube", Phys. Rev. Lett., 76, 479, 1996.

[97] H. Dai, E. W. Wong, and C. M. Lieber, "Probing electrical transport in nanomaterials: conductivity of individual carbon nanotubes", Science, 272, 523, 1996.

[98] T. W. Ebbesen, H. J. Lezec, H. Hiura, J. W. Bennett, H. F. Ghaemi, and T. Thio, "Electrical conductivity of individual carbon nanotubes", Nature, 382, 54, 1996.

[99] J. E. Fischer, H. Dai, A. Thess, R. Lee, N. M. Hanjani, D. L. Dehaas, and R. E. Smalley, "Single-electron transport in ropes of carbon nanotubes", Science, 275, 1922, 1997.

[100] H. Hiura, T. W. Ebbesen, K. Tanigaki, and H. Takahashi, "Raman studies of carbon nanotubes", Chem. Phys. Lett., 202, 509, 1993.

[101] J. Kastner, T. Pichler, H. Kuzmany, S. Curran, W. Blau, D. N. Weldon, M. Delamesiere, S. Draper, and H. Zandbegen, "Resonance Raman and infrared spectroscopy of carbon nanotubes", Chem. Phys. Lett., 221, 53, 1994.

[102] W. S. Bacsa, D. Ugarte, A. Chatelain, and W. A. de Heer, "High-resolution electron microscopy and inelastic light scattering of purified multishelled carbon nanotubes", Phys. Rev. B 50, 15473, 1994.

[103] G. Overney, W. Zhong, and D. Tomanek, "Structural rigidity and low frequency vibrational modes of long carbon tubules", J. Phys. D 27, 93, 1993.

[104] J. P. Lu, "Elastic properties of carbon nanotubes and nanoropes", Phys. Rev. Lett., 79, 1297, 1997.

[105] E. Hernandez, C. Goeze, P. Bernier, and A. Rubio, "Elastic properties of C and $B_xC_yN_z$ composite nanotubes", Phys. Rev. Lett., 80, 4502, 1998.

[106] M. M. J. Treacy, T. W. Ebbesen, and J. M. Gibson, "Exceptionally high Young's modulus observed for individual carbon nanotubes", Nature, 381, 678, 1996.

[107] M. F. Yu, B. S. Files, S. Arepalli, and R. S. Ruoff, "Tensile loading of ropes of single wall carbon nanotubes and their mechanical properties", Phys. Rev. Lett., 84, 5552, 2000.

[108] S. S. Xie, W. Z. Li, Z. W. Pan, B. H. Chang, and L. F. Sun, "Mechanical and physical properties on carbon nanotube", J. Phys. Chem. Solids, 61, 1153, 2000.

[109] T. Hertel, R. Martel, and P. Avouris, "Manipulation of individual carbon nanotubes and their interaction with surfaces", J. Phys. Chem. B 102, 910, 1998.

[110] E. W. Wong, P. E. Sheehan, and C. M. Lieber, "Nanobeam mechanics: elasticity, strength, and toughness of nanorods and nanotubes", Science, 277, 1971, 1997.

[111] M. R. Falvo, G. J. Clary, R. M. Taylor, V. Chi, F. P. Brooks, S. Washburn, and R. Superfine, "Bending and buckling of carbon nanotubes under large strain", Nature, 389, 582, 1997.

[112] S. Iijima, "Helical microtubes of graphitic carbon", Nature, 354, 56, 1991.

[113] T. W. Ebbesen, H. Hiura, J. Fujita, Y. Ochiai, S. Matsui, and K. Tanigaki, "Patterns in the bulk growth of carbon nanotubes", Chem. Phys. Lett., 209, 83, 1993.

[114] G. H. Taylor, J. D. Fitzgerald, L. Pang, and M. A. Wilson, "Cathode deposits in fullerene formation – microstructural evidence for independent pathways of pyrolytic carbon and nanobody formation", J. Cryst. Growth, 135, 157, 1994.

[115] D. T. Colbert, J. Zhang, S. M. McClure, P. Nikolaev, Z. Chen, J. H. Hafner, D. W. Owens, P. G. Kotula, C. B. Carter, J. H. Weaver, A. G. Rinzler, and R. E. Smalley, "Growth and sintering of fullerene nanotubes", Science, 266, 1218.

[116] D. S. Bethune, C. H. Kiang, M. S. de Vries, G. Gorman, R. Savoy, J. Cazquez, and R. Beyers, "Cobalt-catalysed growth of carbon nanotubes with single-atomic-layer walls", Nature, 363, 605, 1993.

[117] W. K. Maser, J. M. Lambert, P. M. Ajayan, O. Stephan, and P. Bernier, "Role of Y-Ni-B mixtures in the formation of carbon nanotubes and encapsulation into carbon clusters", Synthetic Metals, 77, 1, 1996.

[118] L. A. Chernozatonskii, Z. Ja. Kosakovskaja, A. N. Kiselev, and N. A. Kiselev, "Carbon films of oriented multilayered nanotubes deposited on KBr and glass by electron beam evaporation", Chem. Phys. Lett., 228, 94, 1994.

[119] M. Ge and K. Sattler, "Vapor-condensation generation and STM analysis of fullerene tubes", Science, 260, 515, 1993.

[120] T. Guo, P. Nikolaev, A. G. Rinzler, D. Tomanek, D. T. Colbert, and R. E. Smalley, "Self assembly of tubular fullerenes", J. Phys. Chem., 99, 10694, 1995.

[121] M. Endo, K. Takeuchi, S. Igarashi, K. Kobori, M. Shiraishi, and H. W. Kroto, "The production and structure of pyrolytic carbon nanotubes", J. Phys. Chem. Solids, 54, 1841, 1993.

[122] W. K. Hsu, M. Terrones, J. P. Hare, H. Terrones, H. W. Kroto, and D. R. M. Walton, "Electrolytic formation of carbon nanostructures", Chem. Phys. Lett., 262, 161, 1996.

[123] P. Nikolaev, M. J. Bronikowski, K. Bradley, F. Rohmund, D. T. Colbert, K. A. Smith, and R. E. Smalley, "Gas-phase catalytic growth of single-walled carbon nanotubes from carbon monoxide", Chem. Phys. Lett., 313, 91, 1999.

[124] J. Kong, A. M. Cassell, and H. Dai, "Chemical vapor deposition of methane for single-walled carbon nanotubes", Chem. Phys. Lett., 292, 567, 1998.

[125] J. M. Bonard, J. P. Salvetat, T. Stockli, W. A. De Heer, L. Forro, and A. Chatelain, "Field emission from single-wall carbon nanotube films", Appl. Phys. Lett., 73, 918, 1998.

[126] C. Bower, O. Zhou, W. Zhu, A. G. Ramirez, G. P. Kochanski, and S. Jin, Mat. Res. Soc. Symp. Proc., 349, 319, 1994.

[127] W. Zhu, C. Bower, O. Zhou, G. Kochanski, and S. Jin, "Large current density from carbon nanotube field emitters", Appl. Phys. Lett., 75, 873, 1999.

[128] N. I. Sinitsyn, Y. V. Gulyaev, G. V. Torgashov, L. A. Chernozatonskii, Z. Kosakovskaya, Y. F. Zakharchenko, N. A. Kiselev, A. L. Musatov, A. I. Zhbanov, S. T. Mevlyut, and O. E. Glukhova, "Thin films consisting of carbon nanotubes as a new material for emission electronics", Appl. Surf. Sci., 111, 145, 1997.

[129] D. N. Davydov, P.A. Sattari, D. AlMawlawi, A. Osika, L. Haslett, and M. Moskovits, "Field emitters based on porous aluminum oxide templates", J. Appl. Phys., 86, 3983, 1999.

[130] W. A. De Heer, A. Chatelain, and D. Ugarte, "A carbon nanotube field-emission electron source", Science, 270, 1179, 1995.

[131] S. Dimitrijevic, J. C. Withers, V. P. Mammana, O. R. Monteiro, J. W. Ager, and I. G. Brown, "Electron emission from films of carbon nanotubes and ta-C coated nanotubes", Appl. Phys. Lett., 75, 2680, 1999.

[132] J. M. Bonard, N. Weiss, H. Kind, T. Stockli, L. Forro, K. Kern, and A. Chatelain, "Tuning the field emission properties of patterned carbon nanotube films", Advanced Materials, 13, 184, 2001.

[133] M. J. Fransen, Th. L. van Rooy, P. Kruit, "Field emission energy distributions from individual multiwalled carbon nanotubes", Appl. Surf. Sci., 146, 312, 1999.

[134] A. G. Rinzler, J. H. Hafner, P. Nikolaev, L. Lou, S. G. Kim, D. Tomanek, P. Nordlander, D. T. Colbert, and R. E. Smalley, "Unraveling nanotubes: Field emission from an atomic wire", Science, 269, 1550, 1995.

[135] Q. H. Wang, A. A. Setlur, J. M. Lauerhaas, J. Y. Dai, E. W. Seelig, and R. P. H. Chang, "A nanotube-based field-emission flat panel display", Appl. Phys. Lett., 72, 2912, 1998.

[136] W. A. De Heer, J. M. Bonard, T. Stockli, A. Chatelain, L. Forro, and D. Ugarte, "Carbon nanotubes films: Electronic properties and their application as field emitters", Zeitschrift fur Physik D-Atoms Molecules and Clusters, 40, 418, 1997.

[137] J. M. Bonard, F. Maier, T. Stockli, A. Chatelain, W. A. De Heer, J. P. Salvetat, and L. Forro, "Field emission properties of multiwalled carbon nanotubes", Ultramicroscopy, 73, 7, 1998.

[138] P. G. Collins and A. Zettl, "A simple and robust electron beam source from carbon nanotubes", Appl. Phys. Lett., 69, 1969, 1996.

[139] Q. H. Wang, T. D. Corrigan, J. Y. Dai, R. P. H. Chang, and A. R. Krauss, "Field emission from nanotube bundle emitters at low fields", Appl. Phys. Lett., 70, 3308, 1997.

[140] Y. Saito and S. Uemura, "Field emission from carbon nanotubes and its application to electron sources", Carbon, 38, 169, 2000.

[141] E. D. Obraztsova, J. M. Bonard, V. L. Kuznetsov, V. I. Zaikovskii, S. M. Pimenov, A. S. Pozarov, S. V. Terekhov, V. I. Konov, A. N. Obraztsov, and A. P. Volkov, "Structural measurements for single-wall carbon nanotubes by Raman scattering technique", Nanostructured Materials, 12, 567, 1999.

[142] O. M. Kuttel, O. Groning, C. Emmenegger, and L. Schlapbach, "Electron field emission from phase pure nanotube films grown in a methane/hydrogen plasma", Appl. Phys. Lett., 73, 2113, 1998.

[143] S. Fan, M. G. Chapline, N. R. Franklin, T. W. Tombler, A. M. Cassell, and H. Dai, "Self-oriented regular arrays of carbon nanotubes and their field emission properties", Science, 283, 512, 1999.

[144] A. N. Obraztsov, A. P. Volkov, I. Y. Pavlovskii, A. L. Chuvilin, N. A. Rudina, and V. L. Kuznetsov, "Role of the curvature of atomic layers in electron field emission from graphitic nanostructured carbon", JETP Lett. 69, 411, 1999.

[145] D. Xu, G. Guo, L. Gui, Y. Tang, Z. Shi, Z. Jin, Z. Gu, W. Liu, X. Li, and G. Zhang, "Controlling growth and field emission property of aligned carbon nanotubes on porous silicon substrates", Appl. Phys. Lett., 75, 481, 1999.

[146] A. N. Obraztsov, I. Pavlovsky, A. P. Volkov, E. D. Obraztsova, A. L. Chuvilin, and V. L. Kuznetsov, "Aligned carbon nanotube films for cold cathode applications", J. Vac. Sci. Technol. B, 18, 1059, 2000.

[147] H. Murakami, M. Hirakawa, C. Tanaka, and H. Yamakawa, "Field emission from well-aligned, patterned, carbon nanotube emitters", Appl. Phys. Lett., 76, 1776, 2000.

[148] Y. Chen, D. T. Shaw, and L. Guo, "Field emission of different oriented carbon nanotubes", Appl. Phys. Lett., 76, 2469, 2000.

[149] W. Hong, H. Shih, S. Tsai, and C. Shu, "Field-emission properties of aligned carbon nanotubes", Jpn. J. Appl. Phys. 39, L925, 2000.

[150] J. Han, W. Yang, J. Yoo, and C. Park, "Growth and emission characteristics of vertically well-aligned carbon nanotubes grown on glass substrate by hot filament plasma-enhanced chemical vapor deposition", J. Appl. Phys., 88, 7363, 2000.

[151] F. G. Tarntair, L. C. Chen, S. L. Wei, W. K. Hong, K. H. Chen, and H. C. Cheng, "High current density field emission from arrays of carbon nanotubes and diamond-clad Si tips", J. Vac. Sci. Technol. B, 18, 1207, 2000.

[152] A. M. Rao, D. Jacques, R. C. Haddon, W. Zhu, C. Bower, and S. Jin, "In situ-grown carbon nanotube array with excellent field emission characteristics", Appl. Phys. Lett., 76, 3813, 2000.

[153] Y. Chen, S. Patel, Y. Ye, D. T. Shaw, and L. Guo, "Field emission from aligned high-density graphitic nanofibers", App. Phys. Lett., 73, 2119, 1998.

[154] X. Ma, E. Wang, Z. Wuzong, D. A. Jefferson, C. Jun, D. Shaozhi, X. Ningsheng, and Y. Jun, "Polymerized carbon nanobells and their field-emission properties", Appl. Phys. Lett., 75, 3105, 1999.

[155] J. M. Bonard, T. Stockli, F. Maier, W. A. de Heer, and A. Chatelain, "Field-emission-induced luminescence from carbon nanotubes", Phys. Rev. Lett., 81, 1441, 1998.

[156] R. Erz, W. Dotter, K. Jung, and H. Ehrhardt, "Preparation of smooth and nanocrystalline of diamond films", Diamond Relat. Mater., 2, 449, 1993.

[157] Y. Hayashi, W. Drawl, R. W. Collins, and R. Messier, "In-process ellipsometric monitoring of diamond film growth by microwave plasma enhanced chemical vapor deposition", Appl. Phys. Lett., 60, 2868, 1992.

[158] J. S. Ma, H. Kawarada, T. Yonehara, J. I. Suzuki, J. Wei, Y. Yokota, and A. Hiraki, "Selective nucleation and growth of diamond particles by plasma-assisted chemical vapor deposition", Appl. Phys. Lett., 55, 1071, 1989.

[159] M. P. Everson and M. A. Tamor, "Studies of nucleation and growth morphology of boron-doped diamond microcrystals by scanning tunneling microscopy", J. Vac. Sci. Technol. B 9, 1570, 1991.

[160] B. W. Sheldon, R. Csenesits, J. Rankin, and R. E. Boekenhauer, "Bias-enhanced nucleation of diamond during microwave-assisted chemical vapor deposition", J. Appl. Phys., 75, 5001, 1994.

[161] B. R. Stoner, G. H. Ma, S. D. Wolter, and J. T. Glass, "Characterization of bias-enhanced nucleation of diamond on silicon by in vacuo surface ananlysis and transmission electron microscopy", Phys. Rev. B 45, 11067, 1992.

[162] D. Lee and R. K. Singh, "Synthesis of (111) oriented diamond thin films by electrophoretic deposition process", Appl. Phys. Lett., 70, 1542, 1997.

[163] A. Masood, M. Aslam, M. A. Tamor, and T. J. Potter, "Techniques for patterning CVD diamond films on non-diamond substrates", J. Electrochem. Soc., 138, L67, 1991.

[164] K. Hirabayshi, Y. Taniguchi, O. Takamatsu, T. Ikeda, K. Ikoma, and N. Iwasaki-Kurihara, "Selective deposition of diamond crystals by chemical vapor deposition using a tungsten-filament method", Appl. Phys. Lett., 53, 1815, 1988.

[165] M. W. Leksono and H. R. Shanks, "Patterning of microwave plasma deposited diamond films", Mater. Res. Soc. Symp. Proc., 189, 87, 1991.

[166] T. Roppel, R. Ramesham, C. Ellis, and S. Y. Kee, "Thin film diamond microstructures", Thin Solid Films, 212, 56, 1992.

[167] H. Shiomi, "Reactive Ion Etching of Diamond in O_2 and CF_4 Plasma, and Fabrication of Porous Diamond for Field Emitter Cathodes", Jpn. J. Appl. Phys. 1 36, 7745,1997.

[168] N. N. Efremow, M. W. Geis, D. C. Flanders, G. A. Lincoln, and N. P. Economou, "Ion-beam-assisted etching of diamond", J. Vac. Sci. Technol. B 3, 416, 1985.

[169] W. J. Zhang, C. Sun, I. Bello, C. S. Lee, and S. T. Lee, "Bias-assisted etching of polycrystalline diamond films in hydrogen, oxygen, and argon microwave plasmas", J. Vac. Sci. Technol. A 17, 763, 1999.

[170] B. R. Stoner, G. J. Tessmer, and D. L. Dreifus, "Bias assisted etching of diamond in a conventional chemical vapor deposition reactor", Appl. Phys. Lett., 62, 1803, 1993.

[171] S. A. Grot, R. A. Ditizio, G. Sh. Gildenblat, A. R. Badzian, and S. J. Fonash, "Oxygen based electron cyclotron resonance etching of semiconducting homoepitaxial diamond films", Appl. Phys. Lett., 61, 2326, 1992,

[172] M. Karlsson, K. Hjort, and F. Nikolajeff, "Transfer of continuous-relief diffractive structures into diamond by use of inductively coupled plasma dry etching", Optics Letters, 26, 1752, 2001.

[173] L. Ackermann, and W. Kulisch, "Investigation of diamond etching and growth by in situ scanning tunneling microscopy", Diamond Relat. Mater., 8, 1256, 1999.

[174] B. Y. Liaw, T. Stacy, G. Zhao, E. J. Charlson, E. M. Charlson, J. M. Meese, and M. A. Prelas, "Plasma etched polycrystalline hot-filament chemical vapor deposited diamond thin films and their electrical characteristics", Appl. Phys. Lett., 65, 2827, 1994.

[175] M. Rothschild, C. Arnone, and D. J. Ehrlich, "Excimer-laser etching of diamond and hard carbon films by direct writing and optical projection", J. Vac. Sci. Technol. B 4, 310, 1986.

[176] R. Ramesham, W. Welch, W. C. Neely, M. F. Rose, and R. F. Askew, "Plasma etching and patterning of CVD diamond at <100 degrees C for microelectronics applications", Thin Solid Films, 304, 245, 1997.

[177] M. E. Baginski, T. A. Baginski, and J. L. Davidson, "Characterization of the ion-implantation and thermal annealing of boron in (100) diamond", J. Electrochem. Soc., 137, 2984, 1990.

[178] W. Tsai, M. Delfino, D. Hodul, M. Riaziat, L. Y. Ching, G. Reynolds, and C. B. Cooper, "Diamond MESFET using ultrashallow RTP boron doping", IEEE Elect. Dev. Lett., 12, 157, 1991.

[179] J. F. Prins, "Activation of boron-dopant atoms in ion-implanted diamonds"Phys. Rev. B 38, 5576, 1988.

[180] Y. Show, T. Matsukawa, H. Ito, M. Iwase, and T. Izumi, "Structural changes in CVD diamond film by boron and nitrogen doping", Diamond Relat. Mater. 9, 337, 2000.

[181] X. Jiang, P. Willich, M. Paul, and C. -P. Klages, "In situ boron doping of chemical-vapor-deposited diamond films", J. Mater. Res., 14, 3211, 1999.

[182] K. Miyata, K. Kumagai, K. Nishimura, and K. Kobashi, "Morphology of heavily b-doped diamond films", J. Mater. Res., 8, 2845, 1993.

[183] J. Cifre, J. Puigdollers, M. C. Polo, and J. Esteve, "Trimethylboron doping of cvd diamond thin-films", Diamond Relat. Mater. 3, 628, 1994.

[184] A. Masood, M. Aslam, M. A. Tamor, and T. J. Potter, "Synthesis and electrical characterization of boron-doped thin diamond films", Appl. Phys. Lett., 61, 1832, 1992.

[185] D. N. Davydov, J. Li, K. B. Shelimov, T. L. Haslett, M. Moskovits, and B. W. Statt, "Resistance and tunneling spectra of aligned multiwalled carbon nanotube arrays", J. Appl. Phys., 88, 7205, 2000.

[186] Z. F. Ren, Z. P. Huang, J. W. Xu, J. H. Wang, P. Bush, M. P. Siegal, and P. N. Provencio, "Synthesis of large arrays of well-aligned carbon nanotubes on glass", Science, 282, 1105, 1998.

[187] H. M. Cheng, F. Li, X. Sun, S. D. M. Brown, M. A. Pimenta, A. Marucci, G. Dresselhaus, M. S. Dresselhaus, "Bulk morphology and diameter distribution of single-walled carbon nanotubes synthesized by catalytic decomposition of hydrocarbons", Chem. Phys. Lett., 289, 602, 1998.

[188] G. S. Yang, M. Aslam, K. P. Kuo, D. K. Reinhard, and J. Asmussen, "Effect of ultrahigh nucleation density on diamnd growth at different growth rates and temperatures", J. Vac. Sci. Technol. B 13, 1030, 1995.

[189] A. Thess, R. Lee, P. Nikoaev, H. J. Dai, P. Petit, J. Robert, C. H. Xu, Y. H. Lee, S. G. Kim, A. G. Rinzler, D. T. Colbert, G. E. Scuseria, D. Tomanek, J. E. Fischer, and R. E. Smalley, "Crystalline ropes of metallic carbon nanotubes", Science, 273, 483, 1996.

[190] J. Liu, A. G. Rinzler, H. Dai, J. H. Hafner, R. K. Bradley, P. J. Boul, A. Lu, T. Iverson, K. Shelimov, C. B. Huffman, F. Rodriguez-Macias, Y. Shon, T. R. Lee, D. T. Colbert, and R. E. Smalley, "Fullerene pipes", Science 280, 1253, 1998.

[191] L. Forro, J. P. Salvetat, J. M. Bonard, R. Bacsa, N. H. Thomson, S. Garaj, L. Thien-Nga, R. Gaal, A. Kulik, B. Ruzicka, L. Degiorgi, A. Bachtold, C. Schonenberger, S. Pekker, and K. Hernadi, Science and Application of Nanotubes, edited by D. Tomanek and R. J. Enbody, Kluwer Academic/Plenum Publishers, New York, 2000.

[192] Y. Namba, E. Heidrarpour, and M. Nakayama, "Size effects appearing in the Raman spectra of polycrystalline diamond", J. Appl. Phys. 72, 1748, 1992.

[193] R. Saito, T. Takeya, T. Kimura, G. Gresselhaus, and M. S. Dresselhaus, "Finited-size effect on the Raman spectra of carbon nanotubes", Phys. Rev. B 59, 2388, 1999.

[194] J. B. Bindell, "Scanning electron microscopy", Encyclopedia of materials characterization, Butterworth-Heinemann, Boston, 70, 1992.

[195] L. Reimer, "Transmission electron microscopy. Physics of image formation and microanalysis", Springer-Verlag, Berlin, 1984.

[196] R. S. Howland and M. D. Kirk, "Scanning tunneling microscopy and scanning force microscopy", Encyclopedia of materials characterization, Butterworth-Heinemann, Boston, 85, 1992.

[197] D. S. Hong and M. Aslam, "Field-emission from p-type polycrystalline diamond films", J. Vac. Sci. Technol. B 13, 427, 1995.

[198] D. S. Hong, D. M. Aslam, T. Grimm, L. Garbini and S. Bandy, "Field emission from carbon implanted polycrystalline diamond film", Tech. Dig. of IVMC '97, 117, 1997.

[199] Y. Li, D. M. Aslam and S. J. Kwon, "Low voltage emission characteristics of the undoped polycrystalline-diamond field emitter by MPCVD", Tech. Dig. of IVMC '97, 509, 1997.

[200] W. P. Kang, A. Wisitsora-at, J. L. Davidson, D. V. Kerns, Q. Li, J. F. Xu, C. K. Kim, "Effect of sp(2) content and tip treatment an the field emission of micropatterned pyramidal diamond tips", J. Vac. Sci. Technol. B 16, 684, 1998.

[201] J. Angus and A. T. Collins, "Diamond films - electronic era elusive", Nature, 370, 601, 1994.

[202] D. Hong, "Fabrication and characterization of diamond field emitters for field emission displays", Ph. D. Dissertation, Michigan State University, 1997.

[203] H. Dai, J. H. Hafner, A. G. Rinzler, D. T. Colbert, and R. E. Smalley, "Nanotubes as nanoprobes in scanning probe microscopy", Nature, 384, 147, 1996.

[204] S. S. Wong, E. Joselevich, A. T. Wolley, C. L. Cheung, and C. M. Lieber, "Covalently functionalized nanotubes as nanometre-sized probes in chemistry and biology", Nature, 394, 52, 1998.

[205] R. Stevens, C. Nguyen, A. Cassell, L. Delzeit, M. Meyyappan, and J. Han, "Improved fabrication approach for carbon nanotube probe devices", Appl. Phys. Lett., 77, 3453, 2000.

[206] G. Nagy, M. Levy, R. Scarmozzino, R. M. Osgood, Jr., H. Dai, R. E. Smalley, C. A. Michaels, G. W. Flynn, and G. F. McLane, "Carbon nanotube tipped atomic force microscopy for measurement of < 100 nm etch morphology on semiconductors", Appl. Phys. Lett., 73, 529, 1998.

[207] Y. Nakayama, H. Nishijima, S. Akita, K. I. Hohmura, S. H. Yoshimura, and K. Takeyasu, "Microprocess for fabricating carbon-nanotube probes of a scanning probe microscope", J. Vac. Sci. Technol. B 18, 661, 2000.

[208] J. H. Hafner, C. L. Cheung, and C. M. Lieber, "Growth of nanotubes for probe microscopy tips", Nature, 398, 761, 1999.

[209] C. L. Cheung, J. J. Hafner, T. W. Odom, K. Kim, and C. M. Lieber, "Growth and fabrication with single-walled carbon nanotube probe microscopy tips", Appl. Phys. Lett., 76, 3136, 2000.

[210] P. G. Collins and A. Zettl, "Unique characteristics of cold cathode carbon-nanotube-matrix field emitters", Phys. Rev. B 55, 9391, 1997.

[211] Y. Saito, K. Hamaguchi, R. Mizushima, S. Uemura, T. Nagasako, J. Yotani, and T. Shimojo, "Field emission from carbon nanotubes and its application to cathode ray tube lighting elements", Appl. Surf. Sci., 146, 305, 1999.

[212] W. B. Choi, Y. H. Lee, N. S. Lee, J. H. Kang, S. H. Park, H. Y. Kim, D. S. Chung, S. M. Lee, S. Y. Chung, and J. M. Kim, "Carbon-nantubes for full-color field-emission displays", Jpn. J. Appl. Phys., 39, 2560, 2000.

[213] D. Lovall, M. Buss, E. Graugnard, R. P. Andres, and R. Reifenberger, "Electron emission and structural characterization of a rope of single-walled carbon nanotubes", Phys. Rev. B 61, 5683, 2000.

[214] U. Kim, R. Pcionek, D. M. Aslam, and D. Tomanek, "Synthesis of high-density carbon nanotube films by microwave plasma chemical vapor deposition", Diamond Relat. Mater., 10, 1947, 2001.

[215] L. M. Baskin, O. I. Lvov, and G. N. Fursey, Phys. Status Solidi B 47, 49, 1971.

[216] W. A. de Heer, J. -M. Bonard, K. Fauth, A. Chatelain, L. Forro, and D. Ugarte, "Electron field emitters based on carbon nanotube films", Adv. Mater. 9, 87, 1997.

[217] D. T. Carroll, P. Redlich, P. M. Ajayan, J. -C. Charlier, X. Blasé, A. DeVita, and R. Car, "Electronic structure and localized states at carbon nanotube tips", Phys. Rev. Lett., 78, 2811, 1997.

[218] O. Groning, O. M. Kuttel, Ch. Emmenegger, P. Groning, and L. Schlapbach, "Field emission properties of carbon nanotubes", J. Vac. Sci. Technol. B 18, 665, 2000.

[219] A. Modinos, "Field, thermionic, and secondary electron emission spectroscopy", Plenum, New York, 282, 1984.

[220] Y. Muto, T. Sugino, and J. SHirafuji, "Electrical-conduction in undoped diamond films prepared by chemical vapor-deposition", Appl. Phys. Lett., 59, 843, 1991.

[221] A. V. Karabutov, V. D. Frolov, S. M. Pimenov, and V. I. Konov, "Grain boundary field emission from CVD diamond films", Diamond Relat. Mater., 8, 763, 1999.

[222] A. W. S. Williams, E. C. Lightowlers, and A. T. Collins, J. Phys. C 3, 1727, 1970.

[223] M. Fanciulli and T. D. Moustakas, "Defects in diamond thin-films", Phys. Rev. B 48, 14982, 1993.

[224] L. Allers and A. Mainwood, "Surface vacancies in CVD diamond", Diamond Relat. Mater., 7, 261, 1998.

MICHIGAN STATE UNIVERSITY LIBRARIES
3 1293 02372 0455